ABSTRACT

Title of Dissertation: DYNAMICS OF TOPOLOGICAL DEFECTS IN HYBRID QUANTUM SYSTEMS

Hilary M. Hurst, Doctor of Philosophy, 2017

Dissertation Advisor: Professor Victor Galitski

Department of Physics

This dissertation focuses on dynamics and transport effects of semiclassical topological defects in systems with important quantum degrees of freedom, which we term "hybrid quantum systems". The topological defects under consideration are skyrmions and magnetic vortices in layered heterostructures of three-dimensional (3D) topological insulators (TI) and magnetic materials, and dark solitons in Bose-Einstein condensates (BEC).

We examine the proximity effect between a 3D TI and two types of insulating magnets: a chiral magnet with a single skyrmion in a ferromagnetic background, and an XY magnet with strong easy-plane anisotropy which undergoes a vortex unbinding transition. The skyrmion magnetic texture leads to confinement of Dirac states at the skyrmion radius, resulting in a charged skyrmion that can be manipulated by an external electric field. We show that the bound states are robust in the presence of an external magnetic field. Magnetic vortices in the XY magnet affect electronic transport at the TI surface. Scattering at classical magnetic fluctuations influences surface resistivity of the TI, and near the transition

temperature we find that the resistivity has a clear maximum and scales linearly with temperature on either side of the transition. We discuss the limits of mapping the TI-XY magnet model to the classic theoretical problem of free Dirac fermions in a random magnetic field.

Secondly, we study dark solitons in a BEC coupled to thermal non-interacting impurity atoms acting as a dissipative bath. We calculate the friction coefficient due to scattering and find that it can be tuned with accessible experimental probes. We develop a general theory of stochastic dynamics of the negative-mass dark soliton and solve the corresponding Fokker-Planck equation exactly. From the time-dependent phase-space probability distribution function we find the soliton can undergo Brownian motion only in the presence of friction and a confining potential.

Finally, we numerically study the ground-state properties of a spin-1 BEC gas in the "synthetic dimensions" experimental set-up. Ground state phases depend on the sign of the spin-dependent interaction parameter and the strength of the spin-orbit field. We find "charge"- and spin-density-wave phases related to helical spin order.

Dynamics of Topological Defects in Hybrid Quantum Systems

by

Hilary M. Hurst

Dissertation submitted to the Faculty of the Graduate School of the
University of Maryland, College Park in partial fulfillment
of the requirements for the degree of
Doctor of Philosophy
2017

Advisory Committee:
Professor Victor Galitski, Chair
Professor Maissam Barkeshli
Professor Ian Spielman
Professor John Weeks
Professor Victor Yakovenko

to my family

Acknowledgments

It goes without saying that no one gets through a Ph.D. program alone. I have many people to thank for both scientific and moral support along this journey, and I am grateful to all of them for making my graduate school experience a good one.

First and foremost, thanks to my advisor Victor Galitski. He provided no shortage of interesting physics problems to study and helped me gain the technical skills I needed to be successful. He also facilitated collaborations and travel opportunities to meet physicists from all over the world beyond any expectations I had for my graduate school experience. I will always be grateful for his guidance and willingness to promote his students' work in the physics community.

I am fortunate to have had many great collaborations while in graduate school. Firstly, thanks to Dmitry Efimkin, who appears on 4 of the 5 publications in this thesis and has been a wonderful mentor and collaborator. Particularly, Dmitry was the first person that I worked closely with as a graduate student and I am grateful for his patience and guidance in finding the best resources for learning new techniques. Thanks as well to Ian Spielman, who floated the idea of collaboration on some ongoing experimental work which grew into a number of successful projects and (almost) converted me into a cold atoms theorist. Justin Wilson, Jed Pixley, and Stefan Natu helped me learn numerics and were great fun to work with. I am grateful my experimental colleagues, Lauren Aycock and Dina Genkina in particular have become friends and collaborators and continue to teach me about the realities of life in the lab. Thank you to Charlie Tahan and Rusko Ruskov at the Laboratory for Physical Sciences (LPS) for their support when I was there as an intern, and in particular to Charlie for telling me about the NPSC graduate fellowship.

Thank you to my many office and group-mates over the years, Juraj Radić, Aydin Keser, Andrew Allocca, Zach Raines, Sergey Peroshguba, Medhi Kargarian, Valentin Stanev, Efim Rozenbaum, Jon Curtis, and Yi-Hua Lai. Thank you to the Women in Physics and Graduate Committee groups, who have provided a space for conversation and emotional support - in particular Gina Quan, Steve Ragole, Caroline Figgatt, Megan Marshall, Amit Nag, and Zach Eldredge have contributed to a more positive graduate school experience for me and many others.

Thank you to those who have known me since before I started graduate school and supported me through it, including professors Mark Lusk and Lincoln Carr at Colorado School of Mines, without whom I may not have gone to graduate school at all. Thanks to my parents Paul and Patty and my sister Heidi for their unwavering support, and to my best friends since childhood Julia Derk and Christi Baker for support from afar. Finally, thanks most of all to Duncan, who has supported me through everything from qualifying exams to this dissertation and beyond. I can never thank you enough.

Table of Contents

List of Tables

List of Figures

Abbreviations

BEC	**B**ose-**E**instein **C**ondensate
BKT	**B**erezinskii-**K**osterlitz-**T**houless
BZ	**B**rillouin **Z**one
CDW	**C**harge **D**ensity **W**ave
DM	**D**zyaloshinskii-**M**oriya
GPE	**G**ross-**P**itaevskii **E**quation
LL	**L**andau **L**evel(s)
MF	**M**ean **F**ield
PDF	**P**robability **D**istribution **F**unction
QHE	**Q**uantum **H**all **E**ffect
RMF	**R**andom **M**agnetic **F**ield
SDW	**S**pin **D**ensity **W**ave
SF	**S**uper**f**luid
SS	**S**urface **S**tate
SOC	**S**pin **O**rbit **C**oupling
TI	**T**opological **I**nsulator
TRIM	**T**ime **R**eversal **I**nvariant **M**omentum

Physical Constants

Speed of Light	c	$2.997\ 924\ 58 \times 10^{8}$ m/s
Elementary Charge	e	$1.602\ 176\ 621 \times 10^{-19}$ C
Planck constant	$\hbar$	$6.582\ 119\ 514 \times 10^{-16}$ eV-s/rad
Boltzmann constant	k_{B}	$8.617\ 3303 \times 10^{-5}$ eV/K
Bohr magneton	μ_b	$5.788\ 381\ 801 \times 10^{-5}$ eV/T

List of Publications

This dissertation is based on the following publications

1. Hurst, H. M., Efimkin, D. K., Zang, J., & Galitski, V. "Charged skyrmions on the surface of a topological insulator." *Physical Review B*, **91**(6), 060401(R), (2015).

2. Hurst, H. M., Efimkin, D. K., & Galitski, V. "Transport of Dirac electrons in a random magnetic field in topological heterostructures." *Physical Review B*, **93**(24), 245111, (2016).

3. Hurst, H. M., Wilson, J. H., Pixley, J. H., Spielman, I. B., & Natu, S. S. "Real-space mean-field theory of a spin-1 Bose gas in synthetic dimensions." *Physical Review A*, **94**(6), 063613, (2016).

4. Aycock, L. M., Hurst, H. M., Efimkin, D. K., Genkina, D., Lu, H.-I., Galitski, V., & Spielman, I. B. "Brownian motion of solitons in a Bose Einstein condensate." *Proceedings of the National Academy of Sciences*, **114**(10), 2503-2508, (2017).

5. Hurst, H. M., Efimkin, D. K., Spielman, I. B., & Galitski, V. "Kinetic theory of dark solitons with tunable friction." *Physical Review A*, **95**(5), 053604, (2017).

Chapter 1: Introduction

Once reserved for a branch of mathematics, it is now widely accepted that topology plays a role in many important physical phenomena, as recognized by the Nobel Prize in Physics in 2016 for "for theoretical discoveries of topological phase transitions and topological phases of matter" [1]. Topology in physics often manifests as a conserved global property of a system or object classified by a discrete index known as a *topological invariant*. This dissertation examines physical consequences of two different types of topology: topological defects and topological phases of matter. Both are special because they are robust in the presence of local perturbations, the system must be acted upon globally to change them. This introductory Chapter contains an introduction to these two ideas, background information on the theory of topological defects in nonuniform media, an introduction to the physical systems studied, and an overview of the original results presented in the thesis.

Topological defects occur in both classical and quantum systems described by nonlinear field equations. They are nonperturbative, exact solutions of the underlying field equations and are classified by a *winding number* topological invariant. Topological defects have a finite (often macrsocopic) size and are embedded in otherwise conventional classical or quantum systems described by an order parameter. The nontrivial homotopy groups of the order parameter space determine what types of topological defects are possible for a given system [2, 3]. A brief introduction to the topological theory of defects, including homotopy classification, is given in Section 1.1. Topological defects are physically stable in part due to their topological classification. They are not usually the ground state of the

system, rather they are metastable saddle-point solutions of the free energy that can have very long lifetimes. The defects studied here are skyrmions and vortices in magnetic systems, and dark solitons in Bose-Einstein Condensates (BECs).

Topological phases of matter are a different manifestation of topology in which the bulk of the material itself can be described by a topological invariant. The difference in topology between the bulk of the material and the vacuum (or a "topologically trivial" material) results in robust conducting states at the interface between the two, with specific transport properties [4, 5]. The two-dimensional electron gas in the quantum hall regime was the first example of such a state, where the one-dimensional edge states give nonzero longitudinal conductivity at exact multiples of the quantum of conductance [4, 6]. The topological invariant for the quantum hall effect (QHE) is called a Chern number. More recently, three-dimensional topological insulators (TIs) have been discovered, which have two-dimensional surface states (SS) protected from disorder as long as the disorder preserves time-reversal symmetry (TRS). These TIs are characterized by four $\mathbb{Z}_2$ topological invariants [5]. The discovery and classification of new types of topological materials is an active area of research, but is not the focus of this work. Here, we study two types of topological phases of matter in different systems: 3D TIs coupled to magnetic topological defects, and an ultracold atom realization of the Quantum Hall Effect (QHE) using spin-1 bosons with spin-orbit coupling.

This thesis is focused on the dynamics of topological defects in systems where quantum and classical degrees of freedom are important. We are interested in dynamics of topological defects and how they can affect the properties of a solid-state or cold atom system. Additionally, we are interested in modeling topological phases of matter using spinor BECs. This dissertation presents an original research contribution at the interface of classical and quantum physics. We present research

that has increased understanding of the dynamics of topological defects embedded in quantum systems, and how they affect the quantum degrees of freedom in the system. We show that topological defects have consequences for transport phenomena in solid-state systems and can have unconventional dynamics themselves. We treat topological defects semi-classically and assume that they are not destroyed by quantum fluctuations. This assumption is well justified based on the topological protection of such defects and is aligned with previous theoretical and experimental results.

1.1 Defects in Ordered Media

The classification and characterization of new phases of matter lies at the heart of condensed matter physics. Ordered phases are particularly interesting because they can lead to macroscopic phenomena like ferromagnetism and superfluidity. Phases of matter are characterized by an *order parameter*. That is, at each point in space $\mathbf{r}$ there is a function $f(\mathbf{r})$ describing the system at that point. The mapping $f(\mathbf{r}) : \mathbb{R}^d \to \mathcal{M}$ is a mapping between real space of dimension d (typically $d = 2$ or 3) and order parameter space, $\mathcal{M}$. $\mathcal{M}$ constitutes a manifold of internal states that the system can have. For example, in a magnetic system $f(\mathbf{r})$ is the value of the magnetization at $\mathbf{r}$.

Consider "free" spins with fixed magnitude that can point in any direction. Their manifold of internal states is the surface of a sphere S^2, characterized by polar angles Θ, Φ. In this case, $f(\mathbf{r}) = (\cos\Phi(\mathbf{r})\sin\Theta(\mathbf{r}), \sin\Phi(\mathbf{r})\sin\Theta(\mathbf{r}), \cos\Theta(\mathbf{r}))$. Figure 1.1 shows a real space representation of a line of free spins and the equivalent picture in the order parameter space S^2.

An ordered phase of matter is uniform if $f(\mathbf{r})$ is constant for all $\mathbf{r}$. Because of this property, it is possible to classify uniform phases by calculating the order

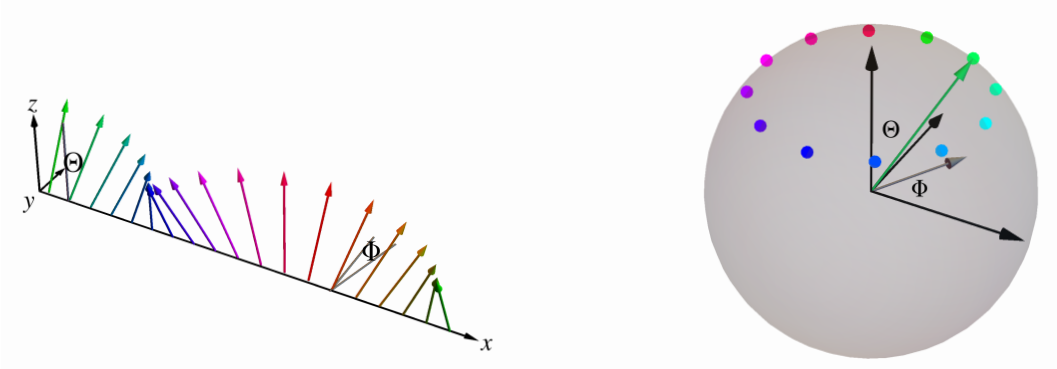

FIGURE 1.1: Mapping a line of helical ordinary spins to order parameter space. (Left) A one-dimensional line of canted spins. (Right) The representation of those spins in the order parameter space S^2. The spins are parameterized by angles Φ and Θ. The dots on the sphere are the same color as the corresponding spins in the real space line.

parameter at a single local point in space. However, for nonuniform media the order parameter may vary smoothly in space and might have singular points or lines. Identification and classification of singular points or lines is central to the theory of topological defects. Singularities in the order parameter are identified by first drawing a closed contour in real space and calculating the order parameter at every point along the contour, thereby giving another contour in $\mathcal{M}$. The real-space contour encloses a topological defect only if the corresponding contour in $\mathcal{M}$ cannot be continuously deformed to a single point; a single point in order parameter space indicates a uniform phase.

Configurations in order parameter space that can be continuously deformed into one another are *topologically equivalent* and describe a single class of defects. Later in the chapter we will formalize this idea using homotopy theory. Topologically equivalent field configurations are homomorphic, and the transformation that continuously deforms one configuration into another is called a homomorphism. By definition, topological defects are *not* homomorphic to a uniform phase. In

other words, the defect cannot be removed by making local changes to the system. In fact, the defect can be identified by looking at any closed contour surrounding it, even arbitrarily far from the defect site. This global property is what distinguishes topological defects from other types of imperfections in media such as vacancies or surface roughness. In the following subsections we discuss how to assign a group structure to order parameter space and give a short introduction to homotopy theory as it relates to defects in condensed matter. This mathematical foundation allows us, in the remainder of this thesis, to study perturbations around topological defects due to quantum scattering effects.

A few caveats are required for this discussion. Strictly speaking, the topological classification applies only to continuum theories, where translational symmetry is preserved [2]. The models we discuss are appropriately described by a continuum theory, meaning that the order parameter varies on a longer length scale than than the separation between atoms. A small length scale cutoff, typically the lattice constant of the material, is required for the continuum theory to accurately represent the system. Secondly, it is important to note that while homotopy theory defines which defects can exist, energetics must always be considered when trying to describe a real system. A state with topological defects has a higher energy than a uniform state because gradient terms in the free energy are nonzero. However, these phases constitute long-lived metastable states because the energy barrier between the uniform state and the state with a topological defect is very high. Field configurations with topological defects are therefore saddle point solutions of the free energy of the system. One the other hand, many topological defects can exist in principle but the energy needed to create them is too high for them to be found in systems like the ones discussed in this thesis.

1.1.1 Group Structure of Order Parameter Space

In all of the systems considered here, the order parameter space $\mathcal{M}$ is best described using the tools of group theory. In general the order parameter $f(\mathbf{r})$ can take many values. Suppose that two different values of the order parameter $f_1 \to f_2$ are related by a transformation g, such as a rotation or translation, where $f_2 = gf_1$. The set of all such transformations constitutes a group $G = \{g\}$ [2]. Likewise, there is a set of transformations $h \in G$ that leave the value of the order parameter unchanged, $f_1 = hf_1$. The group $H = \{h\}$ is called the isotropy subgroup or "little group" of G. The order parameter space $\mathcal{M}$ is the set of all possible transformations on the system modulo transformations that leave the system unchanged, since they are redundant descriptions of the system. In other words, $\mathcal{M}$ is the space of cosets of H in G, denoted

$$\mathcal{M} = G/H. \tag{1.1}$$

It can be shown that the correspondence between $\mathcal{M}$ and G/H is one-to-one and continuous [2]. It is tempting to say that $\mathcal{M}$ is itself a group but this is not always true. If H is a normal subgroup of G, then the left coset gH and right coset Hg contain the same elements for all $g \in G$. In this case, $\mathcal{M}$ is a group, called the quotient group. However, if H is not a normal subrgroup then $\mathcal{M}$ is not a group and should be described only as a space of cosets [2, 7].

The group theory classification of order parameter space is related to the familiar concept of symmetry breaking. The group G is the symmetry group of the disordered phase. When the system is ordered, the symmetry of G is broken, but usually some degree of symmetry remains. H is nothing but the remaining symmetry group of the ordered phase relative to some reference order parameter

f. Free spins provide an intuitive example, shown in Figure 1.1. The spins are free to point in any direction, giving $G = SO(3)$. We choose the $+z$ axis as the reference order parameter for the ordered phase, where all spins are aligned along the $+z$ axis. Rotations about the $+z$ axis will leave the spin unchanged, which gives $H = SO(2)$. Thus, the order parameter space is $\mathcal{M} = SO(3)/SO(2) \simeq S^2$.

There are often multiple descriptions of $\mathcal{M}$ based on group isomorphisms, and in the literature one finds that they are used interchangeably depending on what is most convenient for the system at hand. In this example, $SO(3)$ is isomorphic to $SU(2)$, which has the isotropy subgroup $U(1)$. Therefore, we can equally describe $\mathcal{M}$ for ordinary spins as $\mathcal{M} = SU(2)/U(1) \simeq S^2$.

1.1.2 Homotopy Theory in a Nutshell

Consider a system of two-dimensional spins confined to rotate in the plane. Such a system may host a vortex as shown in Figure 1.2. We can characterize the vortex by its winding number, which counts how many times the spin vector wraps around the unit circle as we travel counterclockwise along a real-space closed contour (shown in blue in Figure 1.2); both vortices in Figure 1.2 have winding number $N = 1$. The winding number is defined as positive if the vector rotates counterclockwise and negative if it rotates clockwise. By assigning a winding number we have learned a lot about that particular vortex. However, we still don't know much about what other types of vortices can occur, or what happens when you combine them. Vortices with the same winding number can look different, yet they are topologically equivalent. Homotopy theory provides this information via a more complete classification of topological defects. Classification of a topological defect is determined by mapping the contour in real space to a contour in order parameter space. Families of contours *in order parameter space* that can be continuously

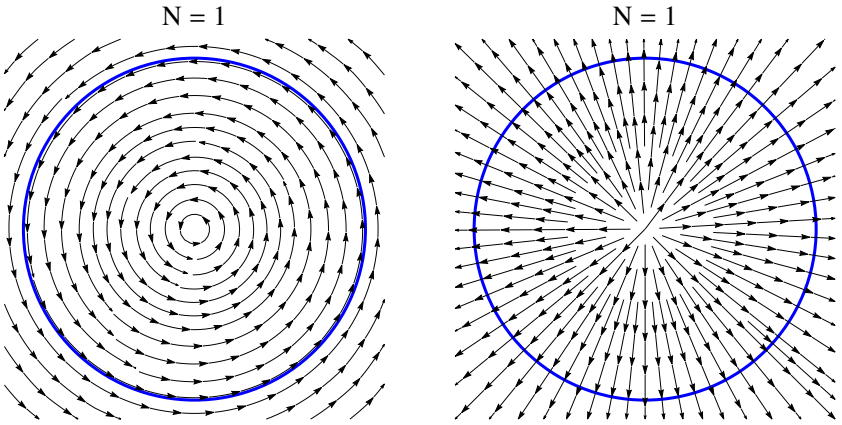

FIGURE 1.2: Vortices with winding number $N = 1$. The blue (thick) line indicates a possible choice of real-space contour along which to calculate the order parameter.

deformed into one another constitute a *homotopy class*, and correspond to a single class of topological defects [2].

The group elements of a homotopy group are classes of closed homotopic loops, each describing different topological defects. Homotopy groups are denoted $\pi_i(\mathcal{M})$ and map spheres of dimension i onto the manifold $\mathcal{M}$. Topological defects occur in systems with nontrivial homotopy groups. There are two important steps to understand whether topological defects occur in a particular system: identify the order parameter space $\mathcal{M}$ and compute the homotopy groups for $\mathcal{M}$. Homotopy groups with $i \leq 3$ are typically the only relevant ones for physical applications.

Here we state the most important results of homotopy theory as applied to condensed matter systems. The fundamental group $\pi_1(S^m)$ describes 1D line defects in a space of dimension $m \geq 2$. In one dimension, $\pi_1(S^1)$ describes point defects. $\pi_2(S^m)$ describes point defects in dimensions $m \geq 2$, and $\pi_3(S^m)$ describes nonsingular field configurations [2, 8]. Note that the dimension of $\mathcal{M}$ is often not the same as the real-space dimension of the system being studied. The homotopy classification always comes from the classification of closed contours in

order parameter space. Homotopy groups where $\pi_i(\mathcal{M}) = 0$ are trivial; every configuration can be continuously deformed to the topologically trivial one. A useful rule of homotopy groups is [3]:

$$\pi_n(S^n) = \mathbb{Z} \tag{1.2}$$

$$\pi_n(S^m) = 0 \;\; ; \;\; n < m \tag{1.3}$$

$$\pi_n(S^1) = 0 \;\; ; \;\; n > 1 \tag{1.4}$$

Higher-order homotopy groups are notoriously difficult to calculate [2]. Perhaps the most famous higher-order homotopy mapping is $\pi_3(S^2) = \mathbb{Z}$ discovered in 1931 by Heinz Hopf, which is called the Hopf fibration. The Hopf fibration maps $S^3 \to S^2$ resulting in a diversity of "knot solitons" classified according to integer winding numbers [9]. The Hopf fibration has been observed recently in chiral nematic liquid crystals [10]. In general, once the order parameter space $\mathcal{M}$ is known it is simple enough to look up the homotopy groups of $\mathcal{M} = G/H$. There are also two theorems which are useful for calculating $\pi_1(\mathcal{M})$ and $\pi_2(\mathcal{M})$ [2]:

Theorem 1.1. *Let G be a simply connected group with an isotropy subgroup H. Then $\pi_1(G/H)$ is isomorphic to the quotient group H/H_0, where H_0 is the set of points in H connected to the identity by continuous paths.*

Theorem 1.2. *Let G be a simply connected, continuous group with an isotropy subgroup H. Then $\pi_2(G/H)$ is isomorphic to $\pi_1(H_0)$.*

Both theorems require that G be simply connected, which can be achieved by making G the universal covering group of the system of interest. Theorem 1.2 is true provided that $\pi_2(G) = 0$, which is true for any simply connected continuous group according to Cartan's 1936 theorem [11]. In the following section we apply these concepts in detail to a system of spins of fixed magnitude confined to rotate

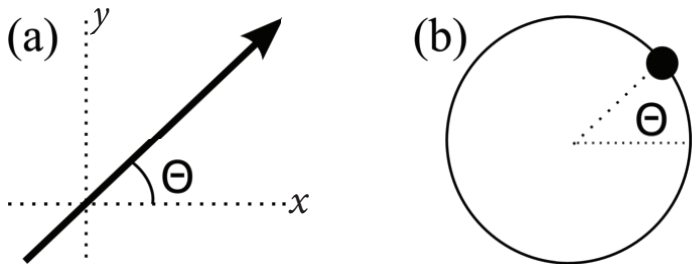

FIGURE 1.3: (a) Real-space representation of a single spin in the $x-y$ plane rotated from the x-axis by an angle Θ. (b) Order-parameter space representation of the same spin on the unit circle. The manifold of internal states is $\mathcal{M} = T_{\varphi}/T_{2\pi n} \simeq S^1$.

in a 2D plane as shown in Figure 1.3. This provides an intuitive example that has a nontrivial homotopy classification and is relevant to two physical systems in this thesis: the magnetic XY-model in Chapter 3 and quasi-1D BECs in Chapter 4.

Case Study: Spins in the x-y plane

Here we apply the concepts of order parameter space and homotopy classification in detail to the example of planar spins in two dimensions. This type of model is used to describe two-dimensional thin film magnets with strong in-plane anisotropy and quasi-2D BECs. The spins have fixed magnitude but are free to rotate in the plane, giving them one degree of freedom which is the angle Θ between the planar spin and the x-axis, as shown in Figure 1.3. The order parameter is

$$f(\Theta(\mathbf{r})) = \cos\Theta(\mathbf{r})\hat{\mathbf{x}} + \sin\Theta(\mathbf{r})\hat{\mathbf{y}}. \tag{1.5}$$

By this construction we see that the one-dimensional order parameter space is the unit circle. An alternative complex parameterization is $f(\Theta(\mathbf{r})) = e^{i\Theta(\mathbf{r})}$ which evokes a phase Θ for the spins. The natural choice for the symmetry group G is

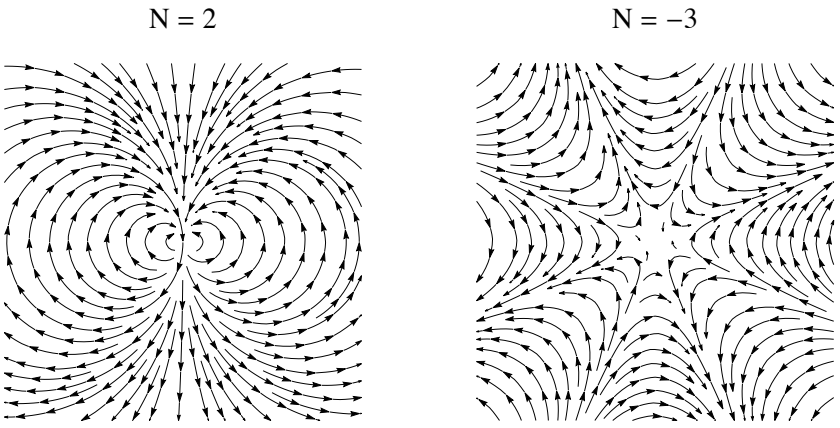

FIGURE 1.4: 2D planar spins in vortex configurations with higher order winding numbers.

the group of rotations in the $x-y$ plane, $G = SO(2)$. However, since $SO(2)$ is not simply connected we cannot apply the theorems of the previous section. Instead, the appropriate choice of G is the one-dimensional translation group $T(1)$ with elements $T_\Phi(\Theta) = \Theta - \Phi$. From the order parameter in Eq. (1.5), it is clear that translations by multiples of 2π leave f invariant. The isotropy group H is therefore a discrete group of elements of T where $\Phi = 2\pi n$ for n positive or negative integer.

$$H = T_{2\pi n} = \{\ldots - 2\pi, 0, 2\pi, 4\pi, \ldots\} \tag{1.6}$$

Having identified G and H, we can now calculate $\pi_1(G/H) \simeq H/H_0$. Since H is a discrete group, the only element connected to the identity is the identity itself, translation by $\Phi = 0$. Therefore $H/H_0 = H$ itself, which is isomorphic to the set of integers $\mathbb{Z}$. Finally, we arrive at the result

$$\pi_1(T_\Phi/T_{2\pi n}) \simeq \mathbb{Z}, \tag{1.7}$$

giving the integer winding number classification. Examples of vortices with higher winding numbers are shown in Figure 1.4. This example shows the flexibility

of homotopy theory for classification of topological defects provided that we are careful in selecting the correct group description of order parameter space.

1.2 Physical Systems: Solid-State Heterostructures

In this Section we introduce the system relevant to Chapter 2 and Chapter 3. We will be studying the properties of the 2D interface between a 3D topological insulator and two different types of magnetic materials.

1.2.1 Skyrmions in Chiral Magnets

A magnetic skyrmion is a topological spin texture with whirlpool-like structure, illustrated in Figure 1.5. The skyrmion consists of many individual $O(3)$ spins spatially confined to the 2D plane with a spin texture equivalent to a 3D point defect. The 3D point defect or hedgehog texture is revealed by stereographic projection of the spins from $\mathbb{R}^2 \to S^2$ [12]. Thus, their homotopy classification is $\pi_2(S^2) = \mathbb{Z}$ and the skyrmion topology is characterized by a winding number topological invariant that takes integer values,

$$N_{\mathrm{S}} = \int \frac{d\mathbf{r}}{4\pi} \hat{\mathbf{n}} \left[\frac{\partial \hat{\mathbf{n}}}{\partial x} \times \frac{\partial \hat{\mathbf{n}}}{\partial y} \right], \tag{1.8}$$

where $\hat{\mathbf{n}}(\mathbf{r})$ is the unit vector describing direction of the magnetization and $N_{\mathrm{S}} \in \mathbb{Z}$. A single skyrmion texture is parameterized by the spin vector

$$\hat{\mathbf{n}}(\mathbf{r}) = \begin{pmatrix} \sin\Theta(\mathbf{r}) \cos\Phi(\mathbf{r}) \\ \sin\Theta(\mathbf{r}) \sin\Phi(\mathbf{r}) \\ \cos\Theta(\mathbf{r}) \end{pmatrix} \tag{1.9}$$

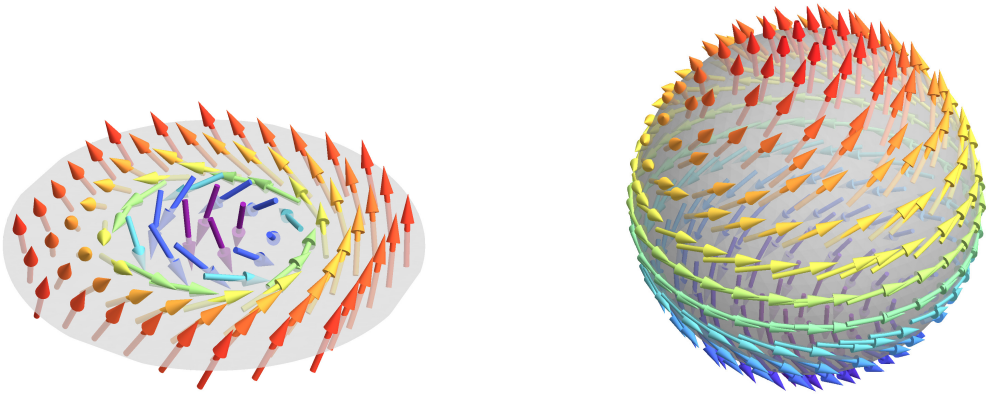

FIGURE 1.5: Skyrmion spin texture. (Left) Skyrmion spin texture with winding number $N_S = 1$, as it appears in real materials defined on $\mathbb{R}^2$. (Right) The same spin texture after stereographic projection to S^2. The spins form a hedgehog texture that fully covers S^2 leading to the homotopy classification $\pi_2(S^2) = \mathbb{Z}$.

where $\mathbf{r} = (\rho\cos\varphi, \rho\sin\varphi)$. Magnetic skyrmions, which can be 100s of nanometers in size, have been experimentally observed in various chiral magnets as a result of the competition between the Dzyaloshinskii-Moriya (DM) interactions, Heisenberg exchange, and Zeeman interaction [13–17]. The free energy of a two-dimensional chiral magnet is given by

$$F[\hat{\mathbf{n}}] = \int d\mathbf{r}\ \frac{J}{2}(\nabla\hat{\mathbf{n}})^2 + D\hat{\mathbf{n}}\cdot(\nabla\times\hat{\mathbf{n}}) - \mathbf{B}\cdot\hat{\mathbf{n}}, \tag{1.10}$$

where J is the Heisenberg exchange energy, D is the strength of the DM interaction and $\mathbf{B}$ is an external magnetic field. Without the magnetic field, the ground state of this system with $D > 0$ is a spiral state with period $\sim D/J$ and right-handed chirality [16–18]. The sign of D also determines the chirality of the skyrmion. Here, we briefly show how to construct a vortex or skyrmion texture with winding number $N_S = 1$ from the free energy in Eq. (1.10).

We assume a rotationally symmetric solution and use following ansatz for the

magnetization $\hat{\mathbf{n}}(\mathbf{r})$,

$$\Theta(\mathbf{r}) = \Theta(\rho) \;\; ; \;\; \Phi(\mathbf{r}) = \varphi + \pi/2,$$

where the factor of $\pi/2$ determines the chirality of the in-plane magnetization. Under this ansatz, the free energy is

$$\mathcal{F}[\Theta] = 2\pi \left(\frac{J}{2}\right) \int d\rho\rho \left[\left(\frac{\partial\Theta}{\partial\rho}\right)^2 + \frac{\sin^2\Theta}{\rho^2} + 2d\frac{\partial\Theta}{\partial\rho} + 2d\frac{\sin\Theta\cos\Theta}{\rho} - 2b^2\cos\Theta \right], \tag{1.11}$$

where $d = D/J$ and $b = \sqrt{B/J}$. The Euler-Lagrange equation for $\Theta(\rho)$ is

$$\frac{\partial^2\Theta}{\partial\rho^2} + \frac{1}{\rho}\frac{\partial\Theta}{\partial\rho} - \frac{2\sin\Theta\cos\Theta}{\rho^2} + \frac{2d\sin^2\Theta}{\rho} - b^2\sin\Theta = 0, \tag{1.12}$$

with boundary connditions $\Theta(0) = \pi$ and $\Theta(\rho \to \infty) = 0$, so the spin is pointed along $-\hat{z}$ at the skyrmion core and $+\hat{z}$ outside the skyrmion. The skyrmion radius ρ_S is defined where out-of-plane magnetization vanishes, $\Theta(\rho_S) = \pi/2$. The asymptotic behavior of $\Theta(\rho)$ is [16]

$$\Theta(\rho) \propto \begin{cases} \pi - \rho & \rho \to 0 \\ e^{-b\rho} & \rho \to \infty \end{cases} \tag{1.13}$$

In general Eq. (1.12) must be solved numerically for different material parameters to determine the size and stability of skyrmions, which can occur alone or in triangular lattices [16, 19]. The skyrmion crystal was first discovered in MnSi in a narrow window at finite temperatures [13]. However, once on a thin film, the skyrmion phase can be greatly extended even down to zero temperature, as long as the external magnetic field is properly tuned [14]. Although it has been demonstrated that metallic skyrmions can be driven by the spin transfer torque (STT) from an electric current [20, 21], recent appearance of the insulating helimagnet

material Cu_2OSeO_3 raises a more challenging question of how to manipulate insulating skyrmions [22–25]. It is important not only from a fundamental point of view, but also for applications in spintronics and memory devices (see Ref. [26] for a recent review).

1.2.2 Vortices in XY-Magnets

The XY model in 2D describes magnetic moments $\hat{\mathbf{n}}(\mathbf{r}) = (\cos\Theta(\mathbf{r}), \sin\Theta(\mathbf{r}))$ with fixed magnitude and arbitrary angle in the x-y plane. This is exactly the model considered in detail in Section 1.1.2. In this section we briefly discuss how the vortices affect spin correlations. Low energy modes are described by the dimensionless continuum model

$$S_{\mathrm{XY}} = \frac{\rho_{\mathrm{S}}}{2T} \int d\mathbf{r} (\nabla\Theta(\mathbf{r}))^2 \tag{1.14}$$

with temperature T spin-wave stiffness ρ_{S}. The Mermin-Wagner theorem forbids long-range ordering in 2D at all nonzero temperatures, so this system never exhibits true long-range order [27, 28]. However, the action in Eq. (1.14) does admit vortex solutions, which lead to quasi-long range order at low temperatures and unusual behavior in the spin-spin correlation function. The spin-spin correlation function is

$$\langle n_\alpha(\mathbf{r}_1) n_\beta(\mathbf{r}_2)\rangle = \frac{1}{2}\left(\frac{\mathbf{r}}{2a}\right)^{-\eta} e^{-\mathbf{r}/\xi_+(T)}\delta_{\alpha\beta} \quad ; \quad \mathbf{r} = |\mathbf{r}_1 - \mathbf{r}_2|\,, \tag{1.15}$$

where where a is a cutoff for the magnet of the order of the vortex core size, which is approximately the lattice constant of the magnet. The critical exponent

$\eta(T) = T/2\pi\rho_s$ takes values from $\eta(0) = 0$ to $\eta_{\rm BKT}(T_{\rm BKT}) = 1/4$. The calculation of the classical correlation function for $T < T_{\rm BKT}$ is shown in Appendix B. The behavior of correlation functions at different temperatures is related to the behavior of vortices in the material. Eq. (1.15) decays algebraically at low temperatures $\propto \mathbf{r}^{-\eta}$ where vortex-antivortex pairs are tightly bound. Above the transition temperature, vortex pairs unbind, and spin correlations decay exponentially $\propto \exp(-\mathbf{r}/\xi_+)$ for $T > T_{\rm BKT}$. Near the transition temperature $T_{\rm BKT}$ the correlation length $\xi_+(T)$ is given by

$$\xi_+(T) \approx a \exp\left(\frac{3T_{\rm BKT}}{2\sqrt{T - T_{\rm BKT}}}\right). \tag{1.16}$$

$\xi_+(T)$ is finite only above the BKT transition and diverges exponentially as $T \to T^+_{\rm BKT}$ [29–31]. The transition between these two regimes, referred to as the BKT transition, is driven by the unbinding of magnetic vortex-antivortex pairs and occurs at $T_{\rm BKT} = \pi\rho_S/2$. The full nature of the vortex-unbinding transition is revealed through RG analysis, however a simple energetic analysis provides some intuition for why it occurs, which we summarize below [30].

The vortices are non-local field configurations with winding number n such that the field configuration obeys $\oint \nabla\Theta \cdot d\mathbf{l} = 2\pi n$ on a contour enclosing the defect. This implies that $\nabla\Theta = n/r(\hat{e}_z \times \hat{e}_r)$. Referring to the action in Eq. (1.14), the energy required to create a vortex is

$$E_{\rm v} = \frac{\pi\rho_S n^2}{T} \ln\left(\frac{L}{a}\right) + E_{\rm core}, \tag{1.17}$$

where L is the size of the system. The contribution from the vortex core $E_{\rm core}$ is a constant which is unimportant in the thermodynamic limit as system size L increases. Therefore, there is an energy cost associated with creating a vortex.

However, entropy also increases with vortex creation as

$$S_{\mathrm{v}} = 2\ln\left(\frac{L}{a}\right) \tag{1.18}$$

resulting from the number of vortex configurations possible for an area of size L^2. The free energy $\tilde{F} = F/T = E_{\mathrm{v}} - S_{\mathrm{v}}$ for $n = 1$ is then

$$\tilde{F} = \left(\frac{\pi\rho_{\mathrm{S}}}{T} - 2\right)\ln\left(\frac{L}{a}\right). \tag{1.19}$$

Clearly, as temperature increases the proliferation of vortices becomes energetically favorable due to the increase in entropy associated with them, and the critical temperature is $T_{\mathrm{BKT}} = \pi\rho_{\mathrm{s}}/2$. The total vorticity of a neutral sample is zero, and the conclusion is that vortices are bound in vortex-antivortex pairs below T_{BKT} and become unbound across the transition [30]. The XY-model can occur in magnetic thin films with strong in-plane anisotropy, and has been realized in several compounds including K_2CuF_4, Rb_2CrCl_4, $BaNi_2(VO_4)_2$ and $(CH_3NH_3)_2CuCl_4$ [32–38]. Additionally, quasi-2D BECs are described by the same physics and the BKT transition has also been observed in trapped atomic gases [39].

1.2.3 3D Topological Insulators

Topological insulators (TIs) are a class of matter with nontrivial topology characterized by properties of the bulk material. The bulk of a topological insulator has an insulating bandgap, as for typical (trivial) insulators. However, the topology of the bulk material is not equivalent a trivial insulator because they belong to different homotopy classes. As with topological defects, TIs are classified according to a topological invariant. Instead of mapping from real space to order parameter space as discussed in the preceding sections, the theory of topological insulators

is defined by mappings from the Brillouin zone (BZ) to the space of Bloch Hamiltonians, $\mathbf{k} \rightarrow \mathcal{H}(\mathbf{k})$.

A material with nontrivial bulk topological invariant has a bandstructure that cannot be continuously deformed to the vacuum without closing the energy gap. Because of this, when topological insulators are in contact with a trivial insulator the topological index across the interface changes discontinuously, leading to a closed gap with conducting states at the interface. These surface states are incredibly robust to perturbations, provided that the symmetry properties of the original model remain intact. The key property of topological materials is that *the topological index cannot be changed without closing the bandgap.* This is referred to as the bulk-edge correspondence because the properties of the bulk material dictate what happens at the edge.

The first topological insulator is widely recognized sa the 2D electron gas in the quantum hall regime, which has been studied since the 1980s. The quantum hall effect (QHE) breaks time-reversal symmetry ($\mathcal{T}$) due to the strong magnetic field needed to produce Landau levels. Newly discovered topologial insulators that do not break $\mathcal{T}$ were predicted in 2007 in both two and three dimensions and were experimentally observed shortly thereafter [4, 40]. The classification and discovery of topological materials is an ongoing area of research; at this time 3D topological insulators of the type considered here are theoretically well understood. In this Section we briefly review the classification of 3D $\mathcal{T}$-invariant TIs and discuss the low energy effective model of the 2D surface states. In Chapter 2 and Chapter 3 we discuss device applications of these materials by exploiting new physics at the interface between 3D TIs and magnetic materials.

In $\mathcal{T}$-invariant 3D TIs there are special points in the BZ where momentum is invariant under time reversal, referred to as time-reveral invariant momentum (TRIM). At these $\mathbf{k}$ points the bands are guaranteed to be doubly degenerate

because because $\mathbf{k} = -\mathbf{k}$ so $\mathcal{H}(-\mathbf{k}) = \mathcal{T}\mathcal{H}(\mathbf{k})\mathcal{T}^{-1} = \mathcal{H}(\mathbf{k})$ where $\mathcal{T}$ is the antiunitary time-reversal operator with $\mathcal{T}^2 = -1$. Pairs of bands are not guaranteed to be degenerate anywhere in the Brillouin zone except at the TRIM. 3D TIs are defined by four $\mathbb{Z}_2$ topological invariants $(\nu_0; \nu_1, \nu_2, \nu_3)$ which are related to the time-reversal polarization of the Hamiltonian at the TRIM [41–43]. The $\mathbb{Z}_2$ topological invariants classify how bands are paired as you traverse from one TRIM to another in the BZ. We focus on the "strong" topological insulator which has $\nu_0 = 1$, meaning that time-reversal polarization switches sign at an odd number of TRIM.

The actual mechanism that causes nontrivial topology in these materials is band inversion. That is, energy bands of opposite parity are inverted from the bare atomic energy levels due to crystal field splitting and spin-orbit coupling (SOC) in the material. This inversion can occur at different $\mathbf{k}$ points in the BZ. In the topological phase, bands are paired differently as you traverse the BZ, so you cannot find a path at any energy from one k point to another that does not intersect at least one band - this is the surface state. Strong SOC in the bulk is the primary source of band inversion for the first proposed TIs, so the first material candidates for 3D TIs were naturally those with high intrinsic SOC.

In general the $\mathbb{Z}_2$ invariants are difficult to compute for a given system because you have to know the parity of each Bloch wavefunction at every TRIM to determine if band inversion occurs. There are some materials including Bi_2Se_3, Bi_2Te_3, and Sb_2Te_3 where the band inversion occurs only at the Γ point, leading to a single surface state with a linear Dirac dispersion [40, 44, 45]. For these materials a simple effective surface theory can be derived, which we sketch below following Refs. [40, 44, 45]. Other materials, notably of the type Bi_xSb_{1-x}, have been proposed as TIs but cannot be described by this simple surface theory [40].

Surface Hamiltonian for 3D TIs

The low-energy effective theory for materials like Bi_2Se_3 with band inversion at the Γ point was developed based on first-principles calculations in [44, 45]. The Hamiltonian obeys time-reversal $\mathcal{T}$, inversion I, and C_3 rotation symmetry about the z axis, following the material crystal structure. Up to quadratic order in $\mathbf{k}$, the minimal four-band model for the 3D TI bulk is [45]

$$\mathcal{H}(\mathbf{k}) = \epsilon_0(\mathbf{k})\mathbb{I}_{4\times4} + \begin{pmatrix} \mathcal{M}(\mathbf{k}) & A_1k_z & 0 & A_2k_- \\ A_1k_z & -\mathcal{M}(\mathbf{k}) & A_2k_- & 0 \\ 0 & A_2k_+ & \mathcal{M}(\mathbf{k}) & -A_1k_z \\ A_2k_+ & 0 & -A_1k_z & -\mathcal{M}(\mathbf{k}) \end{pmatrix}, \tag{1.20}$$

where $k_\pm = k_x \pm ik_y$, $\epsilon_0(\mathbf{k}) = C + D_1k_z^2 + D_2k_\perp^2$, $\mathcal{M}(\mathbf{k}) = M - B_1k_z^2 - B_2k_\perp^2$, $k_\perp^2 = k_x^2 + k_y^2$ and $\mathbb{I}_{4\times4}$ is the 4×4 unit matrix. The constants $A_{1,2}$, $B_{1,2}$, C, $D_{1,2}$ and M are fitting parameters that depend on the material and in particular the strength of spin-orbit coupling. The second matrix in Eq. (1.20) is similar to the Dirac equation, where the momentum-dependent function $\mathcal{M}(\mathbf{k})$ is analogous to the Dirac mass. The basis for Eq. (1.20) is $\{|p1_z^+,\uparrow\rangle, |p2_z^-,\uparrow\rangle, |p1_z^+,\downarrow\rangle, |p2_z^-,\downarrow\rangle\}$, where $p1, p2$ denote hybridized p-orbital states of Bi-Se near the Fermi level with polarization $\pm$ and spin $\uparrow$ ($\downarrow$).

For $A_{1,2} \ll B_{1,2}, D_{1,2}$, Hamiltonian (1.20) is approximately diagonal with doubly-degenerate energy levels

$$E^+(\mathbf{k}) = C + M + (D_1 - B_1)k_z^2 + (D_2 - B_2)k_\perp^2 \tag{1.21}$$

$$E^-(\mathbf{k}) = C - M + (D_1 + B_1)k_z^2 + (D_2 + B_2)k_\perp^2. \tag{1.22}$$

In the "inverted" (topological) regime $M/B_{1,2} > 0$, we can see that $E^+ > E^-$ near $k = 0$, and $E^- > E^+$ at larger values of $\mathbf{k}$, indicating that the ordering of energy levels changes across the BZ.

Now, we derive the surface Hamiltonian following the procedure in Ref. [46] for the 2D quantum spin hall case. We consider $\mathcal{H}(\mathbf{k})$ on the half-plane $z > 0$, and split the Hamiltonian into parts dependent on k_z and $k_\perp$, $\mathcal{H}(\mathbf{k}) = \mathcal{H}_0(k_z) + \mathcal{H}_1(k_x, k_y)$ where

$$\mathcal{H}_0(k_z) = (C + D_1 k_z^2) + \begin{pmatrix} M - B_1 k_z^2 & A_1 k_z & 0 & 0 \\ A_1 k_z & -(M - B_1 k_z^2) & 0 & 0 \\ 0 & 0 & M - B_1 k_z^2 & -A_1 k_z \\ 0 & 0 & -A_1 k_z & -(M - B_1 k_z^2) \end{pmatrix} \tag{1.23}$$

$$\mathcal{H}_1(k_x, k_y) = D_2 k_\perp^2 \mathbb{I}_{4\times 4} + \begin{pmatrix} -B_2 k_\perp^2 & 0 & 0 & A_2 k_- \\ 0 & B_2 k_\perp^2 & A_2 k_- & 0 \\ 0 & A_2 k_+ & -B_2 k_\perp^2 & 0 \\ A_2 k_+ & 0 & 0 & B_1 k_\perp^2 \end{pmatrix} \tag{1.24}$$

At $k_x, k_y = 0$, $\mathcal{H}_1 = 0$ and we can solve for the eigenstates $\Psi(z)$ of $\mathcal{H}_0(k_z)$ with the open boundary condition $\Psi(z = 0) = 0$. Since translation symmetry is broken, k_z is no longer a good quantum number so $k_z \to -i\partial_z$. $\mathcal{H}_0(k_z)$ is block diagonal, so there will be two spinor eigenstates $\Psi_{\uparrow(\downarrow)}$ which are time-reversed pairs. $\Psi_\uparrow(z) = (\psi(z), 0, 0)^T$ with two component spinor $\psi(z) = (\psi_1, \psi_2)^T$. The problem reduces to solving the eigenvalue equation

$$\left[(C - D_1 \partial_z^2)\mathbb{I}_{2\times 2} + \begin{pmatrix} M + B_1 \partial_z^2 & -iA_1 \partial_z \\ -iA_1 \partial_z & -M - B_1 \partial_z^2 \end{pmatrix} \right] \psi(z) = E\psi(z). \tag{1.25}$$

The first term in Eq. (1.25) does not affect the topological properties because it is the same for both $E^{\pm}$ and does not contribute to band inversion. For clarity, we ignore this term to show how the localized surface states are constructed. The second term in Eq. (1.25) is particle-hole symmetric, guaranteed to have a solution with eigenvalue $E = 0$. These zero-energy surface states should be exponentially localized along the surface perpendicular to z. We posit that $\psi = e^{\lambda z}(\psi_1, \psi_2)^T$, giving the eigenvalue equation

$$(M + B_1\lambda^2)\sigma^y\psi = -A_1\lambda\psi, \tag{1.26}$$

where σ^y is the usual y Pauli matrix. The most general solution obeying the boundary condition $\psi(0) = 0$ is then [45]

$$\psi_0(z) = a(e^{\lambda_1 z} - e^{\lambda_2 z})\psi_- + b(e^{-\lambda_1 z} - e^{-\lambda_2 z})\psi_+ \;\; ; \;\; \lambda_{1,2} = \frac{A_1 \pm \sqrt{A^2 - 4MB_1}}{2B_1}, \tag{1.27}$$

where a, b are normalization coefficients and $\psi_\pm$ are the typical eigenstates of σ^y $\psi_\pm = (\psi_1 \pm i\psi_2)/\sqrt{2}$ with $\sigma^y\psi_\pm = \pm\psi_\pm$. With this form of ψ, $\mathrm{Re}\,[\lambda_{1,2}]$ must be the same sign to have a normalizable solution. For $A_1/B_1 > 0$ we have $\mathrm{Re}\,[\lambda_{1,2}] > 0$ so $a = 0$ and $b = 1$. Finally, we project the full Hamiltonian onto these eigenstates for find the surface model $\mathcal{H}_{\mathrm{surf}}(k_\perp)$, where $\mathcal{H}^{\alpha\nu}_{\mathrm{surf}}(k_\perp) = \langle\Psi_\alpha|\mathcal{H}_0 + \mathcal{H}_1|\Psi_\nu\rangle$. This gives

$$\mathcal{H}_{\mathrm{surf}}(k_x, ky) = A_1(k_x\sigma^y - k_y\sigma^x) + \mathcal{O}(\mathbf{k}^2) \tag{1.28}$$

where $\sigma^{x,y}$ corresponds to the real spin of the surface states [45]. Usually it is written $\mathcal{H}_{\mathrm{surf}}(k_x, ky) = v_{\mathrm{F}}(\mathbf{k} \times \boldsymbol{\sigma})$ where $v_{\mathrm{F}} \approx A_1/h$ is the Fermi velocity.

Hamiltonian (1.28) is the celebrated single Dirac cone, which occurs on the surface of Bi_2Se_3 and some other topological materials. The surface states have a linear dispersion $\epsilon(k) = \pm v_{\mathrm{F}}k$ and a helical spin texture as shown in Figure 1.6.

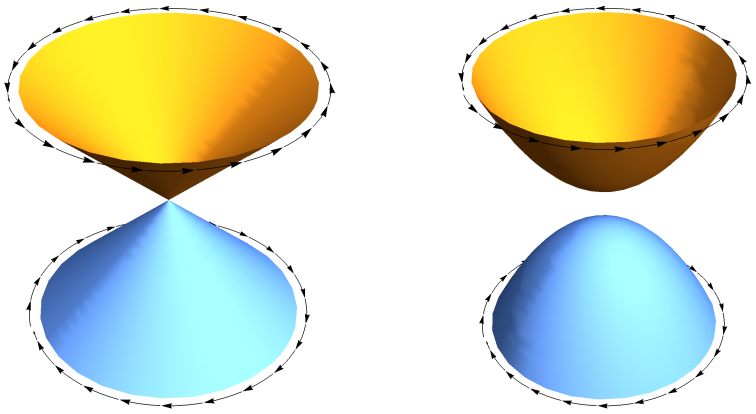

FIGURE 1.6: Dispersion relation $\epsilon(k)$ of 3D TI surface states in the (k_x, k_y) plane. (Left) $\mathcal{T}$ is preserved. The dispersion is linear and gapless with a helical spin texture. (Right) $\mathcal{T}$ is broken. The dispersion is gapped and quadratic, but retains the helical spin texture. The spin textures have opposite helicity on the upper and lower bands.

The surface states exhibit spin-momentum locking, therefore perturbations coupling to spin can affect the electronic structure and properties of the material. As long as $\mathcal{T}$ is preserved, the surface states remain gapless. However, if $\mathcal{T}$ is broken a gap opens in the system. We can see this by the addition of a magnetic field, which adds a Zeeman term $\mathcal{H}_B \propto \Delta\sigma^z$ where $\Delta = g\mu_b B$ to Hamiltonian (1.28), giving energy levels $\epsilon(k) = \pm\sqrt{v_F^2 k^2 + \Delta^2}$. The same effect is produced by proximity coupling to a ferromagnetic layer [47]. Due to the spin-momentum locking, novel magneto-optical effects appear when $\mathcal{T}$ is broken, such as the universal Faraday effect and resonant Kerr effects [48–50].

1.3 Physical Systems: Bose-Einstein Condensates

For a Bose gas at sufficiently low temperatures, nearly all particles occupy a single eigenstate, leading to a macroscopically occupied quantum-coherent "matter

wave". BECs were first observed in trapped atoms in 1995 [51]; they exhibit numerous interesting features including superfluidity and interference effects, even in the presence of interactions [52]. Topological defects such as vortices and solitons also occur in BECs depending on the dimensionality of the atom cloud. Additionally, spinor BECs have an internal degree of freedom and provide an ideal experimental test-bed for studying quantum magnetism and other condensed matter phenomena. In this Section we review dark solitons and spinor BECs, which are essential to results presented in Chapter 4 and Chapter 5. First, we briefly discuss the mean-field theory of BECs.

The real-space Hamiltonian of a single-component interacting Bose gas is

$$\hat{\mathcal{H}} = \int d\mathbf{r}d\mathbf{r}' \left[\hat{\Psi}^\dagger(\mathbf{r})\left(-\frac{\hbar^2}{2m}\nabla^2 + V_{\text{ext}}(\mathbf{r})\right)\hat{\Psi}(\mathbf{r}) + \hat{\Psi}^\dagger(\mathbf{r}')\hat{\Psi}^\dagger(\mathbf{r})V_{\text{int}}(\mathbf{r}-\mathbf{r}')\hat{\Psi}(\mathbf{r})\hat{\Psi}(\mathbf{r}')\right]. \tag{1.29}$$

Where $\hat{\Psi}^{(\dagger)}$ are bosonic field operators which obey the typical commutation relations

$$\left[\hat{\Psi}(\mathbf{r}), \hat{\Psi}^\dagger(\mathbf{r}')\right] = \delta(\mathbf{r}-\mathbf{r}'). \tag{1.30}$$

$V_{\text{ext}}(\mathbf{r})$ is an external potential, and m is the mass of individual atoms. We only take s-wave collisions into account and assume a local pairwise interaction potential

$$V_{\text{int}}(\mathbf{r}-\mathbf{r}') = \frac{g}{2}\sum_{i\neq j}\delta(\mathbf{r}_i - \mathbf{r}'_j), \tag{1.31}$$

with effective interaction parameter $g = 4\pi\hbar^2 a_s/m$ where a_s is the s-wave scattering length. In general a_s can be repulsive ($a_s > 0$) or attractive ($a_s < 0$), unless otherwise noted we consider the repulsive case in this thesis. Under the mean-field approximation, we take $\langle\hat{\Psi}\rangle \to \psi$ where the order parameter $\psi(\mathbf{r},t)$ is a $U(1)$ field, $\psi(\mathbf{r},t) = \sqrt{n(\mathbf{r},t)}e^{i\theta(\mathbf{r},t)}$ where $n(\mathbf{r},t)$ is the condensate density and $\theta(\mathbf{r},t)$ is the phase. The order parameter, also referred to as the "macroscopic wavefunction"

of the BEC, is normalized to the number of particles

$$N = \int d\mathbf{r}\ |\psi|^2. \tag{1.32}$$

Mean-field theory assumes that the lowest energy state is macroscopically occupied and that other, higher energy states are unimportant. The gas parameter na^3 is figure of merit here, mean-field theory is only applicable for $na^3 \ll 1$. From Hamiltonian (1.29) the condensate order parameter obeys the equation of motion

$$i\hbar\frac{\partial\psi(\mathbf{r},t)}{\partial t} = \left(-\frac{\hbar^2}{2m}\nabla^2 + V_{\text{ext}}(\mathbf{r}) + g|\psi(\mathbf{r},t)|^2\right)\psi(\mathbf{r},t). \tag{1.33}$$

Eq. (1.33) is known as the Gross-Pitaevskii equation (GPE) and has a non-linear part resulting from the interaction term. In the following we consider a harmonic external trapping potential with different trapping frequencies along each axis, $V_{\text{ext}}(\mathbf{r}) = m/2(\omega_x^2x^2 + \omega_y^2y^2 + \omega_z^2z^2)$.

1.3.1 Dark Solitons

In confined geometries Eq. (1.33) admits spatially nonuniform vortex and soliton solutions. From the 3D GPE in Eq. (1.33) there are several competing length scales: s-wave scattering length a_s, condensate healing length $\xi = \hbar/\sqrt{2}mc$ where c is the condensate speed of sound, and the effective harmonic oscillator length scales $a_{x,y,z} = \sqrt{\hbar/m\omega_{x,y,z}}$. We consider a strongly anisotropic "cigar" trap such that $\omega_z \ll \omega_\perp$ where $\omega_\perp = \omega_{x,y}$.

In the quasi-1D case for a weakly interacting gas we assume that $a_s, a_\perp < \xi \ll a_z$ where $a_\perp = \sqrt{a_x^2 + a_y^2}$ such that the order parameter can be separated into components according to cylindrical variables, $\psi(\mathbf{r},t) = \tilde{\psi}(z)F(r,\theta)$. We

assume that $F(r,\theta) \sim 1/a_\perp e^{-r^2/2a_\perp^2}$ is the ground state harmonic-oscillator wave-function and that no higher transverse modes are occupied. Then, we can integrate Eq. (1.33) over the transverse direction giving the effective 1D interaction strength $\tilde{g} \approx g/2\pi a_\perp^2$. A similar procedure can be employed for the quasi-2D case.

Upon dimensional reduction, the condensate order parameter obeys the 1D GPE,

$$i\hbar\frac{\partial\psi(x,t)}{\partial t} = \left(-\frac{\hbar^2}{2m}\frac{\partial^2}{\partial x^2} + g|\psi(x,t)|^2\right)\psi(x,t). \tag{1.34}$$

To construct the soliton solution we seek a time-dependent spatially localized order parameter of the form $\psi(x,t) = \sqrt{n_c}\tilde{\varphi}(x-vt)e^{-i\mu t/\hbar}$, where $\tilde{\varphi}$ only depends on time through the coordinate $x - vt$ and n_c uniform density of the condensate as $x \to \infty$. Then we can make a Galilean transformation $\tilde{x} = (x - vt)/\xi$ on the original equation to find a time-independent equation

$$\frac{2im\xi}{\hbar}\frac{\partial\tilde{\varphi}}{\partial\tilde{x}} = \frac{\partial^2\tilde{\varphi}}{\partial\tilde{x}^2} + \tilde{\varphi}(1-|\tilde{\varphi}|^2). \tag{1.35}$$

The boundary conditions on $\tilde{\varphi}$ are $|\tilde{\varphi}| \to 1$, $\partial\tilde{\varphi}/\partial\tilde{x} \to 0$ as $\tilde{x} \to \pm\infty$. This equation can be solved by writing $\tilde{\varphi} = \tilde{\varphi}_1 + i\tilde{\varphi}_2$ and solving for $\tilde{\varphi}_1$ with constant $\tilde{\varphi}_2$ [53]. The final solution is

$$\psi(x,t) = \sqrt{n_c}\left[i\frac{v}{c} + \gamma_s \tanh\left(\gamma_s\frac{x-vt}{\sqrt{2}\xi}\right)\right]e^{-i\frac{\mu t}{\hbar}} \tag{1.36}$$

where $\gamma_s^2 = 1 - v^2/c^2$. The density is

$$n(x-vt) = \frac{n_c v^2}{c^2} + n_c\gamma_s^2\tanh^2\left[\frac{x-vt}{\sqrt{2}\xi}\gamma_s\right] \tag{1.37}$$

Eqs. (1.36) and (1.37) are exact solutions which describe a dark soliton in a $1D$ condensate. The soliton depth at the lowest point is $n(0) = n_c v^2/c^2$. It is a

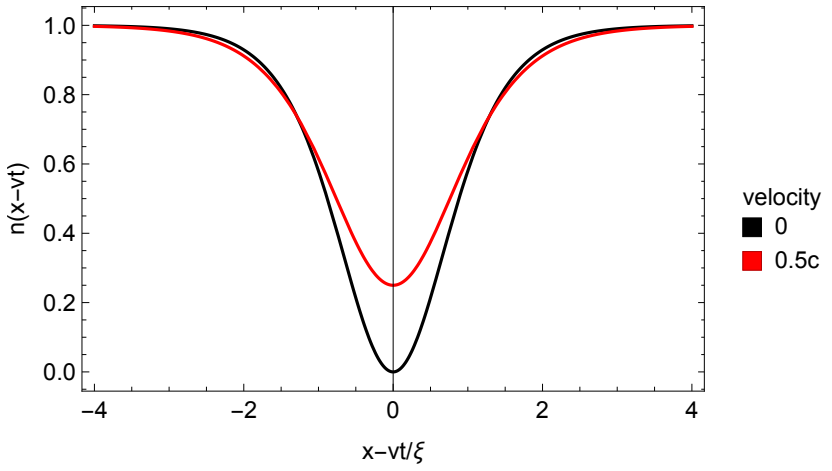

FIGURE 1.7: Density profile of a dark soliton in a uniform condensate. The soliton is a density depletion where the minimum depth is related to the soliton velocity relative to the speed of sound in the condensate.

density depletion in the condensate, for this reason it is called a *dark* soliton. For a stationary soliton ($v = 0$) the density goes to zero, this is referred to as a *black* soliton. The soliton with is given by $w \approx \xi/\gamma_s$, which is set by the healing length but also depends on velocity. The faster the soliton goes the more shallow it is, as shown in Figure 1.7 for the density profile of the dark soliton at two different speeds. The change in condensate phase from one side of the soliton to the other is

$$\Delta S_{\pm\infty} = 2 \arccos\left(\frac{v}{c}\right). \tag{1.38}$$

Black solitons have the largest phase jump with $\Delta S = \pi$. The energy of the soliton on top of the uniform condensate is found by subtracting the uniform background,

$$\mathcal{E}_s = \int d\tilde{x} \frac{\hbar^2}{2m} \left|\frac{\partial \psi}{\partial \tilde{x}}\right|^2 + \frac{g}{2}\left(|\psi|^2 - n\right)^2 = \frac{4}{3}\hbar c n \left(1 - \frac{v^2}{c^2}\right)^{3/2}. \tag{1.39}$$

The energy of this configuration has the peculiar property that the soliton can lower its energy by increasing its speed. This makes it thermodynamically unstable and also leads to unconventional behavior in the presence of friction, which we explore in detail in Chapter 4.

The one-dimensional dark soliton is sometimes referred to as a "kink" state and is a global excitation of the system on top of the uniform ground state. It is not a topological defect in the same sense as skyrmions and vortices because there is no homotopy classification for a single spatial dimension without a well-defined contour in order parameter space. However, the dark soliton is a remnant of quantized vortices, true topological defects that occur in quasi-2D BECs. If the transverse confinement is not tight enough, the longitudinal and transverse modes of the condensate order parameter can couple, leading to a "snake" instability of the soliton [54]. As the transverse width of the condensate increases, dark solitons decay into solitonic vortices and eventually into vortex pairs, behavior which has been observed both numerically and in experiments [55–57]. Here we briefly introduce the 2D vortex solution since it is related to soliton decay.

In the quasi-2D case the order parameter $\psi(r,\theta) = |\psi_0(r)|e^{in\theta}e^{-i\mu t/\hbar}$ is mathematically equivalent to the one considered in Section 1.2.2 for two-dimensional magnets with an additional global phase set by the chemical potential μ. The condensate supports quantized vortices with

$$\oint \nabla\theta \cdot dl = 2\pi n, \tag{1.40}$$

where n is the winding number. The amplitude ψ_0 of the order parameter obeys the radial equation

$$-\frac{\hbar^2}{2m}\frac{1}{r}\frac{\partial}{\partial r}\left(r\frac{\partial\psi_0}{\partial r}\right) + \frac{\hbar^2 n^2}{2mr^2}\psi_0 + \tilde{g}\psi_0^3 - \mu\psi_0 = 0 \tag{1.41}$$

which possesses the asymptotic solutions $\psi_0 \sim r^{|n|}$ as $r \to 0$, so the density of the gas is zero in the center of the vortex and the phase "winds" from $-\pi$ to π around the vortex center [58].

1.3.2 Spin-1 Condensates

In atomic species with more than one relevant hyperfine level and total spin F, the condensate order parameter takes on an additional discrete hyperfine index $\psi_{m_F}(\mathbf{r}, t) = \psi(\mathbf{r}, t)|m_F\rangle$ where $|m_F\rangle$ is a spinor with $2F + 1$ components. In this case the Hamiltonian becomes a matrix

$$\hat{\mathcal{H}} = \int d\mathbf{r} d\mathbf{r}' \left[\hat{\Psi}^\dagger_\alpha(\mathbf{r}) \left(-\frac{\hbar^2}{2m} \nabla^2 \delta_{\alpha\beta} + V^{\alpha\beta}_{\text{ext}}(\mathbf{r}) \right) \hat{\Psi}_\beta(\mathbf{r}) \right.$$
$$\left. + \hat{\Psi}^\dagger_\alpha(\mathbf{r}') \hat{\Psi}^\dagger_\beta(\mathbf{r}) V^{\alpha\beta\gamma\nu}_{\text{int}}(\mathbf{r} - \mathbf{r}') \hat{\Psi}_\gamma(\mathbf{r}) \hat{\Psi}_\nu(\mathbf{r}') \right]. \tag{1.42}$$

The external potential may be spin-independent or spin-dependent. We consider an isolated $F = 1$ manifold with hyperfine states $m_F = \{-1, 0, 1\}$. This theory describes condensates in alkali gases (i.e. ^{87}Rb, ^{23}Na, etc.); here we enumerate some ground-state properties of the condensate. In Chapter 5 we consider a spin-1 condensate in an optical lattice with spin-orbit coupling as a cold atom realization of the QHE.

For the particle interaction potential we still restrict ourselves to s-wave interactions. However, the scattering length for pairwise interactions depends on the total spin F_{tot} of the scattered atom pair. The local interaction potential in Equation 1.31 is modified to

$$V_{\text{int}}(\mathbf{r} - \mathbf{r}') = \frac{1}{2} \sum_{i \neq j} \delta(\mathbf{r}_i - \mathbf{r}'_j) \sum_{F_{\text{tot}}} g_F \mathcal{P}_F, \tag{1.43}$$

where $\mathcal{P}_F$ is a projection operator onto states with total spin F and $g_F = 4\pi\hbar^2 a_F/m$ is the interaction strength in the spin-F channel with s-wave scattering length a_F [59]. For s-wave interactions the wavefunction must be symmetric under particle exchange so states with odd total spin are not allowed, restricting us to $F_{\text{tot}} = 0, 2$. Using the properties of projection operators and addition of angular momentum, we have the following relations [60]

$$V_{\text{int}} \propto g_0\mathcal{P}_0 + g_2\mathcal{P}_2 \tag{1.44}$$

$$\mathbb{I} = \sum_{F_{\text{tot}}} \mathcal{P}_F = \mathcal{P}_0 + \mathcal{P}_2 \tag{1.45}$$

$$\hat{\mathbf{F}}_1 \cdot \hat{\mathbf{F}}_2 = \sum_{F_{\text{tot}}} \left[\frac{1}{2}F_{\text{tot}}(F_{\text{tot}}+1) - F(F+1)\right] \mathcal{P}_{F_{\text{tot}}} = \mathcal{P}_0 - 2\mathcal{P}_2. \tag{1.46}$$

From this, the spin-dependent interaction between two atoms can be re-written with spin-independent and spin-dependent terms separated as

$$V_{\text{int}}(\mathbf{r}-\mathbf{r}') = \frac{1}{2}\sum_{i\neq j} \delta(\mathbf{r}_i - \mathbf{r}'_j)\left[c_0\mathbb{I}_1 \otimes \mathbb{I}_2 + c_2\hat{\mathbf{F}}_1 \otimes \hat{\mathbf{F}}_2\right], \tag{1.47}$$

where $\hat{\mathbf{F}}$ denotes a vector of spin-1 matrices, $c_0 = (g_0+2g_2)/3$, and $c_2 = (g_2-g_0)/3$. In particular, c_2 can be positive or negative depending on the relative values of g_2 and g_0. Atoms with $g_2 > g_0$, like ^{23}Na, have repulsive spin-dependent interactions are are referred to as polar or antiferromagnetic condensates, while atoms with $g_2 < g_0$, like ^{87}Rb, have attractive spin-dependent interactions and are referred to as ferromagnetic condensates. The interaction term preserves $SU(2)$ rotational symmetry.

The mean-field ground state is very different depending on the sign of c_2 (we assume c_0 is always positive) [59]. For ferromagnetic condensates, $|m_F\rangle \propto (1,0,0)^T$ up to an overall phase; ferromagnetic ground states maximize $\langle\hat{\mathbf{F}}\rangle$ such that

$|\langle\hat{\mathbf{F}}\rangle|/N = 1$. For antiferromagnetic condensates, the ground state is longitudinal $|m_F\rangle \propto (0,1,0)^T$ or transverse $|m_F\rangle \propto (1/\sqrt{2}, 0, e^{i\varphi}/\sqrt{2})^T$ polar with $\langle\hat{\mathbf{F}}\rangle = 0$. In the absence symmetry-breaking perturbations, these ground states are independent of interaction strength and only depend on the sign of c_2 [60].

In an ideal uniform system the spin-1 Hamiltonian can be solved exactly [61, 62]. Unlike the mean-field solution, the exact ground state exhibits fragmentation, where multiple eigenstates of $\hat{\mathcal{H}}$ have macroscopic occupation. Fragmentation is analogous to a superposition of mean-field condensates. The ferromagnetic and polar phases still maximize or minimize $\langle\hat{\mathbf{F}}\rangle$, respectively, but they also exhibit large fluctuations. However, these fragmented states are very sensitive to symmetry breaking perturbations such as a magnetic field gradient or quadratic Zeeman effects and rapidly approach the mean-field solution in experimentally relevant set-ups [60, 62].

1.4 Overview of the Thesis

In Chapter 2 we consider a ferromagnet with a single magnetic skyrmion proximity coupled to the surface of a 3D TI. We analytically solve the Dirac equation in the presence of the skyrmion to find the exact eigenstates and energy spectrum of the Dirac surface states. Away the from the skyrmion radius the energy spectrum is gapped due to out-of-plane magnetic moments, but there exist bound states localized at the skyrmion radius where out-of-plane magnetization is zero. Magnetic confinement of the Dirac electrons results in a charged skyrmion, which can be manipulated with an external electric field. We model the skyrmion dynamics using a classical equation of motion and propose the first mechanism of all-electric skyrmion driving. Chapter 2 was previously published in Physical Review B,

Chapter 3 considers coupling a TI to an XY-magnet where all magnetic moments are in-plane, so the linear Dirac spectrum is preserved. We show that the magnetic vortices act like a random magnetic field (RMF) on the Dirac surface states. Our proposed TI-XY magnet heterostructure is the first controllable solid-state realization of a Dirac Hamiltonian with RMF disorder. Dirac fermions in a RMF have been a subject of theoretical study for decades; their localization properties for long-range correlated disorder are unknown. We show that a TI-XY magnet heterostructure would be an ideal way to test the properties of this model in a controlled setting. We predict transport signatures of the magnetic transition using diagrammatic perturbation theory to derive the effective action of the Dirac fermions. We find that the TI resistivity increases strongly near the BKT transition temperature due to unscreened magnetic fluctuations. Furthermore, perturbation theory breaks down for the purely linear Dirac energy spectrum. We show how to properly regularize the theory by taking into account naturally occurring band curvature in the TI. Thus, we clarify the limits on analogies between TI surface states and Dirac fermions in free space, where for the latter the theory is regularized differently. Chapter 3 was previously published in Physical Review B,

In Chapter 4 we transition to studying topological defects in cold atom systems. We propose a way to introduce and control friction in a system with a dark soliton. Thermal impurities are introduced into the system, and they scatter off of the soliton, inducing friction. Dark solitons behave like heavy classical particles but with an important caveat: they have a negative effective mass. Using scattering theory, we calculate the exact friction coefficient from a microscopic model of quantum impurity scattering. We develop a theory of soliton dynamics and find the exact time-dependent probability distribution function (PDF) for dark solitons by solving a Fokker-Planck equation, including friction and a harmonic

trap. We show that the soliton undergoes "emergent" Brownian motion only if contained in a harmonic trap. Soliton trajectories spread linearly in time with a diffusion coefficient *proportional* to the friction coefficient, unlike the typical case where diffusion is inversely proportional to friction. We also propose a way to tune friction in this system using accessible experimental probes. With the exception of Section 4.7, Chapter 4 was previously published in Physical Review A, © American Physical Society, 2017. Section 4.7 is based off of Ref. [63] published in Proceedings of the National Academies of Sciences (PNAS), © PNAS, 2017.

Chapter 5 is devoted to an ultracold atom realization of the QHE using a 1D spin-1 condensate in an optical lattice with spin-orbit coupling. This type of set-up can be mapped to a 2D square lattice with uniform magnetic flux through each plaquette, where the second "synthetic" dimension is made up of the discrete internal spin states of the BEC [64]. Following experimental realization of this system in Ref. [65], we study how interactions affect the ground state phases of this system and in particular we show how interactions affect transport signatures of the QHE. We numerically solve the Gross-Pitaevskii equation (GPE) for different types of interactions, finding new interaction driven density-wave and spin-density-wave phases with clear experimental signatures. Our work shows how interactions affect the ground state phases in the synthetic dimensions picture. Chapter 5 was previously published in Physical Review A, © American Physical Society, 2016. We conclude the dissertation in Chapter 6.

Chapter 2: Charged Skyrmions on the Surface of a Topological Insulator

2.1 Overview

In this Chapter we show that a skyrmion texture in an insulating helimagnet, proximity coupled to TI surface, can become charged due to Dirac surface states localized at the skyrmion radius. In Section 2.2 we examine the electronic spectrum of TI surface states in contact with a skyrmion magnetic texture, both with and without an external magnetic field. We show that the number of localized states can be controlled by an external magnetic field, which is needed for skyrmion phase stabilization, and in realistic conditions there are a few localized states. In Section 2.3 we investigate the classical equation of motion of a single charged skyrmion. Experimentally accessible electric fields can drive individual charged skyrmions in insulating materials at speeds comparable to those seen in metallic systems. We show the first mechanism of manipulating skyrmions in thin films directly via electric field, which opens the door to further investigation of skyrmion manipulation without relying on the spin transfer torque (STT) mechanism. This chapter was previously published in Physical Review B,

2.2 Electronic Spectrum of TI Surface States

2.2.1 Model

In the presence of the skyrmion texture $\mathbf{n}(\mathbf{r})$ and external perpendicular magnetic field $B\hat{e}_z$, corresponding to the vector potential $\mathbf{A} = B(x\hat{e}_y - y\hat{e}_x)/2$, the surface states of a TI can be described by the Hamiltonian

$$\mathcal{H} = v_{\mathrm{F}} \left[\left(\mathbf{p} - \frac{e}{c}\mathbf{A} \right) \times \boldsymbol{\sigma} \right]_z - \Delta_{\mathrm{S}} \mathbf{n}(\mathbf{r}) \cdot \boldsymbol{\sigma} - \Delta_{\mathrm{Z}} \sigma^z. \tag{2.1}$$

Here v_{F} is the Fermi velocity, $\boldsymbol{\sigma}$ is the vector of Pauli matrices, corresponding to electron's spin, $\Delta_{\mathrm{Z}} = g_{\mathrm{TI}}\mu_b B$ is the Zeeman shift due to the external field, and $\Delta_{\mathrm{S}} > 0$ parametrizes ferromagnetic exchange coupling between the thin film and TI surface [47]. The out-of plane component of the magnetic texture $\mathbf{n}_z(\mathbf{r})$ plays the role of position dependent Dirac mass, while the in-plane component $\mathbf{n}_{||}$ can lead to an emergent magnetic field $B_{\mathrm{S}}(\mathbf{r}) = c\Delta_{\mathrm{S}} \mathrm{div}\mathbf{n}_{||}(\mathbf{r})/e\hbar v_{\mathrm{F}}$. A skyrmion stabilized by Dzyaloshinskii-Moriya (DM) interaction, as it is for insulating helical magnets, has a solinoidal in-plane magnetization, shown in Figure 2.1-a. Therefore, its magnetic texture can be parametrized by

$$\mathbf{n}(\mathbf{r}) = (-\sin\varphi\sqrt{1 - n_z^2(\mathbf{r})}, \cos\varphi\sqrt{1 - n_z^2(\mathbf{r})}, n_z(\mathbf{r})).$$

In this case the emergent magnetic field B_{S} is zero and the in-plane component of magnetic texture only shifts the location of the Dirac point in momentum space. For our purposes, we can remove the in-plane magnetization using a gauge transformation. Details of the gauge transformation are given in Appendix A.

For the out-of-plane component we will use the hard-wall approximation $n_z(r) = 2\Theta(r - R_{\mathrm{S}}) - 1$, where R_{S} is the skyrmion radius. The applicability

of this approximation is justified below. In materials where skyrmions are stabilized via DM interaction the radius of the skyrmion is not dependent on the external magnetic field. Rather, skyrmion radius depends on the relative strength of the Heisenberg and DM exchange interactions which in turn depends on the material parameters [26]. In the following we therefore regard the skyrmion radius as an independent parameter.

The Hamiltonian conserves total momentum, and the wave function spinor can be presented as

$$\Psi(r,\varphi) = \frac{1}{\sqrt{2\pi}} \begin{pmatrix} F_m(r)e^{im\varphi} \\ G_m(r)e^{i(m+1)\varphi} \end{pmatrix}, \tag{2.2}$$

where m is the orbital momentum quantum number connected with the total momentum of Dirac particles as $j = m + \frac{1}{2}$. The radial wave functions $F_m(r)$ and $G_m(r)$ with energy E satisfy the Schrödinger equation

$$\begin{pmatrix} -\Delta_S n_z^\nu - \Delta_Z - E & \frac{v_F eB}{2c} r - \hbar v_F \frac{\partial}{\partial r} \\ \frac{v_F eB}{2c} r + \hbar v_F \frac{\partial}{\partial r} & \Delta_S n_z^\nu + \Delta_Z - E \end{pmatrix} \begin{pmatrix} F_m^\nu \\ G_m^\nu \end{pmatrix} - \begin{pmatrix} 0 & \hbar v_F \frac{m+1}{r} \\ \hbar v_F \frac{m}{r} & 0 \end{pmatrix} \begin{pmatrix} F_m^\nu \\ G_m^\nu \end{pmatrix} = 0. \tag{2.3}$$

Here $\nu = \pm$ for wave function of electrons outside and inside the skyrmion, where $n_z^\pm = \pm 1$. The matrix equation (2.3) can be rewritten in as the following system of equations,

$$\rho^2 \frac{\partial^2 F_m^\nu}{\partial \rho^2} + \rho \frac{\partial F_m^\nu}{\partial \rho} - \left[b^2\rho^4 + \rho^2((n_z^\nu + \delta)^2 - \epsilon^2 - 2b(m+1)) + m^2 \right] F_m^\nu = 0 \tag{2.4}$$

$$G_m^\nu = \frac{1}{\epsilon - (n_z^\nu + \delta)} \left[\frac{\partial F_m^\nu}{\partial \rho} - \frac{m}{\rho} F_m^\nu + b\rho F_m^\nu \right], \tag{2.5}$$

with dimensionless quantities $\rho = \Delta_S r/\hbar v_F$, $\epsilon = E/\Delta_S$, $\delta = \Delta_Z/\Delta_S$, and $b = B/B_0$ where $B_0 = 2\Delta_S^2 c/\hbar v_F^2 e$. We seek bound state solutions of these equations using the

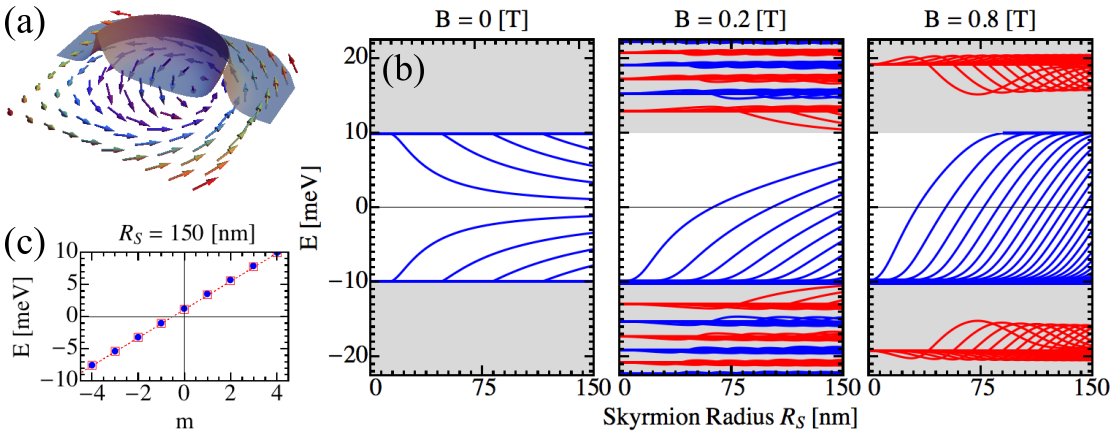

FIGURE 2.1: (a) Sketch of the wave function $|\Psi(r,\varphi)|^2$ (gray) of a TI surface state localized at the skyrmion radius. For clarity we plot $|\Psi|^2$ for $0 < \varphi < \pi$ only. The vector field represents the direction of local magnetization $\hat{\mathbf{n}}(\mathbf{r})$ of the skyrmion. (b) Electronic spectrum of TI surface proximity coupled to the skyrmion texture as a function of skyrmion radius and magnetic field. Without magnetic field states with orbital quantum number $|m| \leq 4$ are presented. With magnetic field $B = 0.2$ T states with $|m| \leq 10$ are presented, and with magnetic field $B = 0.8$ T states with $|m| \leq 25$ are presented. Without magnetic field localized states split from continuous bands $|E| \geq \Delta_\mathrm{S}$ in pairs. In the presence of an external magnetic field localized states split from the zeroth Landau level, which has the energy $E_{0m} = -\Delta_\mathrm{S} - \Delta_\mathrm{Z}$ and is highly degenerate. Higher energy LLs are also shown. (c) The energy of bound states as a function of m at large skyrmion radius R_S without magnetic field. Numerical solution (blue circles) from Equation (2.3) matches almost exactly with the semiclassical quantization (red squares) as in Equation (2.7).

following boundary conditions: $F_m^-(\rho), G_m^-(\rho)$ are regular at the origin as $\rho \to 0$, $F_m^+(\rho), G_m^+(\rho) \to 0$ as $\rho \to \infty$, and finally continuity of the Dirac wave function at the skyrmion radius R_S results in the boundary condition $F_m^+(R_\mathrm{S}) = F_m^-(R_\mathrm{S})$ and $G_m^+(R_\mathrm{S}) = G_m^-(R_\mathrm{S})$.

The energy at the skyrmion radius for each value of m is numerically calculated

by solving the transcendental equation

$$\frac{G_m^-(R_\mathrm{S})}{F_m^-(R_\mathrm{S})} = \frac{G_m^+(R_\mathrm{S})}{F_m^+(R_\mathrm{S})},$$

generating the spectra shown in Figure 2.1-b. We consider the skyrmion radius and external magnetic field to be separate controlling parameters of the surface state energy. Although skyrmions are usually stabilized in the presence of an external magnetic field, it is instructive to consider at first the electronic spectrum without it.

For the following calculations we use $v_\mathrm{F} \approx 0.5 \times 10^6$ m/s and $g_\mathrm{TI} \approx 5$, corresponding to the TI material Bi_2Se_3, and exchange coupling $\Delta_\mathrm{S} = 10$ meV. Insulating skyrmions with radius $R_\mathrm{S} \approx 25$ nm have been stabilized in Cu_2OSeO_3 films [22, 66–68] at low temperatures $T < 40$ K and for magnetic fields 0.05 T $\leq B \leq 0.2$ T.

2.2.2 Without Magnetic Field

At $B = 0$ the skyrmion texture does not modify the continuous gapped spectrum $|E| \geq \Delta_\mathrm{S}$ [69]; if the skyrmion radius exceeds the critical radius $R_\mathrm{S}^* = \hbar v_\mathrm{F}/2\Delta_\mathrm{S}$ it can lead to the appearance of localized states as presented in Figure 2.1-b for $B = 0$ T. The localized states appear in pairs, since the Dirac Hamiltonian possesses electron-hole symmetry $\{H_\mathrm{D}, \hat{\mathrm{K}}\} = 0$ with $\hat{\mathrm{K}} = \sigma^x \mathcal{C}$ where $\mathcal{C}$ is complex conjugation. The states are localized in the vicinity of the skyrmion radius R_S, as presented in Figure 2.1-a with length $r = \hbar v_\mathrm{F}/\Delta_\mathrm{S}$ or $\rho = 1$. These states are well split from the continuous bands and are bound to the skyrmion in case of its motion. Equation (2.4) reduces to Bessel's equation, resulting in (unnormalized)

wavefunctions

$$\Psi_m^- \propto \begin{bmatrix} (\epsilon - n_z^-)\mathcal{I}_m(k\rho) \\ \mathcal{I}_{m+1}(k\rho) \end{bmatrix}; \Psi_m^+ \propto \begin{bmatrix} (\epsilon - n_z^+)\mathcal{K}_m(k\rho) \\ \mathcal{K}_{m+1}(k\rho) \end{bmatrix}, \tag{2.6}$$

where $k^2 = n_z^2 - \epsilon^2$ and $\mathcal{I}_m$ and $\mathcal{K}_m$ are modified Bessel functions of the the first and second kind, respectively.

The second term in Equation (2.3) originates from the angular motion and can be neglected if $R_\mathrm{S} \gg 2mR_\mathrm{S}^*,\ 2(m+1)R_\mathrm{S}^*$. In that case the system of equations Equation (2.3) can be reduced to the system of supersymmetric Schrödinger equations (SUSY) by squaring $\mathcal{H}$ to solve $\mathcal{H}^2\Psi_m = E_m^2\Psi_m$, with the SUSY superpotential $W(x) = \Delta_\mathrm{S} n_z(r)$, as it is for a domain wall [70, 71]. The SUSY nature of the equations guarantees the presence of a localized state for every angular momentum. Their presence is not sensitive to the shape of the skyrmionic texture $n_z(R)$, so the physics is well captured by the hard-wall anzatz in the $R_\mathrm{S} \gg R_\mathrm{S}^*$ regime. When the the angular motion becomes important, at $R_\mathrm{S} \approx R_\mathrm{S}^*$, the reduction to SUSY is lost and localized states are pushed to the continuum. The energy gain due to the localization becomes smaller than additional kinetic energy due to orbital motion.

For large skyrmions $R_\mathrm{S} \gg R_\mathrm{S}^*$, the energy of bound states can be directly calculated from the semiclassical picture. Along the skyrmion boundary there are chiral states inheriting the dispersion law of massless Dirac particles $\mathrm{E}_\varphi = \hbar v_\mathrm{F} k_\varphi$, and the Bohr-Sommerfeld quantization of their motion is respected;

$$2\pi R_\mathrm{S} k_\varphi + \varphi_\mathrm{B} = 2\pi m, \tag{2.7}$$

where $\varphi_\mathrm{B} = -\pi$ is the Berry phase for massless Dirac particles, which appears due to the rotation of the electron's spin when it makes a closed loop in momentum

space. This gives $\mathrm{E}_{\varphi} = \hbar v_{\mathrm{F}}(m + 1/2)/R_{\mathrm{S}}$ which is in excellent agreement with exact numerical calculation, as presented in Figure 2.1-c. It should be noted that the semiclassical arguments are also weakly dependent on the actual shape of the magnetic texture.

2.2.3 With Magnetic Field

Without the skyrmion texture, but in the presence of an external magnetic field, all surface states condensed into Landau levels (LL) indexed by main and orbital quantum numbers n and m, respectively. Landau levels have macroscopic degeneracy $m = [0, \Phi/\Phi_0 - 1]$, where Φ is the total flux through the TI surface and $\Phi_0 = hc/e$ is the flux quantum. In the radial gauge, LL are localized at a cyclotron radius $R_m \approx l_{\mathrm{B}}\sqrt{2(m+1)}$ with magnetic length $l_{\mathrm{B}} = \sqrt{\hbar c/eB}$. Their energy spectrum is given by

$$\begin{aligned} E^{\pm}_{nm} &= \pm v_{\mathrm{F}} \sqrt{\frac{2\hbar^2}{l_{\mathrm{B}}^2}|n| + \left(\frac{\Delta_{\mathrm{Z}}}{v_{\mathrm{F}}}\right)^2} \quad ; \; n \neq 0, \\ E_{0m} &= -sgn(B)\Delta_{\mathrm{Z}} \quad ; \; n = 0. \end{aligned} \tag{2.8}$$

The zeroth LL is spin polarized due to the orbital effect of magnetic field and its shift is sensitive to Zeeman coupling Δ_{Z}, while other LLs are not sensitive to the sign of Δ_{Z}.

In the presence of the magnetic field and the skyrmion texture, discrete states appear which are well split from the macroscopically degenerate $n = 0$ LL. For these states, the cyclotron radius R_m approximately coincides with the skyrmion radius R_{S}, therefore the states are localized at the skyrmion boundary and move with the skyrmion. The zeroth LL states with $R_m \gg R_{\mathrm{S}}$ approach

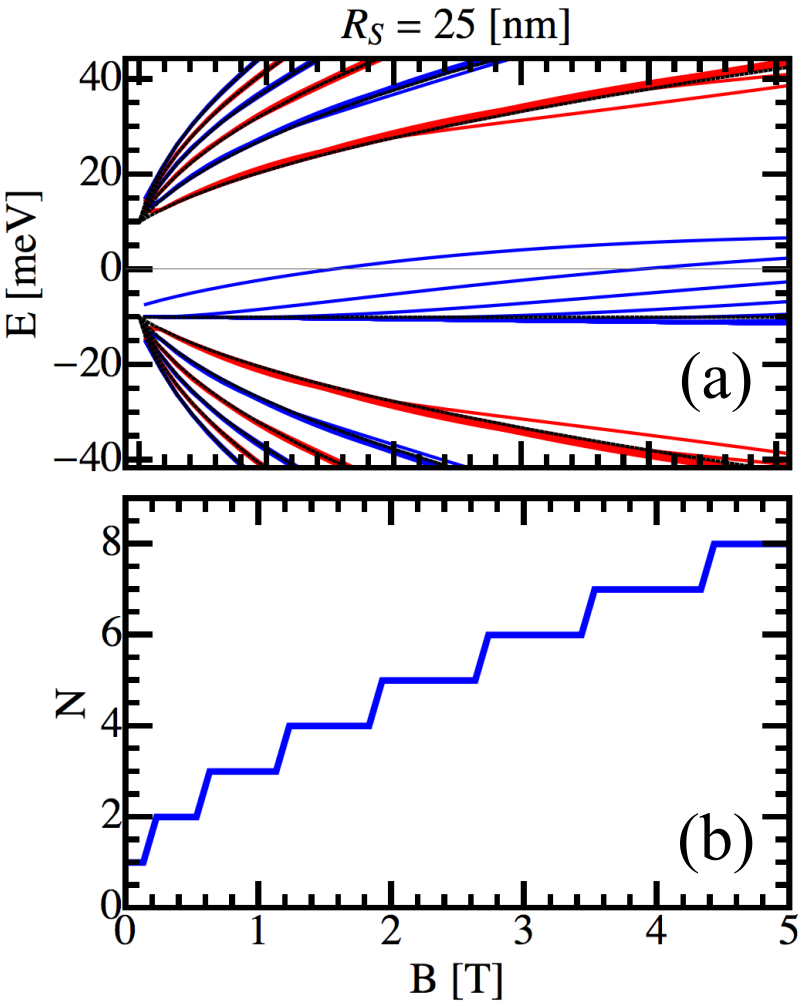

FIGURE 2.2: (a) Electronic spectrum of TI surface states a function of magnetic field B, for skyrmion radius $R_S = 25$ nm. Landau levels with $n \leq 6$ are presented. With increasing magnetic field the number of states split from the zeroth Landau level with the energy $E_{0m} = -\Delta_S - \Delta_Z$ increases. The black lines correspond to the spectrum without the texture. (b) Number of split states bound to the skyrmion as a function of magnetic field.

$E_{0m} = -\text{sgn}(B)(\Delta_Z + \Delta_S)$. These states are weakly affected by the skyrmion texture and are not correlated with its motion, in analogy to the delocalized states in the absence of a magnetic field. The energy spectrum of TI surface states as function of skyrmion radius is presented in Figure 2.1-b for magnetic field values

$B = 0.2$ T and 0.8 T. States bound to the skyrmion no longer appear in pairs since electron-hole symmetry is broken by the magnetic field. States with $|E| \geq \Delta_S$ condense into LLs with $n \neq 0$ which are weakly affected by the skyrmion texture.

Equations (2.4) and (2.5) can be solved exactly even in the presence of the external magnetic field. States localized at the skyrmion boundary have the wave functions

$$\Psi_m^- \propto \rho^m e^{-\frac{\rho^2 b}{2}} \begin{bmatrix} F_1(\alpha^-, m+1; \rho^2 b) \\ \rho F_1(\alpha^- + 1, m+2; \rho^2 b) \end{bmatrix} ; \Psi_m^+ \propto \rho^m e^{-\frac{\rho^2 b}{2}} \begin{bmatrix} \mathcal{U}(\alpha^+, m+1; \rho^2 b) \\ \rho \mathcal{U}(\alpha^+ + 1, m+1; \rho^2 b) \end{bmatrix}, \tag{2.9}$$

where F_1, $\mathcal{U}$ are confluent hypergeometric functions of the first and second kind, parameterized by $\alpha^\pm = ((n_z^\pm + \delta)^2 - \epsilon^2)/4b$.

The dependence of the TI surface spectrum as a function of magnetic field B for $R_S = 25$ nm is presented in Figure 2.2-a. The presence of states bound to the skyrmion is robust and occurs even in the presence of an external magnetic field. Moreover, due to the interplay between the LL and skyrmion confinement the number of bound states increases with magnetic field as presented in Figure 2.2-b. The appearance of bound states can lead to charging of the skyrmion texture. The electric charge is eN_B, where N_B is the number of additional occupied electronic states in comparison to the TI surface without the skyrmion texture. The value N_B depends on local chemical potential and can be controlled by magnetic field. Our mechanism of the texture charging differs from the one in Ref. [72] based on quantized response of electronic density to the emergent magnetic field $B_S(\mathbf{r})$. This type of charging also originates from a magnetic texture but is zero in our case because $B_S(\mathbf{r}) = 0$.

The radius of skyrmions in Cu_2OSeO_3, $R_S = 25$ nm, exceeds the critical radius $R_S^* = \hbar v_F / 2\Delta_S \approx 16$ nm and there is one bound state for magnetic field

0.05 T $\leq B \leq$ 0.2 T. The skyrmionic charge for Cu_2OSeO_3 specifically can be equal to the single charge of an electron. However, our model is applicable to other types of materials with skyrmions. The skyrmion charge becomes more tunable by magnetic field or doping if the radius of individual skyrmions is larger, the skyrmion phase is stabilized in a wider magnetic field interval, or for greater values of exchange coupling Δ_S. In these cases the skyrmion will host a few bound states.

2.3 Dynamics of Charged Skyrmions

We describe skyrmions with bound surface the following Lagrangian for a massive, charged particle with spin in an electromagnetic field

$$\mathcal{L} = Q_S \left[\dot{\mathbf{R}} \times \mathbf{R}\right]_z + eN_B \left(\varphi(\mathbf{R}) - \frac{\dot{R}}{c} A(\mathbf{R})\right) + \frac{m_S \dot{R}^2}{2}, \tag{2.10}$$

where $\mathbf{R}(t)$ is the skyrmion position. Here the first term represents the Magnus force originating from spin dynamics [73–75], and $Q_S = 4\pi\hbar\rho_S S N_S$ where N_S is the skyrmion topological invariant, with ρ_S and S the density and amplitude of spins in the skyrmionic magnet. The second term represents the interaction of skyrmion with external electromagnetic field, while the last term corresponds to the possible additional kinetic energy for a massive skyrmion with mass m_S, which could occur in a system with broken translational symmetry [76]. We find the skyrmion equations of motion from the Euler-Lagrange equations

$$\frac{\partial}{\partial t}\left(\frac{\partial \mathcal{L}}{\partial \dot{R}_i}\right) - \frac{\partial \mathcal{L}}{\partial R_i} = -\gamma \dot{R}_i. \tag{2.11}$$

Here γ is a phenomenological friction parameter. The mass term in (2.10) only provides the initial acceleration of the skyrmion. However the skyrmion's final steady velocity is determined from the balance between electric field and damping, thus it is independent of the mass m_{S} and we set $m_{\mathrm{S}} = 0$ in the following. In the presence of an electric field $\mathbf{E} = (E_x, 0)$ we find that the skyrmion acquires a steady-state velocity

$$\dot{R}_y = -\frac{eN_{\mathrm{B}}c\left(2Q_{\mathrm{S}}c + eN_{\mathrm{B}}B\right)}{\left(2Q_{\mathrm{S}}c + eN_{\mathrm{B}}B\right)^2 + c^2\gamma^2}E_x; \tag{2.12}$$

$$\dot{R}_x = -\frac{eN_{\mathrm{B}}c^2\gamma}{\left(2Q_{\mathrm{S}}c + eN_{\mathrm{B}}B\right)^2 + c^2\gamma^2}E_x. \tag{2.13}$$

In the limit $\gamma \to 0$, the system exhibits Hall motion where $\dot{R}_x = 0$ and $\dot{R}_y = -\mu_{\mathrm{S}}E_x$, defining skyrmion mobility $\mu_{\mathrm{S}} = eN_{\mathrm{B}}c/\left(2Q_{\mathrm{S}}c + eN_{\mathrm{B}}B\right)$. Taking $N_{\mathrm{B}} = 1$, $B = 0.2$ T, $\rho_{\mathrm{S}} \sim d/a^3$, where $d \approx 100$ nm is the magnetic film thickness and $a \sim 8.9$ Å is the crystallographic lattice constant, we have $\mu_{\mathrm{S}} \sim 1 \times 10^{-6}$ m^2/Vs. Electric fields as low as 10^2 V/m can induce drift velocities $v_{\mathrm{H}} \sim 0.1$ mm/s, comparable to skyrmions driven by conduction electrons in metallic systems [77] using the STT mechanism (Ref. [20, 21, 26, 78, 79] and references therein). In the system under consideration the skyrmionic material is insulating and the the surface spectrum of TI is gapped away from the skyrmion, which makes the STT mechanism unimportant.

2.4 Conclusions

It has recently been proposed that insulating skyrmions can be driven by a temperature gradient [24]. For electric fields $E \sim 10^5$ V/m or greater the velocity of a skyrmion driven by electric field is higher than the expected velocity

due to a thermal gradient (0.1 m/s in Ref. [24]) and, more importantly, an electric field is easier to manipulate than a temperature gradient. It has also been shown that in multiferroic materials, which include Cu_2OSeO_3, skyrmion textures have an intrinsic dipole moment which enables them to couple to to the gradient of electric field [23, 67, 68, 80]. Regardless of the difficulty of applying a gradient in electric field, the estimated Hall velocity v_{H} in our approach is two orders of magnitude greater than v_{H} due to magnetoelectric coupling [23], where $v_{\mathrm{H}} \approx (\lambda R_{\mathrm{S}}/2\pi S\hbar)\Delta \mathrm{E} \sim 10^{-3}$ mm/s with $R_{\mathrm{S}} = 25$ nm, dipolar coupling $\lambda \sim 10^{-33} \approx \mathrm{C} \cdot \mathrm{m}$ [66], and field strength *difference* $\Delta \mathrm{E} \sim 10^2$ V/m. We therefore conclude that our mechanism is comparatively very effective due to the direct coupling of skyrmions with electric field.

In an experiment one can use a TI such as Bi_2Se_3 as a substrate and epitaxially grow the Cu_2OSeO_3 thin film on top of it. An ultra-thin buffer layer inserted between these two can help to avoid lattice mismatch while keeping the coupling between Dirac electrons and the magnetization. Concerning the experimental difficulty in growing Cu_2OSeO_3 films, one can also use monolayers of ferromagnet instead, which is generally insulating. The interfacial DM interaction can also generate skyrmions therein [81]. The whole sample is sandwiched in a pair of electrodes, which generates an electric field.

It should be noted that the skyrmion phase can be intrinsic to the surface states of a 3D TI in the presence of strong Coulomb repulsion and hexagonal warping, which takes place at high doping [82]. In that regime our mechanism is not of importance, since the skyrmion texture changes the surface spectrum in the vicinity of the Dirac point which is deeply buried under the Fermi level.

We have focused on the behavior of a single charged skyrmion. Skyrmions most frequently appear in a lattice which can be pinned by disorder and the underlying atomic lattice. Therefore in an experiment this effect would manifest as

a rotation of the skyrmion lattice caused by Hall motion of individual charged skyrmions. We predict that the angle of skyrmion lattice rotation will be proportional to the electric field and the number of bound states at the skyrmion radius. The angle of rotation should change within the skyrmion phase in response to increased DC electric field. To rule out magnetoelectric effects, an experiment at constant electric field but varying magnetic field could be conducted, provided that the stabilizing magnetic field range of skyrmions is big enough to tune the number of bound states. In this case we predict a change in rotation angle in response to an increase in magnetic field, indicating additional bound surface states.

In conclusion, we have shown that skyrmions on a 3D TI surface can be come charged. The charging is due to magnetic confinement of the TI surface states via proximity coupling to a magnetic thin film. Importantly, the bound states are robust in the presence of an external magnetic field and are expected to contributed to electric field driven skyrmion motion. Our findings point toward a new way to manipulate skyrmions and skyrmion crystals in helical magnets.

Chapter 3: Transport of Dirac Electrons coupled to Magnetic Vortices

3.1 Overview

The purpose of this Chapter is to show how signatures of an effective gauge field, created by magnetic vortices, can be observed in transport of Dirac fermions. Coupling the Dirac states to a magnetic system with in-plane magnetic moments that undergoes a phase transition, like the 2D XY model, allows for a system with tunable gauge disorder. In Section 3.2 we present the model and discuss the mapping of classical magnetic fluctuations to static random magnetic field (RMF) disorder. In Section 3.3 we discuss the range of applicability of the perturbative treatment of the disorder by calculating the self energy of Dirac fermions and discussing the renormalization of the single-particle energy spectrum. In Section 3.4 we calculate the temperature behavior of resistivity in the regime where perturbation theory is valid. Section 3.5 contains our conclusions and expanded discussion of the limits of using Dirac materials, topological insulators in particular, to explore models of free Dirac fermions common in high-energy physics.

3.2 Model

The Dirac surface states of a 3D TI coupled to the XY-model can be described by the following Euclidean action

$$S = S_{\mathrm{XY}} + S_{\mathrm{TI}} + S_{\mathrm{int}}, \tag{3.1}$$

where

$$\begin{aligned} S_{\mathrm{XY}} &= \frac{\rho_{\mathrm{s}}}{2T}\int d\mathbf{r}\ (\nabla\theta)^2; \quad S_{\mathrm{int}} = \Delta\int_0^\beta d\tau d\mathbf{r}\ \psi^\dagger \mathbf{n}(\mathbf{r})\cdot\boldsymbol{\sigma}\psi; \\ S_{\mathrm{TI}} &= \int_0^\beta d\tau d\mathbf{r}\ \psi^\dagger\left\{\partial_\tau + v_{\mathrm{F}}\left[\mathbf{p}\times\boldsymbol{\sigma}\right]_z + \alpha p^2 - \mu\right\}\psi. \end{aligned} \tag{3.2}$$

The surface states are represented by a two-component spinor $\psi = (\psi_\uparrow, \psi_\downarrow)^T$, $\boldsymbol{\sigma} = (\sigma^x, \sigma^y)$ is the vector of Pauli matrices representing the real electron spin, v_{F} is the Fermi velocity, and $\Delta > 0$ is the interlayer coupling between surface states and a magnetic XY-model with magnetic moments $\mathbf{n}(\mathbf{r}) = (\cos\Theta(\mathbf{r}), \sin\Theta(\mathbf{r}))$ with $\Theta(\mathbf{r})$ describing their direction, as previously studied in Section 1.1.2 and Section 1.2.2. The strength of quadratic band curvature, occurring in many real topological insulators, is parameterized by α.

If quadratic band curvature caused by electron-hole asymmetry is neglected ($\alpha = 0$), the magnetization plays the role of an emergent gauge field $\mathbf{a} = \Delta v_{\mathrm{F}}^{-1}\ [\mathbf{n}\times\hat{z}]$. It can be split into transverse and longitudinal parts $\mathbf{a} = \mathbf{a}^{\mathrm{l}} + \mathbf{a}^{\mathrm{t}}$. The transverse part is responsible for the emergent magnetic field $B_z = [\nabla\times\mathbf{a}^{\mathrm{t}}]_z = \Delta v_{\mathrm{F}}^{-1}(\nabla\mathbf{n}^{\mathrm{l}})$ perpendicular to the surface, and the longitudinal part can generate an emergent electric field $\mathbf{E} = -\partial_t\mathbf{a}^{\mathrm{l}} = -\Delta v^{-1}\partial_t\mathbf{n}^{\mathrm{t}}$. Here $\mathbf{n}^{\mathrm{l}}$ and $\mathbf{n}^{\mathrm{t}}$ are the corresponding longitudinal and transverse components of spin density. Magnetic fluctuations are assumed to be classical and therefore static in time. This leads to zero emergent

electric field, and therefore the longitudinal gauge field can be safely gauged away as was done for the skyrmion texture in Chapter 2.

Excitations of the magnetic XY-model are spin-waves and vortices $\Theta(\mathbf{r}) = \Theta_{\rm sw}(\mathbf{r}) + \Theta_{\rm v}(\mathbf{r})$. Spin-waves $\Theta_{\rm sw}(\mathbf{r})$ create a smooth emergent magnetic field B_z, and vortices $\Theta_{\rm v}(\mathbf{r})$ generate a nonuniform magnetic field in a very nonlocal way. For a set of vortices situated at $\mathbf{r}_i$, the distribution of phase is $\Theta_{\rm v}(z) = \sum_i q_i \arg(z - z_i)$ with $z = x + \mathbf{i}y$ and $q_i = \pm$ for vortices and antivortices. The resulting random magnetic field (RMF) seen by the Dirac fermions is

$$B_{\rm z}^{\rm RMF} = \frac{\Delta}{v_{\rm F}} \left[\cos\Theta \frac{\partial \Theta_{\rm sw}}{\partial y} - \sin\Theta \frac{\partial \Theta_{\rm sw}}{\partial x} + \sum_i \frac{q_i \cos(\Theta_i)}{|\mathbf{r} - \mathbf{r_i}|} \right] \tag{3.3}$$

with $\Theta_i = \Theta_{\rm sw}(\mathbf{r}) + \sum_{j \neq i} q_j \arg[z - z_j]$. It diverges in the vicinity of each vortex core and its magnitude depends nonlocally on the position of all other vortices and slowly decays away from the vortex cores.

The reconstruction of the local electronic structure due to the nonuniform spin density $\mathbf{n}(\mathbf{r})$ near the vortex core can be probed by tunneling experiments, as considered in detail in the case of magnetic impurities [83, 84]. Here, we are interested in transport of Dirac fermions due to scattering at magnetic fluctuations where the chemical potential lies far above the Dirac point. In this case, scattering is restricted to the conduction band, and the vortex contribution to the effective magnetic field leads to an effective RMF as the conduction electrons see many vortices.

The interaction between Dirac fermions mediated by longitudinal spin fluctuations is obtained by integrating out the spin fluctuations and expanding to the second order in Δ/μ. The magnetic fluctuations are assumed to be static, therefore the partition function of the entire system is separable into the partition function for Dirac fermions (including the interaction), and the classical action for

the XY-magnet

$$\mathcal{Z} = \int \mathrm{D}\mathbf{n} \int \mathrm{D}\psi^\dagger \mathrm{D}\psi e^{-S_D - S_{\mathrm{XY}}} \approx \mathcal{Z}_D \mathcal{Z}_{\mathrm{XY}}.$$

This gives

$$S_{\mathrm{D}} = S_{\mathrm{TI}} + S_{\mathrm{int}} = \int_0^\beta d\tau \int d\mathbf{r}\, \psi^\dagger(\mathbf{r},\tau) \left[\partial_\tau + v_{\mathrm{F}} \mathbf{p} \times \boldsymbol{\sigma} + \alpha p^2 - \mu + \mathbf{n}(\mathbf{r}) \cdot \boldsymbol{\sigma}\right] \psi(\mathbf{r},\tau) \tag{3.4}$$

The interaction term is not quadratic in the magnetic moments $\mathbf{n}$, so we cannot perform a Gaussian integration over the $\mathbf{n}$ variables to find the effective action. Instead, we treat the interaction part of the action perturbatively. Expanding in S_{int} and averaging over S_{XY}, we have

$$\begin{aligned} e^{-S_{\mathrm{int}}} \approx 1 - \Delta \int_0^\beta d\tau \int d\mathbf{r}\ \psi^\dagger \sigma^\alpha \psi \left\langle n^{\mathrm{l}}_\alpha(\mathbf{r}) \right\rangle + \\ + \frac{\Delta^2}{2} \int_0^\beta d\tau_1 d\tau_2 \int d\mathbf{r}_1 d\mathbf{r}_2 \psi_1^\dagger \sigma^\alpha \psi_1 \left\langle n^{\mathrm{l}}_\alpha(\mathbf{r}_1) n^{\mathrm{l}}_\beta(\mathbf{r}_2) \right\rangle \psi_2^\dagger \sigma^\beta \psi_2 \end{aligned}$$

For the XY model in 2D, we know that $\left\langle \mathbf{n}^{\mathrm{l}}(\mathbf{r}) \right\rangle \sim 0$, so we are left with the second order term giving $e^{-\tilde{S}_{\mathrm{int}}}$, corresponding to a disordered static magnetic field which reads

$$\tilde{S}_{\mathrm{int}} = -\frac{\Delta^2}{2} \int d\tau_1 d\tau_2 d\mathbf{r}_1 d\mathbf{r}_2 W_1^\alpha \left\langle n^{\mathrm{l}}_\alpha(\mathbf{r}_1) n^{\mathrm{l}}_\beta(\mathbf{r}_2) \right\rangle W_2^\beta, \tag{3.5}$$

where $W_i^\alpha = \psi^\dagger(\mathbf{r}_i,\tau_i)\sigma^\alpha\psi(\mathbf{r}_i,\tau_i)$, and $\langle \cdots \rangle$ denotes averaging over the free XY action including spin waves and vortices. The longitudinal part of the spin-spin correlation function is the only relevant one, given by

$$\left\langle n^{\mathrm{l}}_\alpha(\mathbf{r}_1) n^{\mathrm{l}}_\beta(\mathbf{r}_2) \right\rangle = \frac{1}{2} \left(\frac{|\mathbf{r}_1 - \mathbf{r}_2|}{2a} \right)^{-\eta} \exp\left(-\frac{r}{\xi_+} \right) \Lambda^{\alpha\beta}_{\mathbf{r}_1 - \mathbf{r}_2}, \tag{3.6}$$

where the matrix $\Lambda^{\alpha\beta}_{\mathbf{q}=q_\alpha q_\beta/q^2}$ ensures that only longitudinal spin fluctuations are taken into account and a is the attice cutoff for the magnet. Interaction between Dirac fermions $V_0^{\alpha\beta}(\mathbf{q}) = -\Delta^2\langle n^{\mathrm{l}}_\alpha(\mathbf{q}) n^{\mathrm{l}}_\beta(-\mathbf{q})\rangle = V_0(\mathbf{q})\Lambda_{\alpha\beta}$ is connected with the gauge invariant correlator of the emergent magnetic field

$$V_0(\mathbf{q}) = -\frac{v_{\mathrm{F}}^2\langle B_z(-\mathbf{q}) B_z(\mathbf{q})\rangle}{q^2}$$

and is given by

$$V_0(\mathbf{q}) = -\frac{\pi\eta\Delta^2\xi_+^{2-\eta}a^\eta}{(q^2\xi_+^2+1)^{1-\eta/2}}, \tag{3.7}$$

found by taking the Fourier transform of Equation (3.6). For $T < T_{\mathrm{BKT}}$, $\xi_+ \to \infty$ and the propagator is $V_0(\mathbf{q}) \propto 1/q^{2-\eta}$, which results in singular behavior as $\mathbf{q} \to 0$ and strong temperature dependence through $\eta(T)$. In 2D this leads to an infrared divergence in the self-energy which cannot be treated in a controlled manner in the absence of screening [85]. Particularly, in the random phase approximation (RPA) the screened interaction is given by

$$V^{-1}(q) = V_0^{-1} - \Pi^{\mathrm{l}}(q). \tag{3.8}$$

Here $\Pi^{\mathrm{l}}(q)$ is the longitudinal spin-spin response function in the static limit which is given by [85]

$$\Pi^{\mathrm{l}} = \frac{q}{8\pi v_{\mathrm{F}}}\mathrm{Re}\left[\frac{2k_{\mathrm{F}}}{q}\sqrt{1-\left(\frac{2k_{\mathrm{F}}}{q}\right)^2} + \arcsin\left(\frac{2k_{\mathrm{F}}}{q}\right) - \frac{\pi}{2}\right]. \tag{3.9}$$

It is zero for $q \leq 2k_{\mathrm{F}}$, which signals the absence of screening. Physically, vanishing $\Pi^{\mathrm{l}}(0)$ implies the absence of uniform spin polarization in the TI in the presence of a uniform external spin density $\mathbf{n}$. Really, $\mathbf{n}$ can be safely gauged away through a transformation which shifts the position of a Dirac point $\mathbf{q}_{\mathrm{D}} = \Delta v_{\mathrm{F}}^{-1}[\mathbf{n}\times\mathbf{e}_z]$, and

therefore does not lead to any response.

Above we have neglected electron-hole asymmetry ($\alpha = 0$) in the Hamiltonian, describing electrons at the surface of the topological insulator. In Bismuth based topological insulators it is not negligible, but usually does not change the physics qualitatively (see [82, 86] for an exception). Here we point out that the presence of electron-hole asymmetry or warping is crucial since it breaks the connection to the emergent gauge field picture. As a result, the spin-spin response function at low momenta becomes finite and allows screening. Recalling that $\Pi^{\mathrm{l}}(0)$ is the response to the uniform spin density, corresponding to momentum shift of Dirac states $\mathbf{q}_{\mathrm{D}} = \Delta v_{\mathrm{F}}^{-1}[\mathbf{n} \times \mathbf{e}_z]$, the resulting average spin polarization of electrons $\mathbf{s}_{\mathrm{D}} = \langle \psi^\dagger \boldsymbol{\sigma} \psi \rangle$ is given by

$$\mathbf{s}_{\mathrm{D}} = \sum_{\mathbf{p}} \left[\mathbf{e}_{\mathrm{z}} \times \frac{\mathbf{p} - \mathbf{q}_{\mathrm{D}}}{2|\mathbf{p} - \mathbf{q}_{\mathrm{D}}|} \right] n_{\mathrm{F}}(\alpha p^2 + v_{\mathrm{F}}|\mathbf{p} - \mathbf{q}_{\mathrm{D}}| - \mu), \tag{3.10}$$

where $n_{\mathrm{F}}(\epsilon_p)$ is the Fermi step-like distribution at zero temperature. To linear order in $\mathbf{n}$ and α we get $\mathbf{s}_{\mathrm{D}} = -\bar{\alpha}\mathbf{n}\nu_{\mathrm{F}}\Delta/2$ with $\nu_{\mathrm{F}} = \mu/2\pi\hbar^2 v_{\mathrm{F}}^2$ the density of states of Dirac electrons at the Fermi level and $\bar{\alpha} = \alpha\mu/v_{\mathrm{F}}^2$ the dimensionless electron-hole asymmetry strength, which leads to $\Pi^{\mathrm{l}}(0) = -\bar{\alpha}\nu_{\mathrm{F}}\Delta/2$. The spin polarization vanishes in the absence of electron-hole asymmetry as expected. The screened interaction in the presence of electron-hole asymmetry now allows us to develop a theory of electron transport using usual perturbative techniques. the screened propagator in RPA mediated by magnetic fluctuations at $T < T_{\mathrm{BKT}}$ is then given by

$$V(\mathbf{q}) = -\frac{\pi\eta\Delta^2\xi_\alpha^{2-\eta}a^\eta}{(q\xi_\alpha)^{2-\eta}+1} \;\; ; \;\; \xi_\alpha = \left(\frac{2}{\bar{\alpha}\nu_{\mathrm{F}}\Delta\pi\eta a^\eta} \right)^{\frac{1}{2-\eta}}. \tag{3.11}$$

The strength of electron-hole asymmetry, which regularizes our theory, can be characterized by the dimensionless parameter $\bar{\alpha}$ which decreases with the chemical potential μ and vanishes in the undoped regime. As a result, by controlling the doping level the system can be tuned from the perturbative to non-perturbative regime. To clarify the range of applicability of the perturbative approach, we consider the renormalization of the single-particle spectrum.

3.3 Self Energy of Dirac Electrons

In the Born approximation, the self energy of Dirac electrons is

$$\Sigma^{\mathrm{R}}(\omega, p) = \int_q \mathcal{Q}^{\alpha}_{\mathbf{p},\mathbf{p}-\mathbf{q}} V^{\alpha\beta}(\mathbf{q}) \mathcal{Q}^{\beta}_{\mathbf{p}-\mathbf{q},\mathbf{p}} G^{\mathrm{R}}_0(\omega, \mathbf{p}-\mathbf{q}), \tag{3.12}$$

where $\mathcal{Q}_{\mathbf{p},\mathbf{p}'} = \langle p|\boldsymbol{\sigma}|p'\rangle = (-\sin\left[(\varphi_{\mathbf{p}} + \varphi_{\mathbf{p}'})/2\right],\ \cos\left[(\varphi_{\mathbf{p}} + \varphi_{\mathbf{p}'})/2\right])^T$ is the matrix element for scattering of electrons from the conduction band and their Green's function is $G^{\mathrm{R}}_0 = (\omega - v_{\mathrm{F}}p + \mu + \mathbf{i}\delta)^{-1}$. Summation over $\alpha, \beta = x, y$ in Equation (3.12) gives the angle factor $\bar{\mathcal{Q}}_{\mathbf{p},\mathbf{p}-\mathbf{q}} = \mathcal{Q}^{\alpha}_{\mathbf{p},\mathbf{p}-\mathbf{q}} \Lambda^{\alpha\beta}_{\mathbf{q}} \mathcal{Q}^{\beta}_{\mathbf{p}-\mathbf{q},\mathbf{p}}$ as follows

$$\bar{\mathcal{Q}}_{\mathbf{p},\mathbf{p}-\mathbf{q}} = \sin^2\left(\frac{2\varphi_{\mathbf{q}} - \varphi_{\mathbf{p}} - \varphi_{\mathbf{p}-\mathbf{q}}}{2}\right), \tag{3.13}$$

where $\varphi_{\mathbf{p}}$ denotes the polar vector of a fermion with momentum $\mathbf{p}$. If the scattering is elastic $|\mathbf{p}| = |\mathbf{p}-\mathbf{q}|$, trigonometry dictates $2\varphi_{\mathbf{q}} - \varphi_{\mathbf{p}} - \varphi_{\mathbf{p}-\mathbf{q}} = \pi$ and $\bar{\mathcal{Q}}_{\mathbf{p},\mathbf{p}-\mathbf{q}} = 1$. $\Re\Sigma(0, p_{\mathrm{F}})$ at the Fermi level leads to Fermi energy renormalization, and it is zero for this case. Inserting the screened propagator, Equation (3.11), into Equation (3.12) gives a single particle decay rate $\hbar\gamma^* = -\Im\hat{\Sigma}(0, p_{\mathrm{F}})$, where

$$\Im\hat{\Sigma} = -\frac{\Delta^2 \eta \xi_{\alpha}^{1-\eta} a^{\eta}}{2\pi\hbar v_{\mathrm{F}}} \Gamma\left(\frac{3-\eta}{2-\eta}\right) \Gamma\left(\frac{\eta-1}{\eta-2}\right). \tag{3.14}$$

The product of gamma functions is of order 1 for $0 < \eta < 1/4$.

The single particle life time diverges in the absence of screening, where $\xi_\alpha \to \infty$ for $\bar{\alpha} \to 0$, as expected. It cannot be cured by using the self-consistent Born approximation and signals the break down of the perturbative approach, which we use below for a calculation of conductivity of Dirac fermions. The apparent breakdown of perturbation theory in this model could also signal the existence of a non-Fermi liquid state on the TI surface, a possibility which could be explored by including the dynamics of the BKT magnet, which is beyond the scope of this work.

In the presence of screening, the Fermi-liquid approach breaks down for $\hbar\gamma^* \gtrsim \mu$. Using Equation (3.11) and Equation (3.14) we find a lower bound on the Fermi energy

$$\mu_c^{4-3\eta} \simeq \frac{\Delta^3 \eta v^2}{\pi^2 \alpha} \left(\frac{2\Delta \hbar v^3}{\pi \alpha a} \right)^{-\eta}. \tag{3.15}$$

For $\mu < \mu_c$ this approach is no longer valid and the system could be tuned from the perturbative to nonperturbative regime by doping. We estimate for Bi_2Te_3, $v_F = 0.5 \times 10^6$ m/s, $\Delta = 10$ meV and $\alpha = 1/2m^*$ with $m^* \sim 0.1 m_e$. The short distance cutoff a is estimated by the half the lattice constant of two dimensional BKT magnet K_2CuF_4, where $a \sim 2.5$ Å [33]. At $T = T_{\mathrm{BKT}}$, $\eta_{\mathrm{BKT}} = 1/4$ which gives $\mu_c \gtrsim 6$ meV. However, it is also important to keep in mind that for $\mu \lesssim \Delta$ higher order terms in Equation (3.5) become important and are not considered here. We leave the non-perturbative regime to further investigations which could be informed by this type of experiment.

3.4 Transport of Dirac Electrons

In the doped regime at $\mu \gg \hbar\gamma^*$, the quasipartcle picture is well defined and the resistivity of Dirac fermions can be approximated by the Drude formula

$$\rho = \frac{h}{e^2}\frac{2\hbar}{\mu\tau_{\rm tr}}, \tag{3.16}$$

where $\tau_{\rm tr}$ is the transport scattering time. Different scattering mechanisms, including impurities, phonons, and spin-fluctuations, additively contribute to $\tau_{\rm tr}^{-1}$ and can be easily separated. Here we concentrate on elastic scattering due to magnetic fluctuations, where for $|q| = 2k_{\rm F}\sin\varphi/2$ the corresponding contribution is given by

$$\begin{aligned}\frac{1}{\tau_{\rm tr}} &= \frac{2\pi}{\hbar}\int_q \bar{\mathcal{Q}}_{\mathbf{p},\mathbf{p}-\mathbf{q}}\,|V_{\mathbf{q}}|\,(1-\cos\varphi_q)\,\delta(\xi_{\mathbf{p}-\mathbf{q}}-\xi_{\mathbf{p}}) \\ &= \frac{\pi\eta\Delta^2}{4\hbar\mu}\left(\frac{\mu}{\mu_a}\right)^{\eta}\int\frac{d\varphi}{\pi}\frac{(2k_{\rm F}\xi_+)^{2-\eta}\sin^2(\frac{\varphi}{2})}{\left[(2k_{\rm F}\xi_+\sin(\frac{\varphi}{2}))^2+1\right]^{\frac{2-\eta}{2}}},\end{aligned} \tag{3.17}$$

with $\mu_a = \hbar v_{\rm F}/2a$. In contrast to the single particle decay rate γ^*, the inverse transport time $\tau_{\rm tr}^{-1}$ does not diverge in the absence of screening and weakly depends on screening length ξ_α. Therefore, in Equation (3.17) we used the unscreened propagator $V_0(\mathbf{q})$ given by Equation (3.7). Nevertheless, we need to keep in mind that the derivation of the Drude formula implies $\hbar\gamma^* \ll \mu$ since all diagrams with crossed impurity lines, which are important in the opposite regime, are neglected [87]. Using Equation (3.16) and the results above, the resistivity has the form

$$\frac{\rho(T,\mu)}{\rho_{\rm BKT}} = \frac{\eta}{I_0\eta_{\rm BKT}}\left(\frac{\mu}{\mu_a}\right)^{\eta-\eta_{\rm BKT}}\mathcal{I}(\eta). \tag{3.18}$$

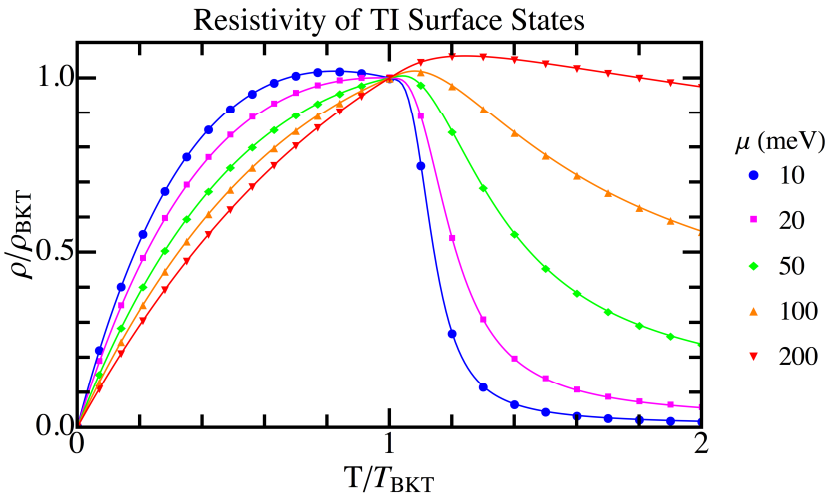

FIGURE 3.1: Resistivity of TI surface states coupled to an XY model. The resistivity scales linearly with temperature as $T \to 0$ and across the BKT transition, with a nonuniversal peak at $T \sim T_{\mathrm{BKT}}$ that increases with increasing chemical potential μ. As μ increases the effect of the transition is less pronounced.

Where $\mathcal{I}(\eta)$ is the integral in Equation (3.17), $\eta_{\mathrm{BKT}} = 1/4$, and $I_0 = \mathcal{I}(\eta_{\mathrm{BKT}}) \approx 1.72$. The resistivity at the transition is given by

$$\rho_{\mathrm{BKT}} = \frac{h}{e^2} \frac{\sqrt{\pi}\Delta^2}{4\ \mu^2} \left(\frac{\mu}{\mu_a}\right)^{\frac{1}{4}} \frac{\Gamma(5/8)}{\Gamma(9/8)}. \tag{3.19}$$

$\rho(T,\mu)/\rho_{\mathrm{BKT}}$ is shown in Figure 3.1 for different values of μ. There is a clear peak near T_{BKT} due to increased magnetic fluctuations. As $T \to 0$ we find the following expression

$$\frac{\rho(T \to 0)}{\rho_{\mathrm{BKT}}} = \frac{\sqrt{\pi}\ \Gamma(9/8)}{\Gamma(5/8)} \left(\frac{\mu}{\mu_a}\right)^{-\frac{1}{4}} \frac{T}{T_{\mathrm{BKT}}}, \tag{3.20}$$

where the resistivity is linear at low temperature, unlike usual impurity scattering. As $T \to T_{BKT}^{\pm}$ across the transition, we find that

$$\frac{\rho(T \to T_{\mathrm{BKT}}^{+})}{\rho_{\mathrm{BKT}}} = 1 + \frac{1}{4}\left\{4 + \ln\left(\frac{\mu}{\mu_a}\right)\right\}\frac{\Delta T}{T_{\mathrm{BKT}}}, \tag{3.21}$$

$$\frac{\rho(T \to T_{\mathrm{BKT}}^{-})}{\rho_{\mathrm{BKT}}} = 1 + \frac{1}{8}\left\{8 + 2\ln\left(\frac{\mu}{\mu_a}\right) + \psi\left(\frac{5}{8}\right) - \psi\left(\frac{9}{8}\right)\right\}\frac{\Delta T}{T_{\mathrm{BKT}}}, \tag{3.22}$$

where $\Delta T = T - T_{\mathrm{BKT}}$ and ψ is the digamma function. The resistivity is linear in temperature in all three regimes but has a different slope in each case. As $T \to 0$, the dynamics of the magnetic moments becomes important, necessitating a fully quantum theory which is not considered here. The slope is dictated by μ and changes significantly with doping as shown in Figure 3.1. The temperature of maximal resistivity is also dictated by μ; it occurs for $T \sim T_{\mathrm{BKT}}$ but is nonuniversal. It can be solved for using the exact expression in Equation (3.18). We note that for $\mu < 13$ meV the slope is always negative for $T > T_{\mathrm{BKT}}$ and the maximum resistivity occurs before the transition.

In a real experiment there will be many sources of scattering including phonons and non-magnetic impurities. The linear temperature dependence and sharp peak near the BKT transition enables the separation of this scattering mechanism from others in the system. Scattering due to impurities is temperature independent, while at low temperatures phonon scattering leads to a different scaling law.

3.5 Conclusions

Physical realization of Dirac fermion-gauge field models in TI systems relies heavily on the strength of magnetic perturbations to the TI system. In this Section we provide some conclusions and estimations of the coupling strength Δ and how it connects to current experiments. For the 3D TI Bi_2Te_3 we use $\mu = 0.1$ eV. The

transport lifetime in Bi_2Te_3 can be inferred from transport measurements to be $\tau_0 \sim 10^{-12}$ s [88].

In order to observe the anomalous transport behavior described above, the coupling between the magnetic layer and the TI must be strong enough such that $\tau_{tr} \lesssim \tau_0$. The transport time τ_{tr} at $T = T_{\mathrm{BKT}}$ is found from Equation (3.17), where

$$\tau_{tr}^{-1} = \frac{\pi\Delta^2}{16\hbar\mu}\left(\frac{\mu}{\mu_a}\right)^{\frac{1}{4}} I_0. \tag{3.23}$$

Setting $\tau_{tr} = \tau_0$ gives a lower bound on the coupling strength Δ. For our parameters, we find $\Delta \gtrsim 10$ meV, which is well within the range of the recently observed $\Delta \sim 85$ meV in lanthanide-doped Bi_2Te_3 [89].

We have considered the transport of Dirac fermions coupled to an XY-model as temperature is tuned through the BKT transition. We claim that both short-range and quasi long-range disorder can be realized, and the transition between these regimes can be tuned by both doping level and temperature, thus determining the strength and nature of the disorder. We have analyzed the resistivity at high doping and we find that it scales linearly with temperature, with a prominent peak at the BKT transition temperature where magnetic fluctuations are the strongest. Notably, the resistivity also scales linearly with temperature as $T \to 0$. The effect is strengthened by decreasing the Fermi energy.

Chapter 4: Dissipative Dynamics of Solitons in Bose-Einstein Condensates

4.1 Overview

In the theoretical literature, dissipation in solitonic systems has been studied by including a trap or introducing additional dimensions [90–93]. In higher dimensions, solitons are unstable and experimental systems must be close to one-dimensional (1D) in order to observe them. The friction coefficient of the soliton is related to the reflection coefficient of excitations scattering off of it [54, 90, 94, 95]. In isolated Bose gases at non-zero temperature, these scatterers would be the Bogoliubov quasiparticles of the original condensate, and their reflection coefficient can be calculated for various geometries. However, in a 1D scattering theory and without a trap the Bogoliubov excitations are reflectionless, and therefore do not cause Ohmic friction [54, 96]. It was recently shown that non-Ohmic friction can still occur in these systems by accounting for non-Markovian effects [96]. However, experimental systems are necessarily quasi-1D, therefore both Ohmic friction and non-Markovian friction are present.

In this Chapter we consider an alternative way to induce Ohmic friction in a 1D system consisting of a condensate, with a dark soliton, coupled to a non-interacting thermal cloud of "impurity" atoms. We consider fermionic impurities except for Section 4.7 where we consider bosonic impurities as related to Ref. [63]. We present three main results: First, the system *with* impurities can be tuned

to have zero Ohmic friction, based only on the ratio of interspecies (impurity-condensate) to intraspecies (condensate-condensate) interaction strengths. Secondly, in contrast to objects with positive mass, for a negative mass object such as a dark soliton there is no diffusion in a meaningful sense in free space. We show that the soliton undergoes only ballistic motion due to the fact that friction increases its speed, providing an anti-damping force. Third, in the presence of Ohmic friction *and* an external potential, the dark soliton can undergo diffusion or Brownian motion, characterized by a mean squared displacement that grows linearly in time, $\langle \bar{x}^2 \rangle \propto Dt$. In this case, the diffusion coefficient is $D \propto \gamma/\omega^2$, where γ is the friction coefficient and ω is the frequency of harmonic confinement. The diffusion coefficient is *proportional* to the amount of friction in the system, in contrast to the usual case where $D \propto 1/\gamma$ [97]. Dark solitons provide an ideal experimental testbed for the mechanism of trap-induced Brownian motion.

This Chapter is structured as follows: In Section 4.2 we outline the model of a dark soliton in quasi-1D BEC in the presence of non-interacting fermions. In Section 4.3 we discuss the single-particle scattering properties of the fermions in the presence of the soliton, which acts as a potential well for the fermions. Section 4.4 is devoted to kinetic theory, where we derive two essential equations: the microscopic expression for the friction coefficient, and the kinetic equation for the soliton probability distribution function (PDF). We show how the full time-dependent PDF can be calculated exactly using the method of characteristics. In Section 4.5, we use the PDF to find the soliton's average position and variance in position. We show that Brownian motion only occurs in the presence of an external trap and calculate the diffusion coefficient. We use the PDF again in Section 4.6 to define and calculate the soliton lifetime. In Section 4.7 we discuss the experimental implementation of Ref. [63] and the difference in the theory used

for that work. Finally, in Section 4.8 we conclude and discuss alternative experimental implementations of this theory. With the exception of Section 4.7, this chapter was previously published in Physical Review A, © American Physical Society, 2017. Section 4.7 was published in Proceedings of the National Academies of Sciences (PNAS), © PNAS, 2017.

4.2 Model

We consider a quasi-1D bosonic superfluid interacting with a Fermi gas in an external potential. The proposed creation and manipulation of solitons requires a highly elongated geometry with confinement frequency $\omega_{\mathrm{c/i},x} \ll \omega_{\mathrm{c/i}\perp}$, where the subscript c denotes the bosons that make up the condensate, subscript i denotes impurity atoms, and $\omega_{\mathrm{c/i},x}$ and $\omega_{\mathrm{c/i}\perp}$ denote the confinement frequencies for the elongated and transverse directions, respectively.

A 1D theory is sufficient to describe the quasi-1D system provided that the transverse confinement is tight enough that transverse degrees of freedom can be eliminated, conditions which we enumerate below. Under these conditions, the system is described by the 1D Hamiltonian $\hat{H} = \hat{H}_{\mathrm{c}} + \hat{H}_{\mathrm{i}} + \hat{H}_{\mathrm{int}}$,

$$\hat{H}_{\mathrm{c}} = \int dx\ \frac{\hbar^2}{2m_{\mathrm{c}}}\nabla\hat{\varphi}^\dagger\nabla\hat{\varphi} + U(x)\hat{\varphi}^\dagger\hat{\varphi} + \frac{g}{2}\hat{\varphi}^\dagger\hat{\varphi}^\dagger\hat{\varphi}\hat{\varphi} \tag{4.1}$$

$$\hat{H}_{\mathrm{i}} = \int dx\ \frac{\hbar^2}{2m_{\mathrm{i}}}\nabla\hat{\psi}^\dagger\nabla\hat{\psi} + U(x)\hat{\psi}^\dagger\hat{\psi} \tag{4.2}$$

$$\hat{H}_{\mathrm{int}} = \int dx\ g'\hat{\psi}^\dagger\hat{\varphi}^\dagger\hat{\varphi}\hat{\psi}, \tag{4.3}$$

where $U(x)$ is an external potential and m_{c} and m_{i} denote the masses of the condensate and impurity atoms, respectively. The field operators are denoted $\hat{\varphi}$ for condensate bosons and $\hat{\psi}$ for thermal impurities. By integrating over transverse

degrees of freedom, the 1D interaction strengths are given by the well known expressions $g = 2\hbar\omega_{c\perp}a_{cc}$ and $g' = 2\hbar\sqrt{\omega_{c\perp}\omega_{i\perp}}a_{ci}$ where a_{cc} and a_{ci} denote the three-dimensional intraspecies (boson-boson) and interspecies (boson-fermion) scattering lengths [98, 99].

At very low temperatures the bosons undergo Bose-Einstein condensation. Provided that the bosons are weakly interacting ($gn_c \ll 1$ where n_c is the condensate density), we can make the mean-field approximation $\langle\hat{\varphi}\rangle \to \varphi_0$. The field φ_0 denotes the macroscopic wavefunction of the condensate, which obeys the GPE

$$i\hbar\frac{\partial\varphi_0}{\partial t} = -\frac{\hbar^2}{2m_c}\frac{\partial^2\varphi_0}{\partial x^2} + U(x)\varphi_0 + g|\varphi_0|^2\varphi_0 + g'n_i\varphi_0, \tag{4.4}$$

where $n_i = \langle\hat{\psi}^\dagger\hat{\psi}\rangle$ is the impurity density.

The condensate profile then appears as an external potential $V(x) = |\varphi_0(x)|^2$ for the impurity atoms, which we treat using a single-particle model. The single particle wavefunction of the fermions, denoted ψ, obeys the Schrödinger equation

$$i\hbar\frac{\partial\psi}{\partial t} = -\frac{\hbar^2}{2m_i}\frac{\partial^2\psi}{\partial x^2} + U(x)\psi + g'|\varphi_0|^2\psi. \tag{4.5}$$

Hamiltonian Eqs. (4.1)-(4.3) apply to both bosonic and fermionic impurities; here we consider the latter. Such Bose-Fermi mixtures have been realized experimentally and have been shown to be stable in quasi-1D [99–105]. In order for our 1D theory to be applicable, the system must be in the quasi-1D regime. This corresponds to the condition $\mu_c \ll \hbar\omega_{c\perp}$ for the condensate and $\mu_i \ll \hbar\omega_{i\perp}$ for the impurity atoms, where $\mu_{c,i}$ is the chemical potential of the condensate and impurities, respectively.

In the microscopic theory, the harmonic potential $U(x)$ is assumed to be sufficiently shallow such that $l_t \gg \xi$, where $l_t = \sqrt{\hbar/m_c\omega_{c,x}}$ is the effective length

scale of the trap and ξ is the healing length of the condensate. Therefore, the trap only weakly affects the solutions to Eqs. (4.4) and (4.5) and we set $U(x) = 0$ in the following. The background (Thomas-Fermi) confining potential provided by the BEC in a trap will however be important when we consider the semi-classical dynamics of the soliton in later sections.

Under the assumption $U(x) = 0$, Eq. (4.4) is known to have dark soliton solutions of the form $\varphi_0(x,t) = \tilde{\varphi}_0(x - v_s t)e^{-i\mu_c t/\hbar}$. Recall from Section 1.3.1 in Chapter 1, we have

$$\tilde{\varphi}_0(x - v_s t) = \sqrt{n_c}\left[i\frac{v_s}{c} + \gamma_s \tanh\left(\gamma_s \frac{x - v_s t}{\sqrt{2}\xi}\right)\right], \tag{4.6}$$

where v_s denotes the soliton velocity, n_c is the density of the condensate as $x \to \pm\infty$, $c = \sqrt{\mu_c/m_c}$ is the speed of sound in the condensate with chemical potential $\mu_c = gn_c$, $\gamma_s^2 = 1 - v_s^2/c^2$, and $\xi = \hbar/\sqrt{2}m_c c$ is the condensate healing length. We have also neglected the last term in Eq. (4.4), $\propto g' n_i$, because at very low densities the impurity atoms do not impede soliton creation and it is safe to assume the typical dark soliton profile for the condensate wavefunction [63].

We see from Eqs. Equation (4.5) and (4.6) that the dark soliton creates a potential well for the impurity atoms. First, we analyze the single particle scattering properties of the impurities due to the soliton well. In our further analysis we treat the soliton as a classical particle interacting with a bath of quantum scatterers, similar to the problem of a heavy particle moving through a gas of much lighter particles [106].

4.3 Impurity Scattering

We can rewrite Eq. (4.5) in the frame co-moving with the soliton by making the variable transformation $z = x - v_s t$, $t = t'$. Recalling the transformation of partial derivatives, $\partial_x = \partial_z$, $\partial_t = \partial_{t'} - v_s \partial_z$, Equation (4.5) is now given by

$$i\hbar\partial_t\psi(x,t) - i\hbar v_s\partial_z\psi(x,t) = -\frac{\hbar^2}{2m_i}\partial_z^2\psi(x,t) + g'|\varphi(z)|^2\psi(x,t) \tag{4.7}$$

We write the impurity wavefunction as $\psi(x,t) = e^{-iEt/\hbar}e^{im_i v_s z/\hbar}\psi(z)$, which gives

$$\left(E + \frac{m_i v_s^2}{2}\right)\psi(z) = -\frac{\hbar^2}{2m}\partial_z^2\psi(z) + g'|\varphi(z)|^2\psi(z) \tag{4.8}$$

$$|\varphi(z)|^2 = n_c\gamma_s^2\tanh^2\left[\frac{\gamma_s z}{\sqrt{2}\xi}\right] + g'n_c(1-\gamma_s^2) \tag{4.9}$$

We now have a time-independent equation for the envelope function $\psi(z)$. Using $\tanh^2(x) = 1 - 1/\cosh^2(x)$, this equation can be recast into the form

$$-\frac{\hbar^2}{2m_i}\partial_z^2\psi(z) - \frac{g'n_c\gamma_s^2}{\cosh^2(\gamma_s z/\xi)}\psi(z) = \left(E + \frac{m_i v_s^2}{2} - g'n_c(1-\gamma_s^2) - g'n_c\gamma_s^2\right)\psi(z) \tag{4.10}$$

Finally, redefining $z = \gamma_s z/\sqrt{2}\xi$, we have a dimensionless equation the following time-independent Schrödinger equation for impurity atoms,

$$\frac{\partial^2\psi(z)}{\partial z^2} + \left[\frac{\lambda(\lambda-1)}{\cosh^2 z} + k^2\right]\psi(z) = 0, \tag{4.11}$$

where

$$\lambda(\lambda-1) = \frac{2m_i g'}{m_c g}\ ;\ k^2 = \frac{4m_i\xi^2}{\hbar^2\gamma_s^2}\left(E + \frac{m_i v_s^2}{2} - g'n_c\right). \tag{4.12}$$

The potential in Eq. (4.11) is known as the Pöschl-Teller potential, whose solutions are known in the form of hypergeometric functions and has been widely studied in

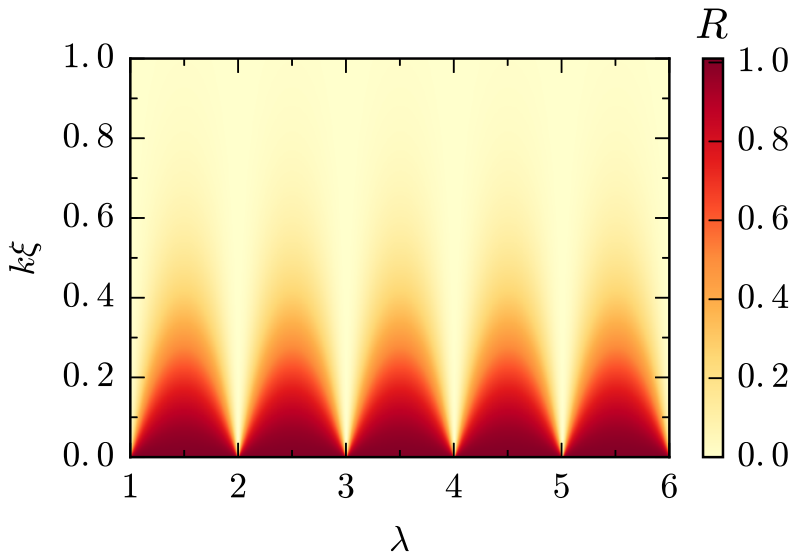

FIGURE 4.1: The reflection coefficient $R(k,\lambda)$ as a function of λ where $\lambda(\lambda-1) = 2m_i g'/m_c g$. $R(k,\lambda)$ is strongly peaked at $k \approx 0$ and is periodic as a function of λ. When λ is an integer $R(k,\lambda)$ is exactly zero.

the context of supersymmetric quantum mechanics [106–112]. The full solution of Eq. (4.11) is shown in Appendix C. The reflection coefficient of scattering states is

$$R(k,\lambda) = \frac{1-\cos(2\pi\lambda)}{\cosh(2\pi k)-\cos(2\pi\lambda)}. \tag{4.13}$$

$R(k,\lambda)$ vs. λ is shown in Figure 4.1. Furthermore, $R(k,\lambda) = 0$ when λ takes integer values, thus the soliton can become reflectionless to the impurities. The soliton potential well can also have bound states. The total number of bound states is the largest positive integer $j < \lambda - 1$. One or two fermionic impurities may occupy each bound state in the soliton core, and these bound particles affect the phase shift of scattered impurities. The effect of bound states and scattering state phase shifts are taken into account when we calculate the chemical potential of the fermions in Appendix D.

4.4 Kinetic Theory of Dark Solitons

The energy of the soliton texture in Eq. (4.6) is calculated by subtracting the uniform condensate background,

$$E(v_\mathrm{s}) = \frac{4\hbar n_\mathrm{c} c}{3}\left(1-\frac{v_\mathrm{s}^2}{c^2}\right)^{3/2} \approx \frac{4\hbar n_\mathrm{c} c}{3} - \frac{M v_\mathrm{s}^2}{2}. \tag{4.14}$$

Here we expanded $E(v_\mathrm{s})$ under the condition $v_\mathrm{s} \ll c$. The soliton is effectively a particle with negative mass of magnitude $M = 4\hbar n_\mathrm{c}/c = 4\sqrt{2}n_\mathrm{c}\xi m_\mathrm{c}$. The soliton is heavy compared to a single atom, $m_\mathrm{c} \ll M$, with width ξ/γ_s. The heavy mass and localized nature of the dark soliton justifies the following classical treatment of its dynamics [113].

We note here that M is often called the "inertial mass", whereas one can also define the "gravitational mass" (M_g) of a soliton, which is also negative. Gravitational mass is the missing mass of the atoms in the soliton core, given by integrating over the soliton density with the uniform background subtracted, $-M_\mathrm{g} = m_\mathrm{c}\int dx(n_\mathrm{s} - n_\mathrm{c})$, where $n_\mathrm{s}(x,t) = |\tilde{\varphi}_0(x - v_s t)|^2$ from Eq. (4.6). For a stationary soliton, $M_\mathrm{g} = 2\sqrt{2}n_\mathrm{c}\xi m_\mathrm{c}$ and $M = 2M_\mathrm{g}$. In the case of harmonic confinement the soliton has gravitational potential energy $U(x_\mathrm{s}) = -M_\mathrm{g}\omega_{\mathrm{c},x}^2 x_\mathrm{s}^2/2$. This distinction is important for the soliton's classical equation of motion, given by $-M\ddot{x} = M_\mathrm{g}\omega_{\mathrm{c},x}^2 x$. Dark solitons are quite stable in a harmonic trap and oscillate as a classical particle would, with effective frequency $\omega = \omega_{\mathrm{c},x}/\sqrt{2}$ [113–115].

In order to describe the diffusive behavior of solitons, we need to understand how the trajectory of a single soliton will deviate from the average trajectory computed for many solitons. Soliton dynamics can be most readily examined by understanding their probability distribution function (PDF) $f(t, x_\mathrm{s}(t), v_\mathrm{s}(t))$. The

soliton PDF obeys the kinetic equation

$$\frac{\partial f}{\partial t} + v_{\rm s}\frac{\partial f}{\partial x_{\rm s}} + \dot{v}_{\rm s}\frac{\partial f}{\partial v_{\rm s}} = \mathcal{I}\left[f\right], \tag{4.15}$$

where the collision integral $\mathcal{I}\left[f\right]$ accounts for scattering of impurities off of the soliton. As the soliton is much heavier than the impurities, $M \gg m_{\rm i}$, the transferred momentum to and from the soliton due to collisions is small. This assumption results in a collision integral of Fokker-Plank form

$$\mathcal{I}\left[f\right] = \frac{\partial}{\partial v_{\rm s}}\left(-A_{v_s} f + \frac{\partial}{\partial v_{\rm s}}\left[B_{v_s} f\right]\right), \tag{4.16}$$

which we derive in Appendix E. The transport coefficients A_{v_s} and B_{v_s} account for drift and diffusion of the distribution and are

$$A_{v_{\rm s}} = -\frac{2\hbar}{M}\sum_k kR_{k,\lambda}\left|\frac{\partial\epsilon_k}{\hbar\partial k}\right| n_{\rm F}(\epsilon_{k+k_{\rm s}})\left[1 - n_{\rm F}(\epsilon_{-k+k_{\rm s}})\right]. \tag{4.17}$$

$$B_{v_{\rm s}} = \frac{2\hbar^2}{M^2}\sum_k k^2R_{k,\lambda}\left|\frac{\partial\epsilon_k}{\hbar\partial k}\right| n_{\rm F}(\epsilon_{k+k_{\rm s}})\left[1 - n_{\rm F}(\epsilon_{-k+k_{\rm s}})\right]. \tag{4.18}$$

Where $n_{\rm F}(\epsilon_k)$ is the Fermi-Dirac distribution for the impurity atoms, which is shifted by $k_{\rm s}$ because we calculated the reflection coefficient $R(k,\lambda)$ in frame comoving with the soliton. The impurities have the usual dispersion relation $\epsilon_k = \hbar^2k^2/2m_{\rm i}$, and the last term $[1 - n_{\rm F}(\epsilon_{-k})]$ accounts for Pauli-blocking effects on impurity scattering.

To the lowest order in $k_{\rm s}$, we expand $n_{\rm F}(\epsilon_{k+k_{\rm s}})$ to find $A_{v_{\rm s}} = \gamma v_{\rm s}/M$ and $B_{v_{\rm s}} = \gamma k_{\rm B}T/M^2$, where γ is

$$\gamma = \frac{2\hbar^2}{k_{\rm B}T}\sum_k k^2R_{k,\lambda}\left|\frac{\partial\epsilon_k}{\hbar\partial k}\right| n_{\rm F}(\epsilon_k)\left[1 - n_{\rm F}(\epsilon_{-k})\right]. \tag{4.19}$$

This exact expression shows that A_{v_s} and B_{v_s} are not independent but intrinsically connected via the relation $A_{v_s} = M v_s B_{v_s}/k_B T$. This guarantees that the collision integral vanishes when $f(v_s)$ is given by the classical Maxwell-Boltzmann distribution. For a positive mass object this corresponds to thermal equilibrium, however for negative mass particles the situation is more complicated.

The crucial difference between Eq. (4.16) and the typical collision integral for a positive mass object is that the drift term $A_{v_s} \propto v_s$ is *negative*, indicating that over time the distribution drifts from lower to higher velocities. Thus, Eq. (4.15) does not have a stationary solution. We show below that this leads to the absence of diffusion in free space, where diffusion is formally defined as variance in position that grows linearly in time, $\langle \bar{x}^2 \rangle \propto t$. The apparent unbound runaway of the distribution function is a result of the expansion of the energy in Eq. (4.14) for $v_s \ll c$, as discussed in further detail below. If we consider the full energy spectrum then the system does reach equilibrium, where the dark soliton accelerates to the speed of sound and disappears. However, to describe the initial soliton trajectory we choose to work in the regime $v_s \ll c$ where the collision integral takes the simple form given by Eq. (4.16).

We note that in the case of bosonic impurities, instead of Pauli blocking factor, there is a Bose enhancement factor, $[1 + n_B(\epsilon_{-k})]$ where n_B is the Bose-Einstein distribution. This factor has been overlooked previously [54, 90], but it strongly influences the magnitude of the friction coefficient for a degenerate gas of impurities [63]. Moreover, the factor is crucial for satisfying the fundamental relation $A_{v_s} = M v_s B_{v_s}/k_B T$, which is dictated only by equilibrium properties and is not sensitive to the nature of the impurities [106].

Finally, combining Eqs. (4.15) and (4.16), we find the following Kramer's type

equation for the soliton distribution function

$$\frac{\partial f}{\partial t} + v_{\rm s}\frac{\partial f}{\partial x_{\rm s}} = \frac{\partial}{\partial v_{\rm s}}\left(-\Gamma v_{\rm s} f - \frac{\partial_{x_{\rm s}} U}{M} f + \Gamma v_{\rm th}^2 \frac{\partial f}{\partial v_{\rm s}}\right) \tag{4.20}$$

where $\Gamma = \gamma/M$ and $v_{\rm th}^2 = k_{\rm B}T/M$. This equation is analytically solvable in the case of harmonic confinement, $U(x_{\rm s}) = -M_{\rm g}\omega_{{\rm c},x}^2 x_{\rm s}^2/2$. At the end of this section we present the full solution to Equation (4.20) by method of characteristics.

The Langevin equation of motion for a single soliton can be inferred from the Fokker-Planck equation, and it is given by

$$-M\ddot{x}_{\rm s} = -\gamma\dot{x}_{\rm s} + M\omega^2 x_{\rm s} + f_{\rm s}(t) \tag{4.21}$$

where $\omega = \omega_{{\rm c},x}/\sqrt{2}$. The stochastic Langevin force is characterized by white-noise correlations with $\langle f_{\rm s}(t)\rangle = 0$ and $\langle f_{\rm s}(t')f_{\rm s}(t)\rangle = 2\gamma k_{\rm B}T\delta(t-t')$. From this equation we see that γ plays the role of the friction coefficient.

At fixed impurity number, γ depends on three parameters: the temperature T, the parameter λ, and the impurity chemical potential μ_i, which is itself a function of λ and T. Figure 4.2 shows γ as a function of λ for four different temperatures; γ grows over many orders of magnitude as λ is tuned from integer to half integer values. The integral over k in Eq. (4.19) is strongly peaked around $k = 0$. Therefore, approximating $n_{\rm F}(\epsilon_{k=0})\left[1 - n_{\rm F}(\epsilon_{k=0})\right] \approx e^{-\beta\mu_{\rm i}}$ and integrating over k, one finds the following expression for the friction coefficient,

$$\gamma \approx \frac{3\hbar^3 e^{-\mu_{\rm i}/k_{\rm B}T}}{2\pi^5 m_{\rm i} k_{\rm B} T \xi^4}\sin^2(\pi\lambda). \tag{4.22}$$

Recalling that $\lambda(\lambda-1) = 2m_{\rm i}g'/m_{\rm c}g$, we see clearly that the system can be tuned to the frictionless limit where $\gamma = 0$ without changing the number of impurities. Furthermore, friction provides an anti-damping force to the soliton, while

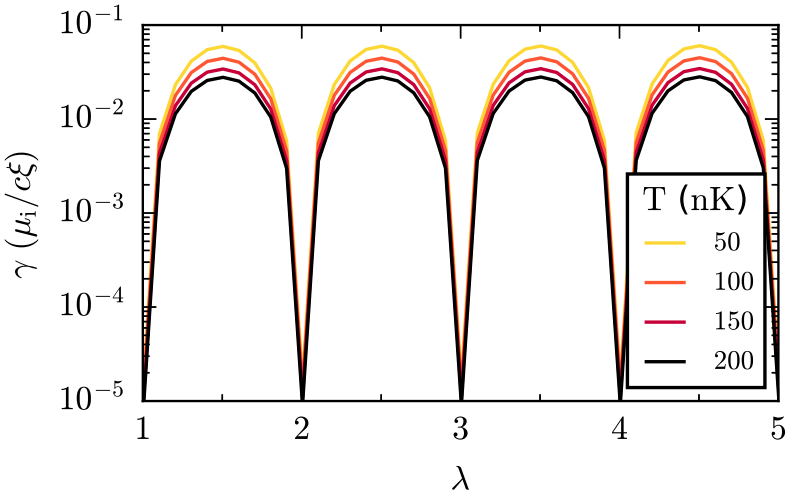

FIGURE 4.2: The soliton friction coefficient γ is periodic as a function of λ where $\lambda(\lambda-1) = 2m_{\rm i}g'/m_{\rm c}g$. Friction vanishes for integer λ, indicating that the soliton is reflectionless to scatterers. A system with tunable interactions enables tuning γ without changing the number of scatterers. γ is calculated in units of $\mu_{\rm i}/c\xi$ where $\mu_{\rm i}$ is the chemical potential of impurities, c is the speed of sound in the condensate and ξ is the condensate healing length. For impurities of ^{173}Yb as we have calculated here, γ decreases with increasing temperature. Increasingly dark lines indicate higher temperatures.

the background harmonic potential provides a confining force. The interplay of friction and confinement lead to the emergence of Brownian motion in the system.

Here we present an analytical solution of Eq. (4.20) for a soliton in harmonic trap with potential $U(x) = -M\omega^2 x^2/2$. In the following it is instructive to introduce dimensionless units as follows $t \to t/\Gamma$, $\omega \to \omega\Gamma$, $v_s \to v_{\rm th}v_s$, $x \to v_{\rm th}x/\Gamma$. In these units, the Fokker-Planck equation is

$$\frac{\partial f}{\partial t} + v_{\rm s}\frac{\partial f}{\partial x_{\rm s}} - \omega^2 x_{\rm s}\frac{\partial f}{\partial v_{\rm s}} = \frac{\partial}{\partial v_{\rm s}}\left(-v_{\rm s}f + \frac{\partial f}{\partial v_{\rm s}}\right), \tag{4.23}$$

where $\Gamma = \gamma/M$ and $v_{\rm th}^2 = k_{\rm B}T/M$ can be interpreted as the thermal velocity. Eq. (4.23) needs to be supplemented by the initial conditions. We assume

that the soliton is created in the trap center with initial velocity v_i, resulting in $f(0, x_\mathrm{s}, v_\mathrm{s}) = \delta(x_\mathrm{s})\delta(v_\mathrm{s} - v_\mathrm{i})$. This second-order partial differential equation (PDE) can be reduced to first-order by Fourier transform. Setting

$$f(t, x_\mathrm{s}, v_\mathrm{s}) = \sum_{p,q} \bar{f}(t, p, q) e^{ipx_\mathrm{s} + iqv_\mathrm{s}}, \tag{4.24}$$

we find the following first-order PDE

$$\frac{\partial \bar{f}}{\partial t} - (p+q)\frac{\partial \bar{f}}{\partial q} + \omega^2 q \frac{\partial \bar{f}}{\partial p} = -q^2 \bar{f} \tag{4.25}$$

with the transformed initial condition $\tilde{f}(0, p, q) = e^{-iqv_i}$. Eq. (4.25) can be solved analytically using the method of characteristics. According to the method, the PDE can be transformed to a system of ordinary differential equations (ODE) along characteristic lines, parametrized by s and defined as follows

$$\frac{d\bar{f}'}{ds} = -q^2(s)\bar{f}, \qquad \frac{dt}{ds} = 1 \quad \frac{dq}{ds} = -\left[p(s) + q(s)\right] \qquad \frac{dp}{ds} = \omega^2 q(s) \tag{4.26}$$

$$\bar{f}'(0) = \bar{f}(0, p_0, q_0), \qquad t(0) = 0, \quad q(0) = q_0, \qquad p(0) = p_0, \tag{4.27}$$

where we introduced $\bar{f}'(s) = f(t(s), p(s), q(s))$ and Eqs. (4.27) are the initial conditions written in a general form. Integration of (4.26) results in $\bar{f}(s) = \exp(Z)$, where

$$\begin{aligned} Z = {} & \frac{e^{-s}}{8\omega^2\bar{\omega}^2}\left[4\omega^2 p_0(p_0+q_0) + 4q_0^2\omega^4 - (p_0^2 + 4p_0q_0\omega^2 + q_0^2\omega^2)\cos(2\bar{\omega}s)\right. \\ & \left. + 2\bar{\omega}(p_0^2 - q_0^2\omega^2)\sin(2\bar{\omega}s)\right] - \frac{q_0\omega^2 + p_0^2}{2\omega^2} - iq_0v_i \end{aligned} \tag{4.28}$$

$$t(s) = s \quad p(s) = \frac{e^{-s/2}}{\bar{\omega}}\left[p_0\bar{\omega}\cos(\bar{\omega}s) + \frac{p_0 + 2q_0\omega^2}{2}\sin(\bar{\omega}s)\right]$$

$$q(s) = \frac{e^{-s/2}}{\bar{\omega}}\left[q_0\bar{\omega}\cos(\bar{\omega}s) - \frac{2p_0 + q_0}{2}\sin(\bar{\omega}s)\right] \tag{4.29}$$

Where $\bar{\omega} = \sqrt{\omega^2 - 1/4}$. For each initial point q_0, p_0 and the parameter s we have the corresponding point $t(s, q_0, p_0)$, $q(s, q_0, p_0)$, $p(s, q_0, p_0)$ on the characteristic line along with $f'(s)$. After inversion of these relations $s(t, q, p)$, $q_0(t, q, p)$, $p_0(t, q, p)$ the general form of solution of the kinetic equation in the Fourier space is $\bar{f}(t, q, p) = \bar{f}'(s(t, q, p))$. The inversion of Eqs. (4.29) leads to

$$\begin{aligned} s &= t, \qquad p_0 = \frac{e^{t/2}}{\bar{\omega}} \left[p\bar{\omega} \cos(\bar{\omega}t) - \frac{p + 2q\omega^2}{2} \sin(\bar{\omega}t) \right] \\ q_0 &= \frac{e^{t/2}}{\bar{\omega}} \left[q\bar{\omega} \cos(\bar{\omega}t) + \frac{2p + q}{2} \sin(\bar{\omega}t) \right]. \end{aligned} \tag{4.30}$$

Where Eqs. (4.30) satisfy initial conditions (4.27). Finally, the general solution in Fourier space is given by

$$\tilde{f}(t, p, q) = \exp\left\{ -g_1(t, \omega)p^2 + g_2(t, \omega)pq - g_3(t, \omega)q^2 - iv_{\mathrm{i}} \left(g_4(t, \omega)p + g_5(t, \omega)q \right) \right\} \tag{4.31}$$

parametrized by the functions $g_i(t, \omega)$, where

$$g_1(t, \omega) = \frac{4\bar{\omega}^2(e^t - 1) - e^t \left[\cos(2\bar{\omega}t) + 2\bar{\omega} \sin(2\bar{\omega}t) - 1 \right]}{8\omega^2\bar{\omega}^2} \tag{4.32}$$

$$g_2(t, \omega) = \frac{e^t}{2\bar{\omega}^2} \left[\cos(2\bar{\omega}t) - 1 \right] \tag{4.33}$$

$$g_3(t, \omega) = \frac{4\bar{\omega}^2(e^t - 1) + e^t \left[2\bar{\omega} \sin(2\bar{\omega}t) - \cos(\bar{\omega}t) + 1 \right]}{8\bar{\omega}^2} \tag{4.34}$$

$$g_4(t, \omega) = \frac{e^{t/2}}{\bar{\omega}} \sin(\bar{\omega}t) \tag{4.35}$$

$$g_5(t, \omega) = \frac{e^{t/2}}{\bar{\omega}} \left[\bar{\omega} \cos(\bar{\omega}t) + \frac{1}{2} \sin(\bar{\omega}t) \right]. \tag{4.36}$$

Eq. (4.25) does not have a stationary solution where $\partial \tilde{f}/\partial t \to 0$, due to negative drift term, which causes the distribution to drift to higher velocities. Eq. (4.31) grows exponentially at long times; this is an artifact of the linear approximation for soliton momentum, $p \approx -Mv_s$. The approach is equally valid for the full soliton spectrum in Eq. (4.14), which is bounded, but does not admit an exact

analytical solution. Finally, transforming Eq. (4.31) back to real space we find the full distribution function $f(t, x_\mathrm{s}, v_\mathrm{s})$ with Gaussian form

$$f(t, x_\mathrm{s}, v_\mathrm{s}) = \frac{1}{2\pi\sqrt{4g_1g_3 - g_2^2}} \exp\left\{-\frac{1}{4g_1g_3 - g_2^2}\left[g_1 v_\mathrm{s}^2 + g_3 x_\mathrm{s}^2 + g_2 v_\mathrm{s} x_\mathrm{s}\right.\right.$$
$$\left.\left. - v_\mathrm{i} v_\mathrm{s}(g_2 g_4 + 2g_1 g_5) - v_\mathrm{i} x_\mathrm{s}(g_2 g_5 + 2g_3 g_4) + v_\mathrm{i}^2(g_3 g_4^2 + g_1 g_5^2 + g_2 g_4 g_5)\right]\right\}. \tag{4.37}$$

The distribution contains all information about the stochastic dynamics of a dark soliton.

4.5 Dark Soliton Trajectory

From the solution $f(t, x_\mathrm{s}, v_\mathrm{s})$ of Eq. (4.20), we can calculate exact expectation values for the soliton position and velocity. In experiments, it is generally easier to measure soliton position, which we focus on in the following. The average soliton trajectory (with units restored) is

$$\bar{x}_\mathrm{s}(t, \omega) = \frac{v_\mathrm{i} e^{\Gamma t/2}}{\bar{\omega}} \sin(\bar{\omega} t), \tag{4.38}$$

where $\bar{\omega} = \sqrt{\omega^2 - \Gamma^2/4}$ and v_i is the initial velocity of the soliton. The variance in soliton position, D_x, is

$$D_x(t, \omega) = \frac{v_\mathrm{th}^2(e^{\Gamma t} - 1)}{\bar{\omega}^2} + \frac{v_\mathrm{i}^2 e^{\Gamma t}}{\bar{\omega}^2} \sin^2(\bar{\omega} t) + \frac{v_\mathrm{th}^2 \Gamma^2 e^{\Gamma t}}{4\omega^2 \bar{\omega}^2}\left[1 - \left(\cos(2\bar{\omega} t) + \frac{2\bar{\omega}}{\Gamma}\sin(2\bar{\omega} t)\right)\right]. \tag{4.39}$$

The problem has an intrinsic timescale given by $\Gamma^{-1} = M/\gamma$. For $\Gamma t \gtrsim 1$, the soliton's position grows exponentially, indicative of the soliton rapidly reaching the

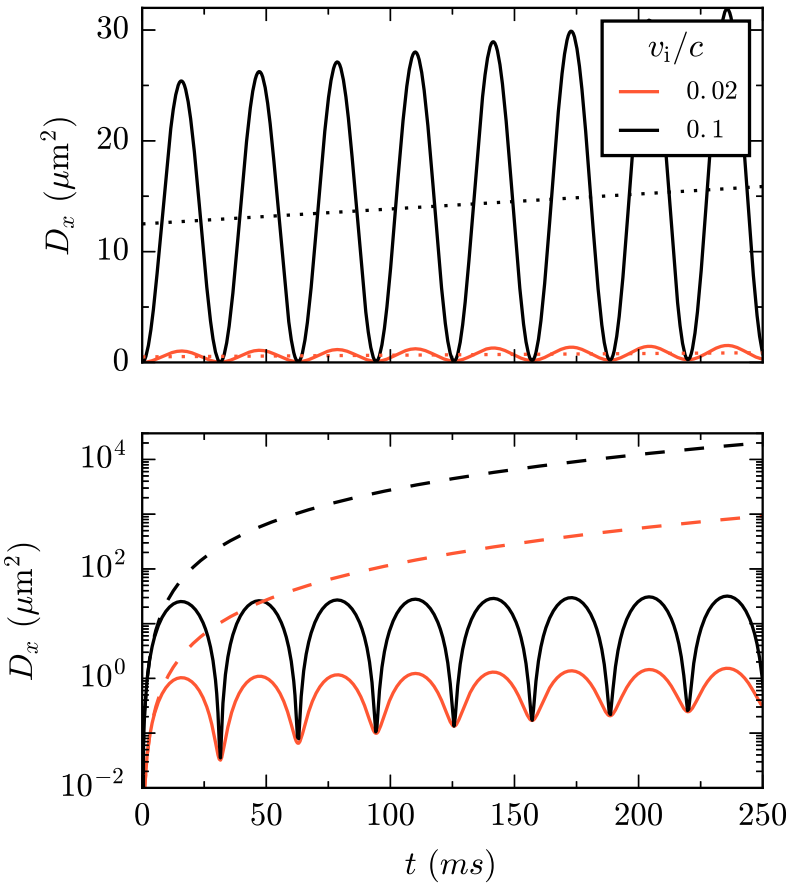

FIGURE 4.3: Variance in soliton position $D_x(t,\omega)$ as a function of time from the exact expression (4.39) for $v_i/c = 0.02$ (orange line) and $v_i/c = 0.1$ (black line) with $v_{th} \approx 0.1$ mm/s and $\Gamma^{-1} \approx 1$ s. Top: Results for a harmonic potential with $\omega = 100\Gamma$. D_x grows linearly in time with additional oscillations due to confinement. The amplitude of oscillation increases with increasing v_i. Dotted lines show the average value using the linear approximation in Eq. (4.40). Bottom: Comparison with $D_x(t,\omega)$ in the limit $\omega \ll \Gamma$ (dashed lines). In the absence of harmonic confinement, D_x initially grows like t^3 for $\Gamma t \ll 1$, then grows exponentially. There is no diffusive regime.

speed of sound and disappearing. We examine Eqs. (4.38) and (4.39) in the short-time limit $\Gamma t \ll 1$. The trap frequency ω also considerably affects the soliton dynamics. In the limit $\Gamma \ll \omega$, we find that diffusive behavior emerges, where

$D_x(t,\omega) \propto D_0 + D(t)t$ with a time-dependent diffusion coefficient

$$\langle D(t)\rangle \approx \frac{v_{\rm th}^2\Gamma}{\omega^2} + \frac{v_{\rm i}^2\Gamma}{\omega^2}\sin^2(\bar{\omega}t) - \frac{v_{\rm th}^2\Gamma^2}{2\omega^3}\sin(2\bar{\omega}t), \tag{4.40}$$

with offest $D_0 \approx v_{\rm i}^2/2\omega^2 + v_{\rm th}^2/4\omega^4$. However, in the opposite limit of $\omega \ll \Gamma$, the linear in t term vanishes, giving

$$D_x(t,\omega) \approx v_{\rm i}^2 t^2 + v_i^2\Gamma t^3 + \frac{2}{3}v_{\rm th}^2\Gamma t^3 \tag{4.41}$$

to lowest order in Γt. In the absence of the restoring force provided by background potential, the soliton undergoes ballistic transport $\propto t^3$, followed by the exponential growth of D_x. The exact expression for $D_x(t,\omega)$ is shown in Figure 4.3.

The mechanism of diffusion for dark solitons is thus inherently different than Brownian motion for positive mass objects. Friction forces cause the soliton to speed up, therefore the only restoring force in the problem is due to the background confining potential, which leads to the emergence of diffusive behavior. Finally, we see that in the frictionless limit, $\Gamma \to 0$, we have $D \to 0$, and there is no diffusion. For quantitative agreement with experiment, the initial velocity of the soliton $v_{\rm i}$ also plays a crucial role [63].

4.6 Soliton Lifetime

Integrating the distribution function $f(t, x_{\rm s}, v_{\rm s})$ over the spatial coordinate $x_{\rm s}$, we find the distribution of soliton velocities

$$f_v(t, v_{\rm s}) = \frac{1}{\sqrt{4\pi g_3(t,\omega)}}\exp\left(-\frac{(v_{\rm s} - \bar{v}_{\rm s}(t))^2}{4g_3(t,\omega)}\right), \tag{4.42}$$

parametrized by functions $g_3(t,\omega)$ and $\bar{v}_s(t)$. The function $g_3(t,\omega)$ is

$$g_3 = \frac{\left[4\bar{\omega}^2(e^{\Gamma t}-1) + e^{\Gamma t}\left(\Gamma^2 + 2\Gamma\bar{\omega}\sin(2\bar{\omega}t) - \Gamma^2\cos(2\bar{\omega}t)\right)\right]}{8\bar{\omega}^2} \tag{4.43}$$

The average velocity is $\bar{v}_s(t)$, which captures oscillations in the trap as well as exponential growth of the soliton velocity,

$$\bar{v}_s(t) = \frac{v_i e^{\Gamma t/2}}{\bar{\omega}}\left[\bar{\omega}\cos(\bar{\omega}t) + \frac{\Gamma}{2}\sin(\bar{\omega}t)\right]. \tag{4.44}$$

Starting from the velocity distribution function in Eq. (4.42), we impose a perfectly absorbing boundary condition at $v_s = \pm c$, reflecting that the soliton disappears once it reaches the speed of sound. This can be done using the method of images as discussed below.

The boundary perfectly absorbing boundary condition imposed is $f_v(\pm c, t) = 0$ for all times t. We construct a distribution that obeys this boundary condition using the method of images. The distribution function is reflected about the boundaries, $v_s = \pm c$ in our case, with "image distributions" placed at $v_n = 2cn$ for $n = \pm 1, \pm 2, ...$ The distribution which obeys the boundary condition is then described by the general formula

$$f_v^{\mathrm{Img}}(t, v_s) = f_v(t, v_s) + \sum_{n=1}^{\infty}(-1)^n\left[f_v(t, v_n - v) + f_v(t, -v_n - v)\right] \quad ; \quad v_n = 2cn. \tag{4.45}$$

We find the total survival probability of the soliton by integrating over v_s from $-c$ to c,

$$\mathcal{P}(|v_s| < c; t) = \int_{-c}^{c} dv_s \; f_{v_s}^{\mathrm{Img}}(v_s, t). \tag{4.46}$$

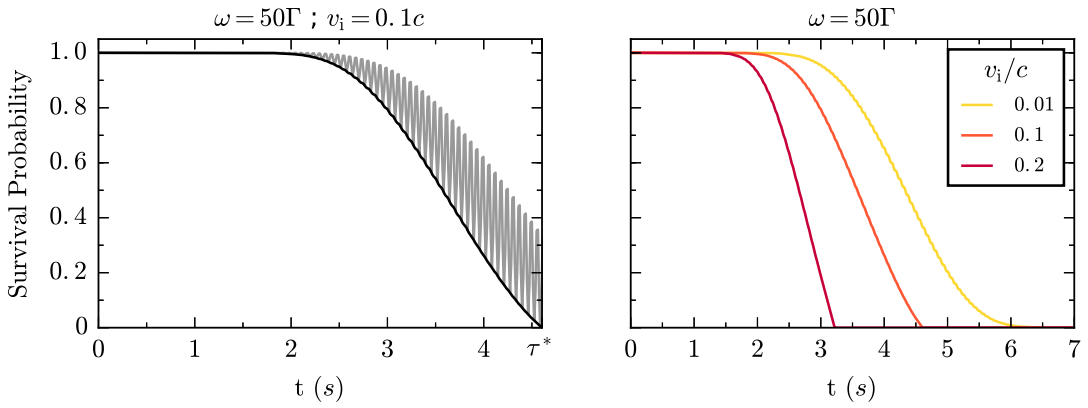

FIGURE 4.4: Left: Survival probability as defined by the exact expression in Eq. (4.47) (gray line) is highly oscillatory. The lower bound is given by replacing $\bar{v}_\mathrm{s}(t)$ with Eq. (4.48) (black line). Soliton lifetime is marked by $\tau*$ on the horizontal axis. Calculated for $v_\mathrm{i} = 0.1c$ and $\omega = 50\Gamma$. Right: Survival probability for different soliton initial velocities with $\omega = 50\Gamma$.

Since each term in $f^{\mathrm{Img}}_{v_\mathrm{s}}(v_\mathrm{s}, t)$ is a Gaussian, we integrate and find the following expression for the survival probability:

$$\begin{aligned}\mathcal{P}(|v_\mathrm{s}| < c; t) = \frac{1}{2}\left(\mathrm{Erf}\left[\frac{c - \bar{v}_\mathrm{s}(t)}{2\sqrt{g_3(t,\omega)}}\right] + \mathrm{Erf}\left[\frac{c + \bar{v}_\mathrm{s}(t)}{2\sqrt{g_3(t,\omega)}}\right]\right) \\ + \frac{1}{2}\sum_{n=1}^{\infty}(-1)^n\left(\mathrm{Erf}\left[\frac{c + v_n - \bar{v}_\mathrm{s}(t)}{2\sqrt{g_3(t,\omega)}}\right] + \mathrm{Erf}\left[\frac{c - v_n + \bar{v}_\mathrm{s}(t)}{2\sqrt{g_3(t,\omega)}}\right]\right. \\ \left. + \mathrm{Erf}\left[\frac{c - v_n - \bar{v}_\mathrm{s}(t)}{2\sqrt{g_3(t,\omega)}}\right] + \mathrm{Erf}\left[\frac{c + v_n + \bar{v}_\mathrm{s}(t)}{2\sqrt{g_3(t,\omega)}}\right]\right)\end{aligned} \tag{4.47}$$

The exact expression in Eq. (4.47) is oscillatory, because $\bar{v}_\mathrm{s}(t)$ and $g_3(t,\omega)$ capture oscillations in the trap as well as the long-time acceleration of the soliton. However, if the soliton velocity reaches c at any point in it's oscillation it will not survive, so we focus on the lower bound of $\mathcal{P}(|v_\mathrm{s}| < c; t)$, which can be found by replacing

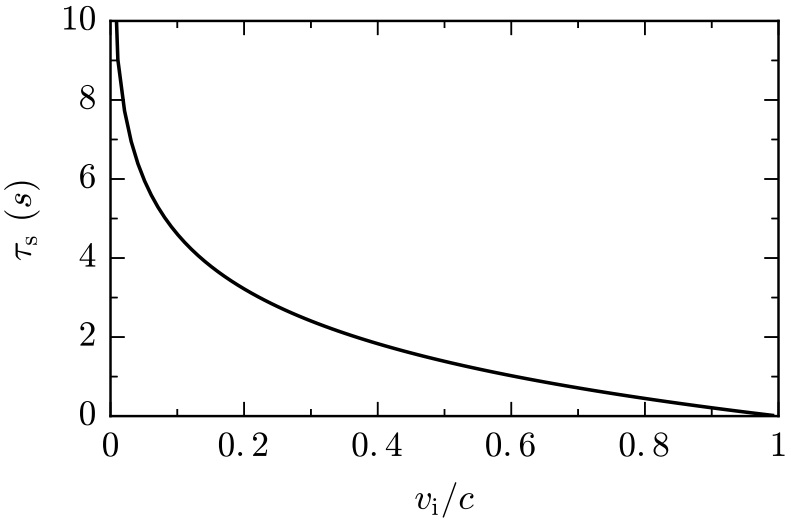

FIGURE 4.5: Soliton lifetime as a function of initial velocity v_i, with $\omega = 100\Gamma$ and where c is the condensate speed of sound. Solitons that start at higher initial velocities have a shorter lifetime, which one would intuitively expect. Soliton lifetime is only weakly dependent on trapping frequency ω.

$\bar{v}_s(t) \to \bar{v}_s^*(t)$ where $\bar{v}_s^*(t)$ is the maximum value over one oscillation period,

$$\bar{v}_s^*(t) = \frac{v_i e^{\Gamma t/2}}{\bar{\omega}} \sqrt{\bar{\omega}^2 + \Gamma^2/4} = \frac{v_i \omega e^{\Gamma t/2}}{\bar{\omega}}. \tag{4.48}$$

Making this substitution, we can plot a smooth survival probability curve. When $|\bar{v}_s^*(\tau_s)| = c$, $\mathcal{P}(|v_s| < c; \tau_s) = 0$, and we define τ_s as the soliton lifetime. The exact oscillatory expression and the lower envelope of the survival probability are shown in Figure 4.4. From Eq. (4.48) we find a simple expression for the lifetime,

$$\tau_s = \frac{2M}{\gamma} \ln\left(\frac{c\,\bar{\omega}}{v_i \omega}\right). \tag{4.49}$$

The soliton lifetime from Equation (4.49) is shown in Figure 4.5. The lifetime decreases as initial velocity increases, however it is only weakly dependent on the trapping frequency ω since $\bar{\omega} \approx \omega$ for $\omega \gg \Gamma$. Furthermore, soliton lifetime is

simply inversely proportional to the friction coefficient γ, and diverges as $\gamma \to 0$. Tuning the friction coefficient therefore should have a measurable effect in experiments, where soliton lifetime increases as γ decreases.

4.7 Experimental Implementation

In this Section we briefly discuss application of the theory in Section 4.3 and Section 4.4 to the experiment by Aycock, et. al. [63]. The system was an elongated BEC of $N_c \approx 10^6$ atoms of ^{87}Rb in the $|F = 1, m_F = 0\rangle$ state with chemical potential $\mu/\hbar\omega_\perp \simeq 9$ where $\omega_\perp$ is the transverse trapping frequency, and the temperature was 10 ± 5 nK. The systems longitudinal extent was $L \approx 250\mu$m, approximately 30 times the transverse Thomas-Fermi diameter. Long-lived solitonic excitations were intialized using the phase-imprint method [116, 117].

The solitons had an initial velocity of $v_s \approx 0.3$ mm/s and the speed of sound was $c \approx 1.4$ mm/s. The impurities were thermal ^{87}Rb atoms in the $|F = 1, m_F = 1\rangle$ state which were transferred via RF pulse prior to evaporation. Since ^{87}Rb does not have convenient Feshbach resonances for tuning interaction strength, the number of impurity atoms was varied. Therefore, the parameter λ remained constant throughout the experiment, with $\lambda \approx 1.5$, which corresponds to the maximum possible value of $R(k, \lambda)$ in Eq. (4.13). Soliton position vs. time is shown in Figure 4.6 for different impurity levels. The impurities affect the soliton in two ways: the lifetime of the soliton decreases and the variance in soliton position increases for different shots at each timestep.

The theory from Section 4.5 for the soliton trajectory was adapted for bosonic ^{87}Rb impurities and slightly modified to take experimental realities into account. The BEC cloud geometry had a finite transverse extent, implying that the dark soliton is in an unstable regime, where it will convert from a planar kink soliton to

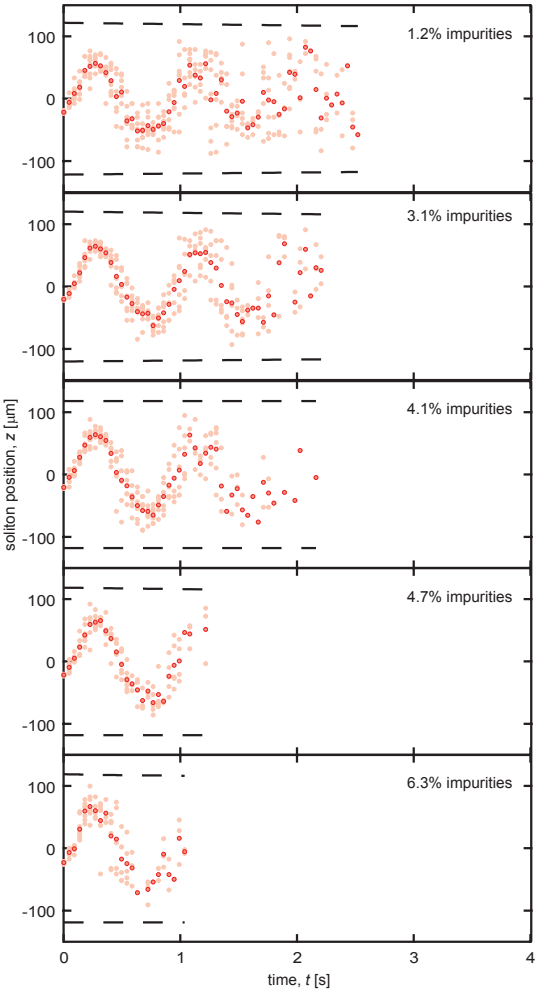

FIGURE 4.6: Impact of impurities. Here, we plot the position z_i of the soliton (light pink) vs. time t after the phase imprint for different impurity levels. The dark pink markers represent the average position $\langle z_i \rangle$ for each time t. Dashed lines represent the endpoints of the condensate vs. t. Data and Figure by L. M. Aycock [63].

a nearly planar solitonic vortex [54, 118]. For highly anisotropic geometries such as ours, the density profile of these two types of solitons is nearly the same as given by the profile in Eq. (4.6) and reflects that they become formally indistinguishable to the quantum impurity scatterers.

The finite transverse extent of the system necessitated the inclusion of multiple scattering modes for the bosonic impurities. Furthermore, the impurities

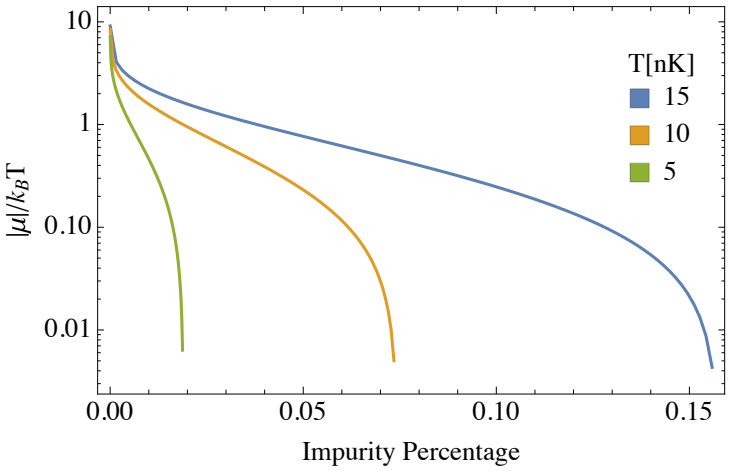

FIGURE 4.7: Chemical potential of thermal bosonic impurities with increasing impurity percentage. For all temperatures $\mu_i \approx 0$ for $N_{\rm imp}/N_{\rm c} \approx 0.2\%$.

began to condense at $\gtrsim 0.2\%$ impurities. We calculated the chemical potential of thermal bosons in the same way as in Appendix D to find the critical number of impurities for condensation, which occurs when $\mu_i = 0$. Unlike for the fermionic case here we did not include any bound states in the chemical potential calculation. For $\lambda \approx 1.5$ there is only a single, shallow bound state in the soliton well, and occupation of the bound state by an impurity atom can only occur through three body collisions (two impurity atoms and soliton), scenarios that we did not consider relevant to the experiment. Under these assumptions, the chemical potential of thermal bosons was calculated as shown in Figure 4.7.

We assumed that past the critical number for condensation, the number of thermal impurity scatterers remained constant and all additional impurities went into the newly formed impurity condensate. The kinetic theory for the soliton was the same as in Section 4.4, with a modified friction coefficient (as compared to Eq. (4.19))

$$\gamma = \frac{2\hbar}{k_{\rm B}T} \sum_{m,l} \int_{-\infty}^{\infty} \frac{dk_z}{2\pi} k_z^2 \left| \frac{\partial \epsilon}{\partial k_z} \right| R(k_z, \lambda) n_{\rm B}(\epsilon_k) \left[1 + n_{\rm B}(\epsilon_{-k})\right], \tag{4.50}$$

where $n_{\mathrm{B}}(\epsilon)$ is the Bose-Einstein distribution. The impurities' quasi-1D dispersion ϵ is

$$\epsilon_{m,l}(k_z) = \frac{\hbar^2 k_z^2}{2m_{\mathrm{Rb}}} + \frac{\hbar^2 j_{m,l}^2}{2m_{\mathrm{Rb}} R_\perp^2}, \tag{4.51}$$

where m_{Rb} is the mass of a single rubidium atom and we account for radial confinement with radius $R_\perp \approx 4\mu$m by summing over quantum numbers m and l corresponding to Bessel functions in the radial direction with zeros $j_{m,l}$; numerically we used $m = l = 20$ for the maximum value in the sum. Aside from the sum over transverse quantized modes, Eq. (4.50) differs from the fermionic counterpart, Eq. (4.19), by the occupation factor $n_{\mathrm{B}}(\epsilon)\left[1 + n_{\mathrm{B}}(\epsilon)\right]$. Rather than suppression of scattering due to Pauli blocking, bosonic impurities undergo bosonic enhancement. Scattering is always enhanced for increased impurity number until the impurities begin to condense. Using this friction coefficient, we calculated the diffusion coefficient from Eq. (4.40). After averaging over a single trap oscillation period, the soliton diffusion coefficient (with units restored) is

$$D \approx \frac{\gamma + \gamma_0}{M\omega^2}\left(\frac{k_{\mathrm{B}}T}{M} + \frac{v_i^2}{2}\right), \tag{4.52}$$

with soliton mass $M \approx 6000 \times m_{\mathrm{Rb}}$ and offset γ_0 which accounted for friction without impurities, the only fitting parameter. Figure 4.8 plots D measured experimentally (markers) and computed theoretically (curves; colored for different temperatures) as a function of $N_{\mathrm{imp}}/N_{\mathrm{c}}$.

The theory provides rather accurate estimates of the experimentally observed diffusion coefficient, with $\gamma_0 = 5.32 \times 10^{-4}$ mm^2/s. The fitting parameter γ_0 is set by the diffusion coefficient at zero impurities, where D is suppressed in agreement with our theory. Diffusion at zero impurity concentration could be due to a number of factors, including scattering of thermal phonons from the soliton, as well as

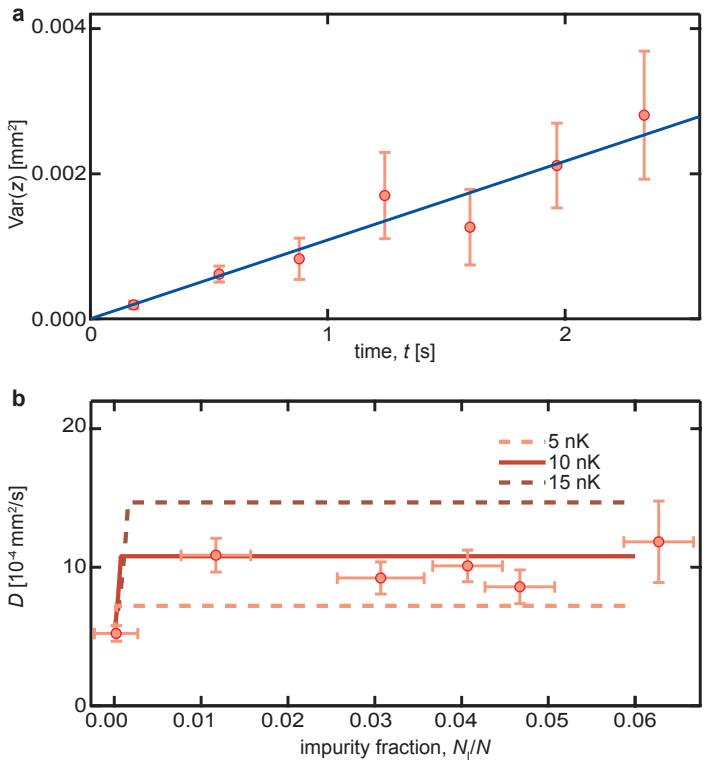

FIGURE 4.8: Brownian diffusion constant dependence on impurities. (a) An example for the linear fit of variance of z vs. t for 1.2% impurities. Data are binned into 0.36-s bins; the uncertainties are the sample standard deviation. (b) The diffusion coefficient D vs. impurity fraction $N_{\mathrm{imp}}/N_{\mathrm{c}}$. The experimental results (markers) are extracted from the slope of a linear fit of the sample variance Var(z) vs. time t. The uncertainty in D is the uncertainty from that fit. The theory curves (solid and dashed curves) plot the calculated D for our measured temperature. Data and Figure by L. M. Aycock, theoretical prediction for D based on Eq. (4.52) with friction coefficient from Eq. (4.50).

trap anharmonicity [54, 93]. In our quasi-1D system, the soliton is not reflectionless to phonons in the majority gas as it would be in 1D. The phonon contribution to soliton diffusion is due to coupling between longitudinal and tranverse degrees of freedom and is much smaller than the contribution from the externally imposed impurity species [54].

4.8 Conclusions

We calculated the friction coefficient γ and the diffusion coefficient $D(t)$ of a dark soliton in the presence of a non-interacting Fermi gas and a gas of bosonic impurities as related to experiment. We have shown that the soliton acts as a potential well for the impurities, and the scattering states and reflection coefficient of the impurities can be calculated exactly.

In this Section we estimate properties of a Bose-Fermi mixture of ^{174}Yb $-^{173}$ Yb, however the theory is general and applicable to other Bose-Fermi mixtures. We chose ^{174}Yb$-^{173}$Yb as a lab-realized example with scattering properties giving $m_{\rm i}g'/m_{\rm c}g \approx 1.3$ [119, 120].

We consider a quasi-1D BEC of ^{174}Yb atoms with $n_{\rm c}\xi \approx 100$ and speed of sound $c \approx 1$ mm/s, corresponding to a soliton mass of $M \approx 600m_{\rm c}$ and chemical potential $\mu_{\rm c} \approx \hbar \times 2$ kHz. For $T = 150$ nK, the thermal velocity of the soliton is $v_{\rm th} = \sqrt{k_{\rm B}T/M} \approx 0.1$ mm/s. The chemical potential requires a radial trapping frequency of $\omega_{\rm c\perp} \gtrsim 2\pi \times 10$ kHz for the quasi-1D criterion to be satisfied, and the shallow trapping direction should have $\omega_{{\rm c},x} \lesssim 2\pi \times 100$ Hz. We set the number of ^{173}Yb impurity atoms to $N_{\rm i} = 1000$. We choose the system length $L = 250$ μm, long enough that the continuum description of the impurity scattering states is appropriate. We find the chemical potential of fermions to be on the order of $k_{\rm B}T$, which requires a transverse trapping frequency $\omega_{\rm i\perp} \gtrsim 2\pi \times 10$ kHz for the fermions to be considered one-dimensional. For lower frequencies $\omega_{\rm i\perp}$ it is possible to obtain an accurate theory by summing over quantized transverse modes for the impurities as in Section 4.7.

Changing the magnitude of friction for the soliton requires tunable interactions. The most straightforward way of tuning interactions in the Yb system is by

changing the overlap of the transverse wavefunctions of the impurities and condensate atoms. This can be done by applying optical forces to either the bosonic or fermionic species which change the overlap of the atomic clouds. The narrow linewidths in the Yb spectra are ideal for this type of selective addressing, which can be done with high precision [121]. Bose-Fermi mixtures with different atomic species allow for other ways of tuning interactions by using Feshbach resonances or magnetic field gradients [122]. For the Yb s-wave scattering lengths that have already been measured, we find $\lambda \approx 2.2$ [119]. Such a system would only need to be tuned to slightly weaker interactions such that $\lambda \approx 2$ to see a decrease in friction coefficient and corresponding measurable increase in soliton lifetime. For attractive interspecies interactions ($g' < 0$) such as in ^{87}Rb $-^{40}$ K the soliton appears as a potential barrier rather than a well. The theory is still applicable in this case; the form of the reflection coefficient $R(k, \lambda)$ is slightly different but still periodic in λ and the physics is nominally unchanged [111].

We developed a general theory for the stochastic dynamics of negative mass objects using a kinetic equation approach. We find that the dynamics are drastically different from their positive mass counterparts - they do not undergo Brownian motion in free space. The proposed dark soliton-Fermi gas system provides an ideal experimental testbed in which to further study how friction and dissipation affects an object with negative mass.

We presented an analytical expression for the friction coefficient based on fermion scattering properties, including a term accounting for Pauli blocking, which is important to satisfy the equilibrium conditions on the transport coefficients. Using this result, we found exact expressions for the soliton position and position variance over time. We classified soliton trajectories at short times as diffusive and ballistic, and the diffusive regime can only be seen in the presence of a confining potential. The crossover timescale is given by $\Gamma^{-1} = M/\gamma$, which

we find to be on the order of a second. The intrinsic frequency $\Gamma \sim 1\text{Hz}$ is very low. Thus, the timescale over which diffusive behavior occurs is on the order of seconds and the diffusion coefficient can be directly measured [63]. Furthermore, the limit $\Gamma \ll \omega$ is justified for a reasonably shallow trapping potential which still preserves the soliton shape. Experiments with tunable interspecies interaction strength present the ability to tune the amount of friction at fixed impurity number, providing a simple way to manipulate the lifetime and trajectory of dark solitons in a laboratory setting.

Chapter 5: Mean-Field Theory of a Spin-1 Bose Gas in Synthetic Dimensions

5.1 Overview and Introduction

Internal degrees of freedom in atomic Bose-Einstein condensates (BECs) provide a platform for realizing phenomena conceived of in more traditional condensed matter settings. We view these discrete internal spin degrees of freedom as an extra "synthetic" dimension with finite extent, allowing phenomena in higher dimensions to exist in systems with lower real space dimension [64]. The setup considered in this Chapter consists of a one-dimensional (1D) spin-1 Bose gas in an optical lattice potential where the three hyperfine levels are "Raman" coupled using a pair of laser beams, a scheme which has been explored both theoretically and experimentally [64, 65, 123–127].

Experimental advances in ultra-cold atomic gases led to spin-orbit coupling (SOC) in spinful Bose and Fermi gases, one route for realizing synthetic dimensions [60, 128–130]. Despite the lack of true Bose-Einstein condensation in quasi-1D, in the weakly interacting mean-field (MF) regime the condensate wave function is well described by the 1D Gross-Pitaevskii equation (GPE) [60]. The introduction of a spin-orbit wave vector imbues the single particle energy dispersion with multiple minima in momentum space [131–133].

At low temperatures an interacting Bose gas can Bose-condense at these minima, forming a superfluid (SF) with density order: a charge density wave (CDW) [131, 132, 134, 135]. Moreover, different SF phases occur depending on the symmetry of the underlying Hamiltonian: spin density wave (SW) and magnetized

phases are two examples [136]. In spin-1/2 bosons, SOC can induce CDW and SW phases, however these are necessarily pseudospin systems and an SU(2)-breaking spin dependent interaction term is required to achieve these phases [135, 137]. For the case of spin-1 bosons, spin-dependent interactions preserve SU(2) symmetry which is then broken by SOC, leading to a rich phase diagram exhibiting multiple CDW and SW phases [133, 138–140].

The second ingredient to the synthetic dimension programme is an optical lattice. The system is loaded into a 1D lattice provided by counter propagating lasers with wavelength $\lambda_{\mathrm{L}} = 2\pi/k_{\mathrm{L}}$ where k_{L} is the recoil momentum. The hyperfine spin states $-F \leq m_F \leq F$ are viewed as an added spatial dimension, coupled using Raman lasers with a different wavelength $\lambda_{\mathrm{R}} = 2\pi/k_{\mathrm{R}}$. These components are shown in Fig. 5.1(a). Thus, the 1D system maps to a two dimensional ladder model with rungs of $2F + 1$ sites in width, leading to a square lattice in the tight binding approximation [see Fig. 5.1(c)]. The spatial dependence of the Raman coupling is essential to this analogy, as it gives each synthetic plaquette a flux $\Phi = 2\pi k_{\mathrm{R}}/k_{\mathrm{L}}$ [64]. In this space, the laser coupling of spin states gives hopping along the synthetic dimension direction. This allows for novel transport properties and topological states of matter to form and be probed [64, 65, 125, 127, 141].

This system was theoretically investigated for several different types of atoms and recent experiments observed chiral currents [64, 65, 123–126]. The mapping to a higher dimensional Hamiltonian is exact for single particle physics, but local interactions in the 1D system translate to non-local interactions in the synthetic direction. In this Chapter, we explore the combined effect of the Raman strength and spin-dependent interactions on phases at the MF level, without making tight binding or single band approximations. In particular, we focus on the regime of intermediate lattice depth where the mean-field description is applicable. At

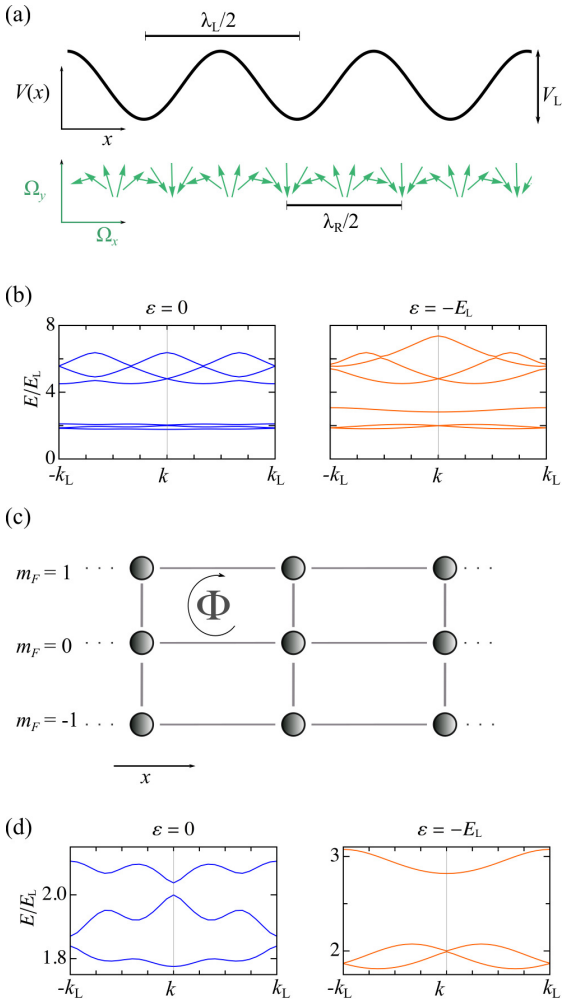

FIGURE 5.1: (a) The physical system consists of an optical lattice (black line, period $\lambda_{\mathrm{L}}/2$) with Raman lasers forming an effective helical magnetic field (green arrows, period $\lambda_{\mathrm{R}}/2$). (b) Single particle dispersion relation for the spin-1 spin-orbit coupled Bose gas in an optical lattice at $\Omega = 0.25E_{\mathrm{L}}$, $c_2 = 0$, $c_0 = 0$. (c) Synthetic dimensions visualization. They hyperfine levels m_F are viewed as an additional dimension with $2F + 1$ sites. Each plaquette has a uniform flux $\Phi \approx 2\pi k_{\mathrm{R}}/k_{\mathrm{L}}$. (d) Three lowest bands in the synthetic dimensions set up for $\Omega = 0.25E_{\mathrm{L}}$.

higher lattice depths, Mott physics becomes important and the GPE is an insufficient probe of the system. All of the parameter values used in our calculations are listed in Table 5.1.

Previous work on spin-orbit coupled bosons identified numerous MF phases without an optical lattice [138, 140, 142, 143], and with a deep optical lattice resulting in pinning effects and an interaction driven superfluid (SF) phase [144]. "Pinning" refers to condensation only at wavevectors commensurate with the underlying lattice [144]. The effect of increasing the lattice depth (that is intermediate between these two regimes) was also recently explored for spin-1/2 systems [145, 146]. A common feature of these systems is that the lattice causes the condensation at the Brillouin zone edge, which coincides with the wavevector of the optical lattice potential and not with the wavevector of spin-orbit coupling [144–146].

The physics that continuously connects the continuum limit to the deep lattice limit (i.e. both the single particle Hamiltonian, optical lattice, and tight binding) is largely unexplored for spin-1 spin-orbit coupled bosons. In light of recent experimental progress it is important to understand the possible ground state phases of this system including interactions to compare with all parameter ranges possible in experiment. We study the ground state properties of the spin-1 Bose gas with SOC and an optical lattice at the mean-field level by solving the GPE at zero temperature for weakly interacting bosons with either repulsive (polar) or attractive (ferromagnetic) spin-dependent interactions and repulsive density dependent interactions. Of particular interest is how the phases develop with increasing Raman coupling and how different phases manifest in the synthetic dimensions picture. Furthermore, we compare how the synthetic dimensions set up affects previously studied phenomena in the uniform system, such as the appearance of CDW phases [131, 133, 138].

The main result of this Chapter is shown in Figure 5.2, the phase diagrams for varying Raman strength Ω and ferromagnetic and polar spin-dependent interaction parameter c_2 for two different values of the quadratic Zeeman strength. We

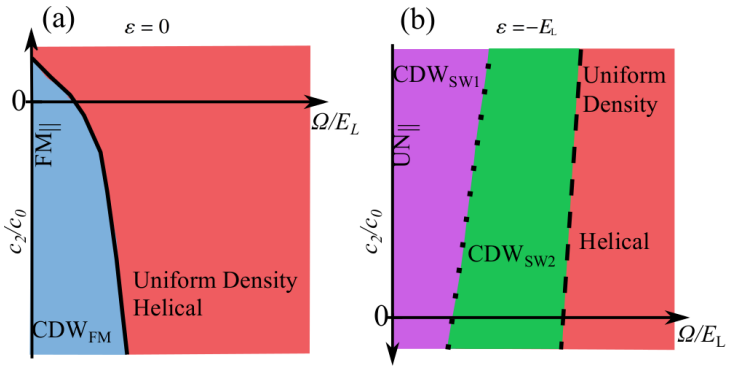

FIGURE 5.2: Schematic phase diagram for $\varepsilon = 0$ and $\varepsilon = -E_{\mathrm{L}}$. (a) $\varepsilon = 0$. For $\Omega \lesssim 0.5E_{\mathrm{L}}$ the system exhibits charge density wave behavior and spin polarization along S_x and is denoted $\mathrm{CDW_{FM}}$. Increasing Ω leads to a uniform density phase with a helical spin texture. The period of the spin helix is determined by the Raman field. Positive c_2 values suppress density fluctuations. (b) $\varepsilon = -E_{\mathrm{L}}$. The BEC exhibits distinct charge density wave phases with different ordering wavevectors and different spin textures, denoted $\mathrm{CDW_{SW1}}$ and $\mathrm{CDW_{SW2}}$. A cross over occurs between the two with increasing Ω. At $\Omega \approx 2.4E_{\mathrm{L}}$ there is a first order transition to a uniform density state with helical spin polarization.

briefly discuss our conclusions here, with more detail provided in Section 5.3. As expected from previous work [144], the lattice suppresses condensation at wavevectors other than $k = 0$ and the lattice wavevector $k = k_{\mathrm{L}}$ at the Brillouin zone edge. However, in the regime of interest this order is not completely suppressed and we predict several novel phases. Phases are labeled CDW or uniform density, with the type of spin texture denoted by the subscript in the CDW regimes. When the interaction strength is comparable to the Raman coupling, along with the CDW phases we find a variety of spin textures: a predominantly ferromagnetic state (FM) for $c_2 < 0$ and two different spin density waves (SW1, SW2) for $c_2 > 0$. Increasing Ω favors the single-particle ground state with uniform density and helical spin order. For the purposes of this Chapter, a "uniform density state" refers to a state where the total density is modulated only by the optical lattice. We relate

these phases to the synthetic dimensions picture by analyzing the spin current and fractional population of atoms in each spin state. The rich variety of phases reported here directly results from the interplay between interactions and the single particle Hamiltonian. We are able to establish what effects result directly from interactions by comparing our results with exact results for the ground state in the non-interacting case.

Our results align with MF phases previously studied without the lattice, and we conclude that the intermediate lattice depth modifies the phase boundaries but does not destroy phases that have already been predicted [138, 142, 143]. In addition, we characterize the lattice depth at which these phases are suppressed and the mean-field picture breaks down. Furthermore, we find that the ground state phase is dependent on the strength of the Raman coupling, which provides an additional tunable parameter in experiment. It is notable that increasing the Raman coupling strength at constant lattice depth leads to condensation at the Brillouin zone edge, a phenomenon that was previously predicted solely for increasing lattice depth [146]. Our model parameters were selected to be directly relevant to experiments with ferromagnetic atoms (e.g. ^{87}Rb, ^{7}Li, ^{41}K) as well as polar atoms (e.g. ^{23}Na) [65, 126, 127]. In Section 5.2 we explain the model and briefly review previous results. Section 5.3.1 and Section 5.3.2 give detailed results for attractive and repulsive spin-dependent interactions, respectively. The effects of increasing lattice depth are discussed in Section 5.3.3. We conclude in Section 5.4 and discuss how our work relates to current and future experiments. This chapter was previously published in Physical Review A,

5.2 Model and Method

We consider interacting spin-1 bosons in the presence of a Raman field and an optical lattice. The model is defined by $\hat{H} = \int dx(\hat{\mathcal{H}}_0 + \hat{\mathcal{H}}_{\rm so} + \hat{\mathcal{H}}_{\rm int})$, setting $\hbar = 1$ throughout. The non-interacting Hamiltonian density $\hat{\mathcal{H}}_0$ is

$$\hat{\mathcal{H}}_0 = \frac{1}{2M}\nabla\hat{\psi}^\dagger_\alpha\nabla\hat{\psi}_\alpha + \hat{\psi}^\dagger_\alpha\left[V(x) - \mu\right]\hat{\psi}_\alpha, \tag{5.1}$$

with the hyperfine states coupled through the spin-orbit coupling and interaction terms

$$\hat{\mathcal{H}}_{\rm so} = \hat{\psi}^\dagger_\alpha\left[\varepsilon(F_z^2)_{\alpha\beta} + \mathbf{\Omega}_{\rm R}(x)\cdot\mathbf{F}_{\alpha\beta}\right]\hat{\psi}_\beta, \tag{5.2}$$

$$\hat{\mathcal{H}}_{\rm int} = \frac{c_0}{2}\hat{\psi}^\dagger_\alpha\hat{\psi}^\dagger_\beta\hat{\psi}_\beta\hat{\psi}_\alpha + \frac{c_2}{2}\hat{\psi}^\dagger_\gamma\hat{\psi}^\dagger_\alpha\mathbf{F}_{\gamma\nu}\cdot\mathbf{F}_{\alpha\beta}\hat{\psi}_\beta\hat{\psi}_\nu, \tag{5.3}$$

using the notation defined in Table 5.1, with repeated indices summed over. In particular, the spatial structure of the the spin-orbit coupling term is given by $\mathbf{\Omega_R}(x) = \Omega\cos(2k_{\rm R}x)\mathbf{e}_x - \Omega\sin(2k_{\rm R}x)\mathbf{e}_y$.

The single particle physics of this system without a lattice was studied extensively in Ref. [133]. For small Ω and ε the low energy dispersion relation has three minima at $k = 0, \pm\, 2k_{\rm R}$ corresponding to spin states $m_F = 0, \pm 1$. These minima are degenerate when ε is tuned to slightly negative values with increasing Ω. Increasing ε shifts the middle minimum down, resulting in a single minimum structure, while decreasing ε shifts the middle minimum up, leading to a double minima structure. The dispersion relation for these two conditions is shown in Figure 5.1(b,d), where we plot the band structure for $\Omega = 0.25E_{\rm L}$ and $\varepsilon = 0$ and $-E_{\rm L}$. In the triply-degenerate regime, the condensate wavefunction takes the

Notation	Description	Value
$\hat{\psi}_\alpha(x)$	Boson field operator; $\alpha = m_F$	–
N	Number; $N = \int dx \, \langle \hat{\psi}_\alpha^\dagger \hat{\psi}_\alpha \rangle$.	$N = 100$
L	length of lattice	$L = 15\lambda_{\mathrm{L}}/2$
M	atomic mass	–
$V(x)$	Optical lattice potential; $V(x) = V_{\mathrm{L}} \cos^2(k_{\mathrm{L}} x)$	$V_{\mathrm{L}} = 5E_{\mathrm{L}}$
k_{L}	Lattice recoil momentum	$2\pi/\lambda_{\mathrm{L}}$
E_{L}	Lattice recoil energy $E_{\mathrm{L}} = k_{\mathrm{L}}^2/2M$	–
v_{L}	Lattice recoil velocity $v_{\mathrm{L}} = k_{\mathrm{L}}/M$	–
ε	Quadratic Zeeman strength	$\varepsilon = \begin{cases} 0, & c_2 < 0, \\ -E_{\mathrm{L}}, & c_2 > 0. \end{cases}$
$\mathbf{F}_{\alpha\beta}$	vector of spin-1 matrices	–
$\mathbf{\Omega}_{\mathrm{R}}(x)$	spin-orbit coupling; $\mathbf{\Omega}_{\mathrm{R}}(x) = \Omega \Re \left[e^{2ik_{\mathrm{R}}x} (\hat{\mathbf{x}} + i\hat{\mathbf{y}}) \right]$	Ω tuned
k_{R}	Raman wave vector	$k_{\mathrm{R}}/k_{\mathrm{L}} = 4/3.$
c_0	density-density interaction	$c_0 N/L = 0.1 E_{\mathrm{L}}$
c_2	spin-dependent interaction	$\frac{c_2}{c_0} = \begin{cases} -0.25, -0.5, -0.7 \\ 0.25, 0.5, 1.0 \end{cases}$

TABLE 5.1: Table of notation and values used for numerical simulations (if applicable). We tune the Raman field strength Ω and spin-dependent interaction c_2. Values for V_{L} and k_{R} come from the relevant experiment [65]. Interactions are related to scattering lengths a_0 and a_2 by $c_0 = 4\pi(a_0 + 2a_2)/3M$ and $c_2 = 4\pi(a_2 - a_0)/3M$ [60].

form [138]

$$\psi(x) = A_+ \xi_+ e^{i2k_{\mathrm{R}}x} + A_0 \xi_0 + A_- \xi_- e^{-i2k_{\mathrm{R}}x}, \tag{5.4}$$

where $A_{\pm,0}$ are complex amplitudes and $\xi_{\pm,0}$ are the single-particle spinor eigenstates at the energy minima corresponding to momenta $k = \pm 2k_{\mathrm{R}}, 0$. The condensate can exhibit a zero momentum phase or a plane wave phase when a single minimum is occupied, corresponding to $A_0 \neq 0, A_\pm = 0$ or $A_\pm \neq 0, A_{\mp,0} = 0$. The condensate also exhibits various density modulated (CDW) phases when at least two of the three components $A_{\pm,0}$ are nonzero. These CDW phases have different wavelengths depending how the minima are occupied [133].

For a weakly interacting condensate Eq. (5.4) is still a valid ansatz, but $A_{\pm,0}$

are selectively occupied to minimize both the single particle and interaction energies. Interactions dictate the form of the spinor structure in the condensate, favoring ferromagnetic order for attractive ($c_2 < 0$) and uniaxial nematic order for repulsive ($c_2 > 0$) spin-dependent interactions [138]. This is due to the fact that for $c_2 < 0$ (> 0), the system maximizes (minimizes) spin $\langle \hat{\mathbf{S}}(x) \rangle$, where $\hat{\mathbf{S}}(x) = \hat{\psi}^\dagger_\alpha(x) \mathbf{F}_{\alpha\beta} \hat{\psi}_\beta(x)$, leading to distinct phases in the two regimes [133, 138, 140, 142]. Furthermore, tuning ε also alters the ground state in the presence of interactions by changing the structure of the underlying dispersion relation [138]. This interplay between SW and CDW order leads to a number of exotic phases and excitations in the continuum system [138–140, 142].

One goal of this chapter is to understand the stability of each spin-orbit and interaction driven phase in the presence of an optical lattice, away from the deep-lattice limit. A lattice invalidates the ansatz of Eq. (5.4) since the lattice breaks translational symmetry, but essential features and minima of the lowest band remain intact as shown in Figure 5.1(b,d).

We describe a spinor BEC by three classical complex fields $\langle \hat{\psi}_\alpha(x) \rangle = \psi_\alpha(x) = \sqrt{n(x)} \xi_\alpha$ where $n(x) = \sum_\alpha |\psi_\alpha|^2$ is the total density, ξ_α is a three component spinor with normalization $\xi^*_\alpha \xi_\alpha = 1$, and $\alpha = \{1, 0, -1\}$ labels the synthetic dimension sites. We define the GPE energy functional by replacing the bosonic operators in Eqs. (5.1)-(5.3) with $\psi_\alpha(x)$. This gives the coupled equations

$$i\partial_t \psi_\alpha = \left\{ \left[-\frac{\nabla^2}{2M} + V(x) \right] \delta_{\alpha\beta} + \mathbf{\Omega_R} \cdot \mathbf{F}_{\alpha\beta} + \varepsilon (F_z^2)_{\alpha\beta} + c_0 |\psi|^2 \delta_{\alpha\beta} + c_2 \left[(\psi^\dagger_\delta \mathbf{F}_{\delta\gamma} \psi_\gamma) \cdot \mathbf{F}_{\alpha\beta} \right] \right\} \psi_\beta \quad (5.5)$$

We solve for the ground state using imaginary-time evolution where $t \to -i\tau$ [147] and test convergence using the strong criterion detailed in Ref. [148]. The system was initialized in a uniform state $\sum_\alpha |\psi_\alpha(x)|^2 = \mu/c_0$, with all 3 spin

components (ladder legs) equally weighted and where the number of particles fixes μ. We find that near the phase transitions there are several states that are close in energy. Our initial state biases the GPE solver and at some point in the phase diagram there is an artificial transition between phases, because sometimes the GPE relaxes to a metastable state rather than the ground state. To precisely pinpoint a transition, we ran the GPE over parameter ranges biasing the initial guess in favor of the previously calculated result at $\Omega \pm \delta\Omega$ (running from small to large Ω and large to small Ω). The lower energy phase is then taken as the ground state. As a heuristic check, we stochastically sampled points in the phase diagram using random initial conditions, confirming the ground state solution found from the above methodology. The parameter values used in the GPE solver are detailed in Table 5.1. Importantly, ε has a strong influence on phases and we present results for ferromagnetic BECs with $\varepsilon = 0$ and polar BECs with $\varepsilon = -E_{\mathrm{L}}$. These two choices are explained in Section 5.3.

CDW and SW phases are identified by nonzero Fourier amplitudes of the density and spin order parameters, $n(k)$ and $\langle \mathbf{S}(k) \rangle$, at the relevant wavevectors $k = 2k_{\mathrm{L}}$, $k = 2k_{\mathrm{R}}$, and $k = 4k_{\mathrm{R}}$. The first two correspond to the wavevector of the lattice and the spin-orbit field, respectively. Nonzero amplitude at $k = 2k_{\mathrm{L}}$ indicates an effect due to the lattice, while $k = 2k_{\mathrm{R}}$ indicates an effect due to SOC. The third wavevector, $k = 4k_{\mathrm{R}}$, corresponds to condensation at the two degenerate minima at $\pm 2k_{\mathrm{R}}$ in the single particle bandstructure (see Figure 5.1). The resolution of the system is set by the length L; here we have 5 unit cells because the Raman beam is periodic over 3 optical lattice sites. Density $n(k)$ and spin $\langle \mathbf{S}(k) \rangle$ are defined by $n(k) = \int dx\ e^{ikx} n(x)$ and $\langle \mathbf{S}(k) \rangle = \int dx\ e^{ikx} \langle \mathbf{S}(x) \rangle$. A schematic diagram of CDW phases in synthetic dimensions is shown in Figure 5.3(a-c). In synthetic space, these phases are captured by the fractional population in the m_F

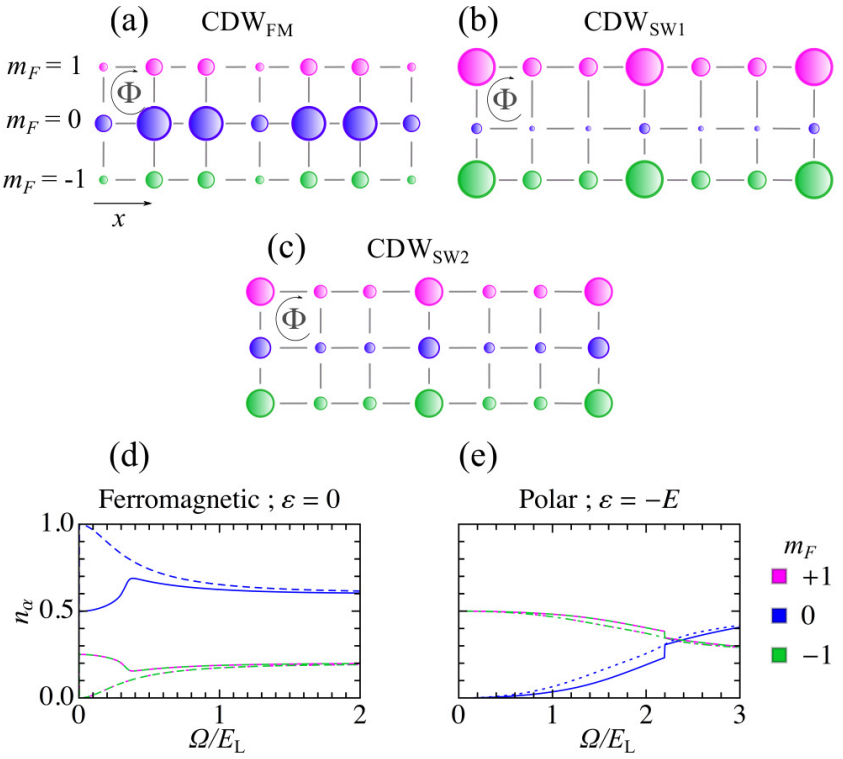

FIGURE 5.3: (a) Schematic diagram of the CDW$_{FM}$ phase. The BEC predominantly occupies $m_F = 0$ level. The total density is modulated at neighboring sites due to the Raman field. (b) Schematic diagram of the CDW$_{SW1}$ phase. The edges are preferentially occupied and there is an overall density modulation. (c) Schematic diagram of the CDW$_{SW2}$ phase. The bulk is more occupied than in (b), and the overall density modulation remains. (d-e) Fractional population as a function of Ω. (d) $c_2/c_0 = -0.25$, $\varepsilon = 0$; The system begins in a CDW$_{FM}$ ground state at $\Omega \approx 0$ with $n_0 = 1/2$ (top line) and $n_{\pm 1} = 1/4$ (bottom line) and moves to meet the single particle occupation. The non-interacting case is indicated by dashed lines. (e) $c_2/c_0 = 0.25, \varepsilon = -E_L$. The system starts with $n_{\pm 1} = 1/2$ (top line) and $n_0 = 0$ (bottom line). As Ω increases, it undergoes an edge to bulk first order transition at $\Omega \approx 2.0E_L$, which is weakened to a cross over in the limit $c_2 = 0$. As Ω increases the bulk is preferentially occupied. Dotted lines indicate the case for $c_0 \neq 0, c_2 = 0$.

states, shown in Figure 5.3(d-e). Fractional population n_α is defined as

$$n_\alpha = \frac{\int dk\, n_\alpha(k)}{\sum_\alpha \int dk\, n_\alpha(k)}. \tag{5.6}$$

Finally, we analyze the spin currents in this system, which is analogous to the chiral edge current in a quantum Hall system. The extremal spins represent the edges in the synthetic dimension [129]. This provides a way to visualize and measure chiral currents because the BEC can be imaged in the synthetic and spatial dimensions using spin-resolved absorption imaging [65]. The total spin current density is defined as

$$j_S \equiv \sum_\alpha \alpha \langle j_\alpha \rangle = \sum_\alpha \alpha \int \frac{dk}{2\pi} \frac{k}{M} \psi_\alpha^\dagger(k)\psi_\alpha(k), \tag{5.7}$$

where $\psi_\alpha(k) = \int dx\ e^{ikx}\psi_\alpha(x)$. Nonzero current corresponds to occupying states in the edge-site conduction bands of the corresponding 2D lattice system. In this case, the spin current is driven by the Raman beam Ω, and also depends on the population of atoms in the $m_F = \pm 1$ Zeeman (edge) states.

5.3 Results

5.3.1 Attractive Spin-Dependent Interactions

The schematic phase diagram for $c_2 < 0$ and $\varepsilon = 0$ is shown in Figure 5.2(a). For $\Omega = 0$ the system is an SU(2) FM [59, 149] with uniform charge density (i.e. the density is only suppressed by the lattice potential); this symmetry is broken by the Raman field. The physics at large Ω is largely explained by the single-particle Hamiltonian: The data matches up with exact diagonalization for $c_0 = c_2 = 0$ rather well.

For small Ω, the SU(2) FM phase and the modulating Raman field compete. In this regime, the charge redistributes itself to accommodate the FM phase in the presence of the Raman field. To understand this, consider the Raman field on

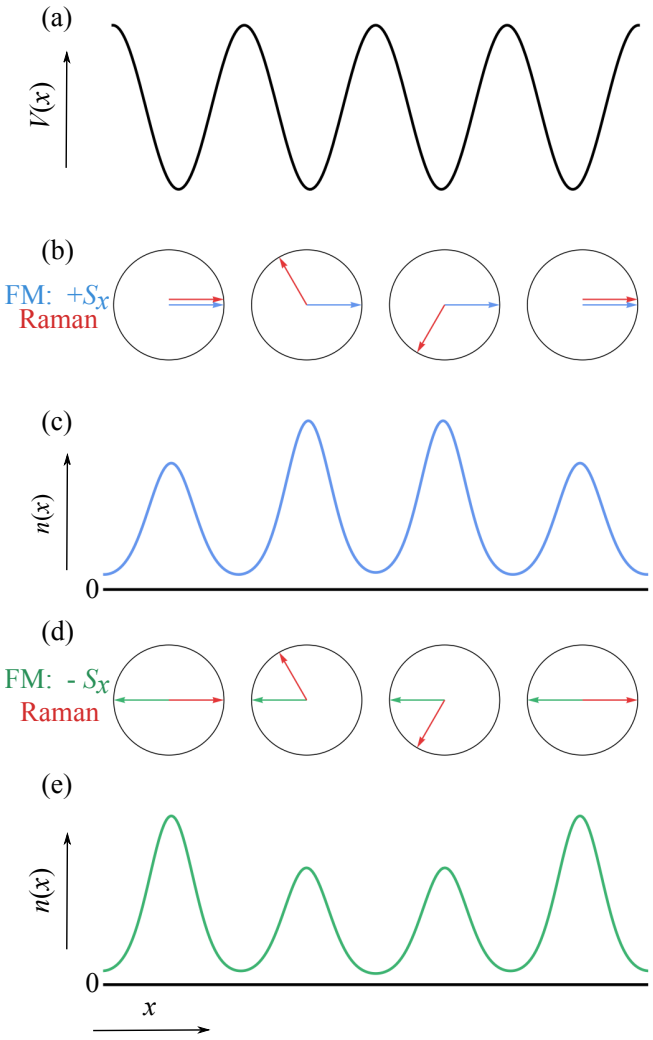

FIGURE 5.4: Interplay of spin and density for $c_2 < 0$ at small Ω. (a) Lattice potential $V(x)$. (b) Local spin polarization and Raman field at each site for $+S_x$ polarization. The blue arrow shows the spin polarization, and the red arrow shows the local Raman field. (c) $\mathrm{CDW}_{\mathrm{FM}}$ phase with $+S_x$ polarization. Density increases at sites where $\mathbf{F} \cdot \mathbf{\Omega}_{\mathrm{R}} < 0$. (d) Local spin polarization and Raman field at each site for $-S_x$ polarization. The green arrow shows the spin polarization, and the red arrow shows the local Raman field. (e) $\mathrm{CDW}_{\mathrm{FM}}$ phase with $-S_x$ polarization. Density increases at the sites where $\mathbf{F} \cdot \mathbf{\Omega}_{\mathrm{R}} < 0$.

each lattice site: The angle of the Raman field in the S_x-S_y plane is 0, $2\pi/3$, and $4\pi/3$ before it repeats itself every third site. Within the GPE, the wave function at each site l is $\psi_{\alpha,l} = \sqrt{n_l}\xi_{\alpha,l}$ with $\xi^{\dagger}_{\alpha,l}\xi_{\alpha,l} = 1$, and to leading order in Ω the

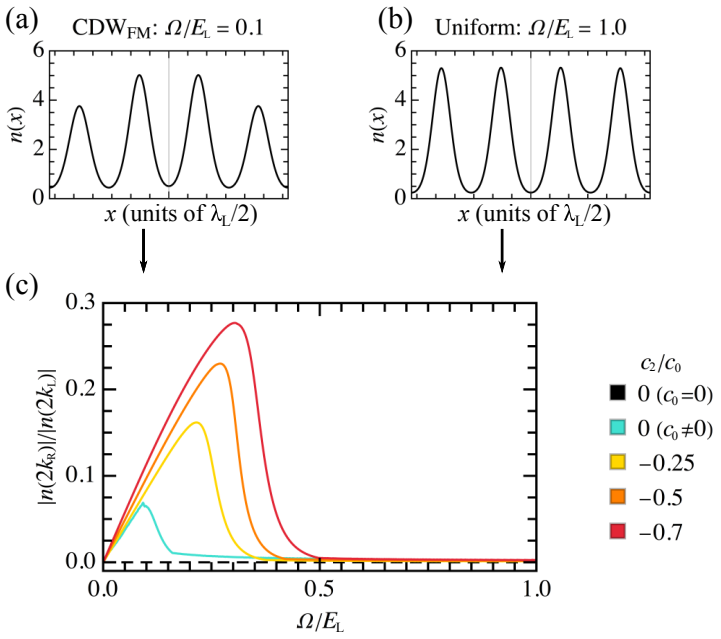

FIGURE 5.5: (a-b) GPE density computed for $c_2/c_0 = -0.25$ and $\varepsilon = 0$. (a) Density in real space in the CDW_{FM} phase shows modulation between lattice sites. (b) Density in real space in the uniform density phase. (c) $|n(2k_{\text{R}})| \neq 0$ signals a CDW phase. The non-interacting case (dashed line at 0) has density modulation only from the lattice, and only slight density modulation appears for $c_2 = 0, c_0 > 0$ (light gray, bottom line). Increasing spin-dependent interaction strength $|c_2|$ leads to greater overall density modulation until a cross over occurs to the uniform density regime. The largest peak (red/darker gray line) indicates largest interaction strength tested.

energy is changed by roughly

$$\Delta E \approx \sum_l n_l \; \xi^\dagger_{\alpha,l} \mathbf{F}_{\alpha\beta} \xi_{\beta,l} \cdot \mathbf{\Omega}_{\text{R}}. \tag{5.8}$$

For a given FM state, ΔE is minimized by larger density n_l at sites where $\xi^\dagger_{\alpha,l} \mathbf{F}_{\alpha\beta} \xi_{\beta,l} \cdot \mathbf{\Omega}_{\text{R}} < 0$ and smaller n_l when $\xi^\dagger_{\alpha,l} \mathbf{F}_{\alpha\beta} \xi_{\beta,l} \cdot \mathbf{\Omega_R} > 0$. This reasoning leads to two kinds of charge density waves as depicted in Figure 5.4. Our simulations suggest that Figure 5.4(b) is lower energy, shown in Figure 5.5(a). We

precisely track this $\mathrm{CDW_{FM}}$ regime by looking at Fourier modes of the density $n(k)$ at $k = 2k_{\mathrm{R}}$ as seen in Figure 5.5(c), which makes clear that the CDW is an interaction induced effect, increased by a larger FM interaction.

In Figure 5.6 we describe a system with $0 < \Omega/E_{\mathrm{L}} \lesssim 0.5$ that is polarized along S_x, connected to two other degenerate states with the transformation

$$\psi(x) \to e^{-\frac{2\pi i}{3}F_z}\psi(x - \pi/k_{\mathrm{L}}). \tag{5.9}$$

We confirmed numerically that the above transformation yields degenerate states with the same energy, and one would expect this from the above reasoning. The precise nature of the FM state with increasing Ω is captured in Figure 5.6 where we see that $\langle S_x(k)\rangle$ is at first only modulated at $2k_{\mathrm{L}}$ and $\langle S_y(k)\rangle$ is quite small, but as the Raman field Ω increases we obtain a small SW in $\langle S_y(x)\rangle$, shown in Figure 5.6 (c,d). This minimizes the energy in Eq. (5.8), as depicted in Figure 5.4.

For strong enough Ω, the easy axis ferromagnetic order is suppressed and the helical order of the single particle picture takes over, as indicated in Figure 5.3(c) by the increase in occupation in the $m_F = 0$ state for $\Omega \approx 0.3E_{\mathrm{L}}$. Finally, a cross-over to a helical spin texture occurs for large Ω, shown in Figure 5.6. The preference for $m_F = 0$ is seen in the single particle picture: for small Ω the degenerate $m_F = -1, 0, 1$ states split so that $m_F = 0$ becomes the lowest energy, as discussed in Section 5.2. The spin-current is initially suppressed by these FM interactions as seen in Figure 5.7. In the synthetic space, a FM state implies little phase change between neighboring sites with $m = 1$ or $m = -1$, leading to a suppressed spin current, but a SW is induced as a function of increasing Raman strength. This leads to an increased spin current, and even enhances it past the single particle value where density modulation is highest. Finally, the spin current approaches the non-interacting case.

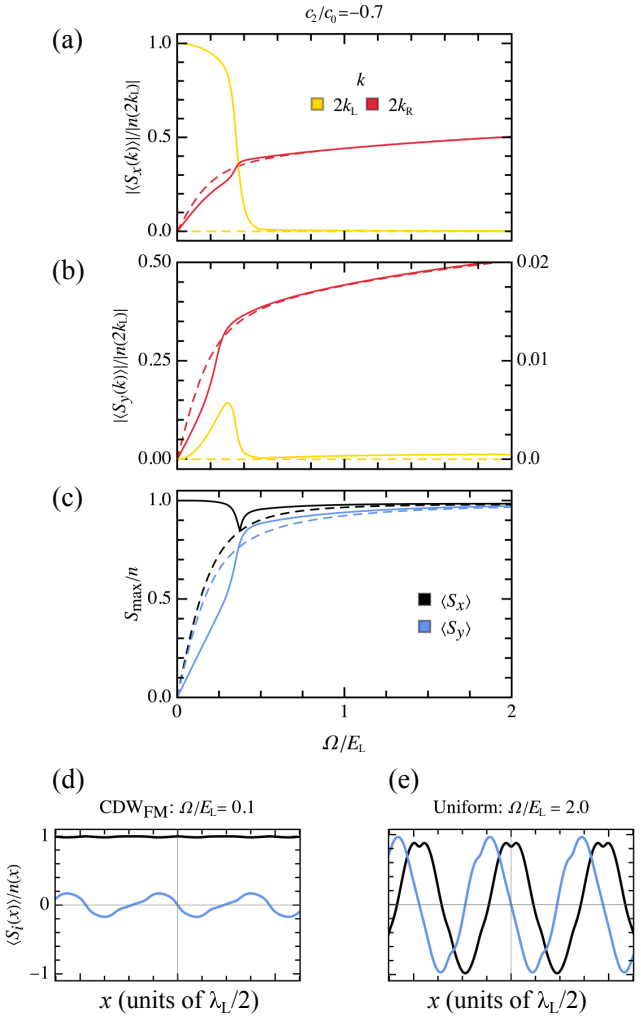

FIGURE 5.6: Spin wave order for $c_2/c_0 = -0.7$, $\varepsilon = 0$. Dashed lines show $c_2, c_0 = 0$ case for reference. (a) $\langle S_x(k)\rangle$ in the CDW$_{\mathrm{FM}}$ phase, shown by $|\langle S_x(2k_{\mathrm{L}})\rangle| \neq 0$ (yellow line). After the transition $\langle S_x\rangle$ is modulated primarily at the Raman wavevector $k = 2k_{\mathrm{R}}$ (red/dark gray line) and $|\langle S_x(2k_{\mathrm{L}})\rangle| \to 0$. (b) $\langle S_y(k)\rangle$ is nearly unaffected by the optical lattice but follows the Raman beam, shown by $|\langle S_y(2k_{\mathrm{L}})\rangle| \ll |\langle S_y(2k_{\mathrm{R}})\rangle|$. The right axis labels correspond to the yellow/light gray line. (c) Amplitude of spin oscillations with increasing Ω. S_x is indicated by the black line, S_y by the blue (light gray) line. The ferromagnetic state crosses over to Raman polarized at $\Omega \approx 0.5E_{\mathrm{L}}$. (d-e) Example real-space spin texture. (d) CDW$_{\mathrm{FM}}$ phase. (e) Uniform density phase with a helical spin texture. Legend is the same as in (c).

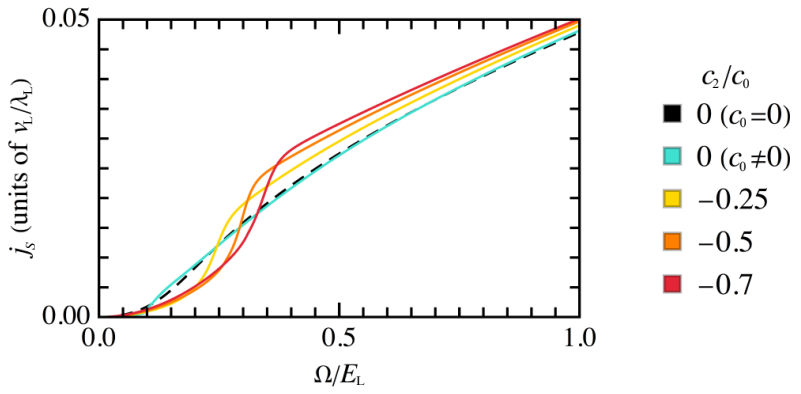

FIGURE 5.7: $j_S(\Omega)$ computed for $c_2/c_0 \leq 0$ and $\varepsilon = 0$. Ferromagnetic spin-dependent interactions first suppress and then slightly enhance the overall spin current compared to the non-interacting case (dashed line) in the regime where the density modulation is highest. For spin-independent interactions only ($c_2 = 0$ - cyan/ light gray line) the current is hardly changed.

5.3.2 Repulsive Spin-Dependent Interactions

In the case of polar interactions the system cannot lower its energy through the interplay of enhanced density modulation and spin wave order. Setting $\varepsilon = 0$ gives a uniform density ground state with $n(x) \sim \cos^2(k_L x)$. An experimentally accessible way to stabilize a CDW phase in a polar BEC is to bias the system with a large negative ε. Setting $\varepsilon = -E_L$ for $c_2 > 0$ favors occupation of the single-particle minima at maximal spin states. This induces competition between the spin-dependent interaction and the underlying single particle dispersion; in the language of synthetic dimensions, $\varepsilon < 0$ favors edge over bulk states.

The phase diagram for $c_2 - \Omega$ and $\varepsilon < 0$ is shown in Figure 5.2(b). There exist two phases with nonzero $n(2k_R)$ and $n(4k_R)$. These phases are denoted CDW_{SW1},

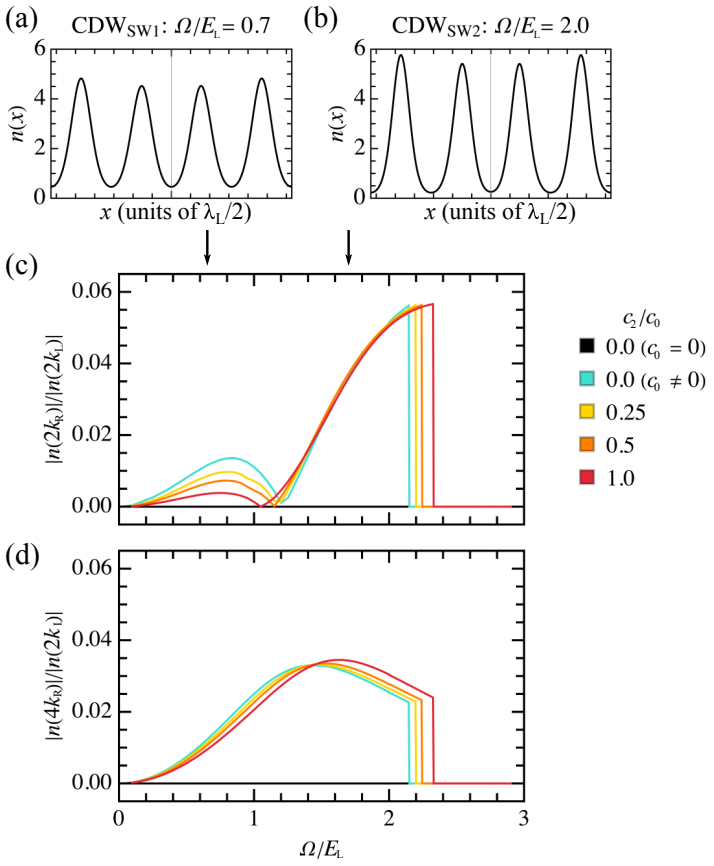

FIGURE 5.8: (a-b) GPE density computed for $c_2/c_0 = 0.25$ and $\varepsilon = -E_L$. (a) Density in real space in the CDW$_{SW1}$ and (b) CDW$_{SW2}$ phases. (c) $n(k)$ at $k = 2k_R$ and (d) $4k_R$. The non-interacting case (black line) has no density modulation other than by the lattice, so it is zero in this case. For $c_0 \neq 0$ the density is modulated at two different wavevectors of the same order of magnitude, varying slightly with varying c_2. For $|n(4k_R)| > |n(2k_R)|$ we denote the CDW$_{SW1}$ phase, while for $|n(4k_R)| < |n(2k_R)|$ the system is in the CDW$_{SW2}$ phase. The cross over from CDW$_{SW1}$ $\rightarrow$ CDW$_{SW2}$ occurs for $\Omega \approx 1.7E_L$. The system undergoes a first order transition to uniform density for $\Omega \approx 2.4E_L$, corresponding to the transition to the single minimum regime. This first order transition occurs at slightly higher Ω for increasing interaction strength. The red/darker gray line indicates largest interaction strength tested.

for $|n(4k_{\mathrm{R}})| > |n(2k_{\mathrm{R}})|$, and $\mathrm{CDW}_{\mathrm{SW2}}$ for $|n(4k_{\mathrm{R}})| < |n(2k_{\mathrm{R}})|$, which are analogous to the distinct density modulated phases found without the optical lattice in Ref. [142]. The existence of multiple density wave phases allows for the possibility of observing a continuous $\mathrm{CDW}_{\mathrm{SW1}} \rightarrow \mathrm{CDW}_{\mathrm{SW2}}$ cross over with increasing Ω, as shown in Figure 5.8(a-c). For $c_2/c_0 = 0.25, 0.5$ and 1.0, the cross over occurs at $\Omega \approx 1.7E_{\mathrm{L}}$. We find a first order phase transition at $\Omega \approx 2.4E_{\mathrm{L}}$ into the uniform density phase, which occurs when the lowest band becomes extremely flat (not shown). The first order transition is a generic feature of the transition from two minima to one and has also been predicted for the interacting system without the optical lattice [140, 142].

Even for the relatively shallow lattice at $V = 5E_{\mathrm{L}}$ contrast of the CDW phases may be difficult to resolve in experiments. The first order transition can be verified through measurement of the current, shown in Figure 5.9. Spin current is suppressed for $c_2 > 0$ in comparison to the non-interacting case, particularly in the flat-band region around $\Omega \approx 2.0E_{\mathrm{L}}$. The first order transition leads to a discontinuous jump in spin current. Past this point the spin current approaches the single particle case.

In addition to novel CDW behavior, the system exhibits multiple spin textures. Total spin $\langle \mathbf{S}^2(x) \rangle$ is minimized for $\Omega = 0$. As Ω grows the spin begins to polarize in the $S_x - S_y$ plane. Initially $\langle S_y \rangle$ is suppressed and only begins to grow after the $\mathrm{CDW}_{\mathrm{SW1}} \rightarrow \mathrm{CDW}_{\mathrm{SW2}}$ cross over, as shown in Figure 5.10(b,c). This spin configuration is also connected to two other degenerate states through the transformation in Eq. (5.9), which we have verified numerically. The lattice plays a much smaller role in the spin textures than in the $c_2 < 0$ case as evidenced by a small but nonzero $|\langle S_{x,y}(2k_{\mathrm{L}}) \rangle|$. At large Ω the helical spin texture is again entirely determined by the Raman beam, decoupled from the density behavior and the sign of c_2. The variety of spin textures is shown in Figure 5.10(d,e), where

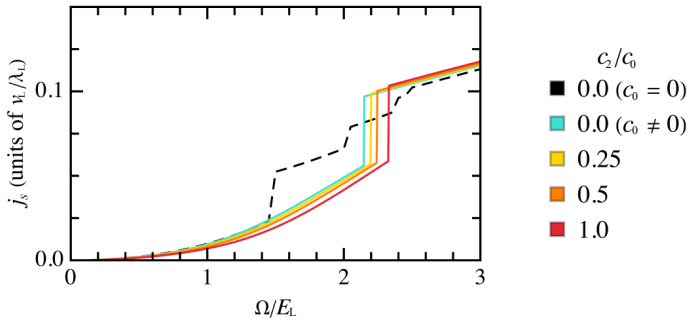

FIGURE 5.9: $j_S(\Omega)$ computed for $c_2/c_0 \geq 0$ and $\varepsilon = -E_{\mathrm{L}}$. Repulsive spin-independent (c_0) interactions suppress current compared to the non-interacting case, indicated by the dashed black line. The first order transition causes a sharp increase in current, and is weakly dependent on c_2. It occurs at higher values of Ω for higher values of c_2/c_0. The red/darker gray line indicates largest interaction strength tested. In the non-interacting case (dashed line), the discrete steps in the current are a finite size effect due to the change in curvature of the lowest band. As ε is tuned, the momentum k where the band minimum occurs decreases in discrete steps from the original value of $k = \pm 2k_{\mathrm{R}}$ until the single minimum regime at $k = 0$ is reached. In the infinite system this curve would be smooth.

we plot the spin in real space for each of the density wave phases. In the uniform density phase the spin texture is the same as Figure 5.6(e). Due to the high degree of degeneracy in the non-interacting case with $\varepsilon = -E_{\mathrm{L}}$, in Figure 5.8-5.9 we present the non-interacting results for condensation in a single minimum.

5.3.3 Effect of Increasing Lattice Depth

In this section we analyze the role of increasing lattice depth V_{L} on the CDW phases presented in the main body of the paper. The mean-field description of the BEC breaks down as the lattice depth increases and Mott physics becomes more important. In our results, we find that for both polar and ferromagnetic

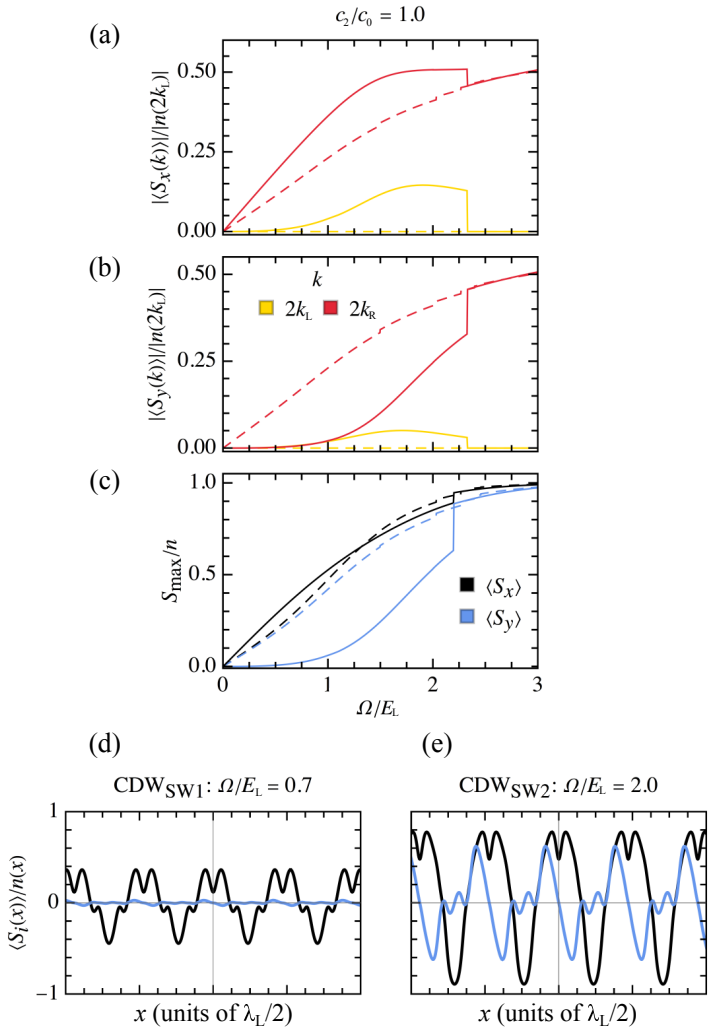

FIGURE 5.10: Spin wave order for $c_2/c_0 = 1.0$, $\varepsilon = -E_L$. Dashed lines show the $c_2, c_0 = 0$ case. (a-b) $\langle S_x(k)\rangle$ and $\langle S_y(k)\rangle$ are modulated at both the Raman and lattice wavevectors for $\Omega \lesssim 2.4E_L$. After the first order transition the spin comes unpinned from the lattice as evidenced by $|\langle S_{x,y}(k = 2k_L)\rangle| = 0$ (yellow/light gray lines) (c) The amplitude of spin oscillations grows with increasing Ω. S_x is indicated by the black line, S_y by the blue (light gray) line. The non-interacting case initially occupies a single minimum and is polarized in $\langle S_z\rangle$ for $\Omega = 0$ (not shown). For $\Omega \neq 0$ $\langle S_x\rangle$ and $\langle S_y\rangle$ grow continuously, with $\langle S_y\rangle$ suppressed in the interacting case. (d-e) Real-space spin textures for CDW$_{SW1}$ and CDW$_{SW2}$. Legend is the same as in (c).

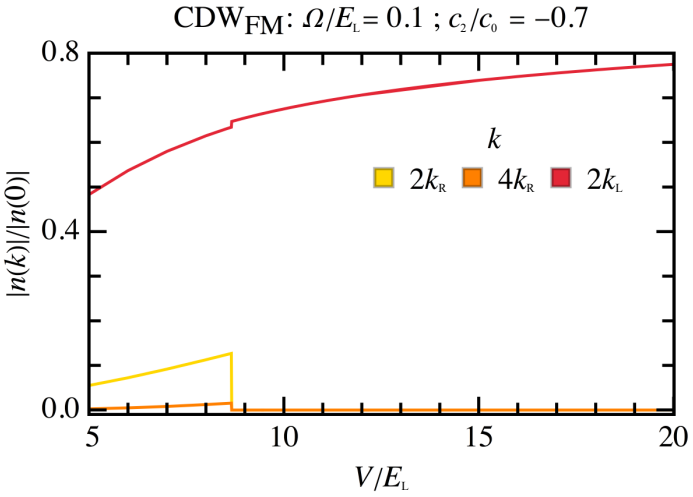

FIGURE 5.11: Dependence of the CDW_{FM} phase on lattice depth. As V_{L} increases, the CDW increases in amplitude and then undergoes a first order transition to a uniform density phase. Condensation moves toward the Brillouin zone edge, as shown by increasing $|n(2k_{\text{L}})|$ (red/darker gray line) even after the transition. Note that here $|n(k)|$ is normalized by $|n(k=0)|$.

spin-dependent interactions the CDW order is suppressed for $V_{\text{L}} \gtrsim 10E_{\text{L}}$. This indicates that increasing the lattice depth by as little as a factor of two reaches the boundary of applicability of the mean-field description in 1D.

In Figure 5.11 we analyze the effect of an increasing lattice depth on the CDW_{FM} phase. As V_{L} increases, the CDW amplitude *grows* until there is a first-order transition to a uniform density phase with modulation only at $k = 2k_{\text{L}}$. The transition occurs for $V_c \approx 8.6E_{\text{L}}$, therefore it is important that the system is in a relatively shallow lattice regime to observe the CDW_{FM} phase. For $V_{\text{L}} > V_c$, condensation only occurs at $k = 0$ and the Brillouin zone edge ($k = k_L$) with increasing lattice depth, as shown by an increase in $|n(2k_{\text{L}})|$ with increasing V_{L}. The deep lattice suppresses interaction-induced effects at the mean-field level (for these values of c_0 and c_2) including the CDW and FM polarization, and the spin

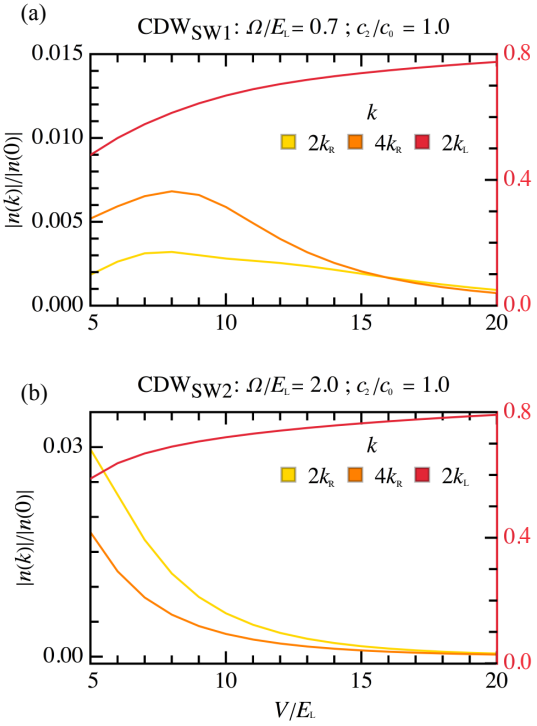

FIGURE 5.12: (a-b) Dependence of the CDW_{SW1} and CDW_{SW2} phases on lattice depth. In both cases, condensation moves toward the Brillouin zone edge, as shown by increasing $|n(2k_{\text{L}})|$ (red/darker gray top line, right axis), which is much larger in magnitude than the other order parameters. (a) CDW_{SW1}. As V_{L} increases, the CDW increases slightly before decreasing. (b) CDW_{SW2}. As V_{L} increases, the CDW decreases. Notably, $|n(2k_{\text{L}})|$ is the same order of magnitude as the CDW_{FM} case, while $|n(2k_{\text{R}})|$ (yellow/light gray line) and $|n(4k_{\text{R}})|$ (orange/gray line) are much smaller. Note that in both (a) and (b) $|n(k)|$ is normalized by $|n(k=0)|$.

texture is Raman-polarized as the lattice depth increases.

The effect of increasing lattice depth on both CDW_{SW1} and CDW_{SW2} is shown in Figure 5.12. Unlike the CDW_{FM} case, the amplitude of density modulations decreases gradually with increasing V_{L} and we do not find a sharp transition. For CDW_{SW1} the behavior of $n(k)$ at $k = 2k_{\text{R}}$ and $4k_{\text{R}}$ is slightly non-monotonic, showing a small increase initially with increasing V_{L}. In the case of CDW_{SW2}, $n(k)$

decreases across the entire range of V_{L}. Condensation at the lattice wavevector is almost the same as for the $\mathrm{CDW_{FM}}$ case, with $n(2k_{\mathrm{L}})$ having a similar magnitude. This shows that for increasing lattice depth the condensation wavevector moves to the edge of the Brillouin zone independent of the type of interactions present.

5.4 Conclusions

We examined the weakly interacting spin-1 Bose gas with SOC in an optical lattice and related it to the synthetic dimensions framework. Specifically, we have presented the phase diagram in the $\Omega - c_2$ plane for both positive and negative values of c_2. The system exhibits a rich phase diagram with CDW and SW phases, which depend strongly on Ω, ε, and the sign of c_2. In the regime of intermediate lattice depth at $V = 5E_{\mathrm{L}}$, we find a number of novel phases. For attractive spin-dependent interactions, the system exhibits ferromagnetic behavior and density modulations at the Raman wavevector, leading to altered spin current in the $\mathrm{CDW_{FM}}$ regime. In the $\mathrm{CDW_{FM}}$ phase there are small spin modulations that cross over to helical polarization.

BECs with repulsive spin-dependent interactions present novel phases provided that $\varepsilon < 0$. In particular, a cross over from a $\mathrm{CDW_{SW1}}$ to $\mathrm{CDW_{SW2}}$ phase occurs with increasing the Raman intensity, and a first order transition to a uniform density state is also seen. This first order transition can be measured through the spin current, which shows a discontinuous jump at the transition. We show that ε plays a crucial role in the phases that can be realized. Increasing Ω leads to condensation only at the lattice wavevector, which indicates a uniform density state. Additionally, we investigated the effect of increasing lattice depth and showed that as the lattice depth increases the amplitude of density modulations

gradually decreases. In effect, increasing the lattice depth washes out interaction-induced effects at the mean field level.

Finally, we studied the interplay of spin and density order parameters by characterizing the spin textures in the $S_x - S_y$ plane. Notably, the interplay of interactions and single particle physics at low Ω leads to alterations of the spin current and spin texture when compared to the non-interacting case. This is true of both attractive and repulsive c_2, however for $c_2 < 0$ this effect is particularly pronounced due to the appearance of finite magnetization. Interactions lead to modified bulk or edge occupation of the system in the synthetic dimension. For $c_2 > 0$ and large negative ε the system favors edge occupation of the synthetic lattice, while for $c_2 < 0$, $\varepsilon = 0$ it is primarily bulk occupation. Future research could investigate the excitation spectrum in the present setup, or more closely examine the role of ε. These results are accessible by current experiments and apply to a variety of atoms such as ^{87}Rb, ^{7}Li, ^{41}K, and ^{23}Na.

Chapter 6: Conclusion

In this dissertation we examined the role of topological defects in solid-state and cold atom systems and studied their dynamics when embedded in quantum systems. The defects considered here are treated semi-classically, but they interact with quantum particles via various mechanisms including quantum scattering and magnetic confinement. In Chapter 1 we reviewed the theory of defects in ordered media and showed that topological defects have different homotopy classifications than uniform or trivial field configurations, which is why they are so stable. Homotopy theory provides justification for our assumption that the defects themselves behave semi-classically even though they interact with external quantum degrees of freedom.

The problems considered here are at the boundary of classical and quantum physics and occur in many natural settings. In each Chapter we have used different analytical and numerical techniques to understand this phenomena including scattering theory, kinetic theory of stochastic processes, and diagrammatic perturbation theory. As researchers continue to work toward high-quality mesoscopic quantum systems it is important to develop an understanding of how topological defects affect transport phenomena, whether the defects are purposefully engineered or spontaneously occurring.

In Chapter 2 and Chapter 3 we considered topological defects in solid-state systems. We theoretically modeled skyrmions and magnetic vortices at the interface between a thin-film magnet and a 3D topological insulator (TI). The surface states of a 3D TI exhibit strong spin-momentum locking, therefore magnetic perturbations affect the electronic properties of these materials. We showed that

magnetic topological defects markedly alter the linear energy spectrum of the TI near the Dirac point. In particular, magnetic skyrmions can host discrete, in-gap states at the skyrmion radius due to the out-of-plane magnetic moments of the skyrmion, which open a gap in the TI spectrum everywhere except the skyrmion radius. Furthermore, we showed that these states are robust in the presence of an external magnetic field and could be observed in an experiment. The magnetically confined surface states cause the skyrmion to become charged, opening the door to skyrmion driving with only an electric field. Our proposal was the first for all-electric skyrmion driving.

In contrast to the skyrmion case, in Chapter 3 we considered a TI coupled to an XY model where all magnetic moments are in-plane. Although an in-plane magnetic field cannot open a gap in the energy spectrum, quasi long-range magnetic correlations due to 2D vortices can cause the surface state resistivity to increase. We showed that the magnetic vortices act like a random magnetic field (RMF) when coupled to Dirac fermions. The effective RMF causes a peak in resistivity near the vortex-unbinding transition temperature. Furthermore, for a strictly linear Dirac spectrum the coupling to the RMF is completely unscreened and leads to an infrared divergence in the quasiparticle decay time. The theory is regularized by accounting for band curvature due to electron-hole asymmetry or other material imperfections. This work presents a relevant effect in topological heterostructures and shows the limits of using TI surface states as a test-bed for gauge theories of Dirac fermions in free space.

In Chapter 4 we transitioned to cold atom systems and studied dark solitons in quasi-1D Bose-Einstein condensates (BEC). Dark solitons in higher dimensions decay into solitonic vortices or vortex pairs, thus they are related to the topological defects occuring in quasi-2D BECs and are characterized by phase winding

like their 2D vortex counterparts. In the case of repulsive interactions, dark solitons are an exact solution of the 1D Gross-Pitaevskii equation which describes the condensate at the mean-field level, an accurate description for most experiments.

We studied the dynamics of dark solitons in the presence of friction due to quantum impurities which scatter off of the soliton. Dark solitons are particularly interesting because they are heavy, particle-like density depressions that behave classically, but with a negative effective mass. As a consequence of the negative mass, friction causes the soliton to speed up and eventually decay. By solving the Fokker-Planck equation exactly for the probability distribution function of the soliton, we showed that the soliton cannot undergo Brownian motion in free space. However, in the presence of a harmonic trap Brownian motion is *emergent*. This is unlike any typical system undergoing Brownian motion. We proposed a Bose-Fermi mixture with a BEC and thermal impurity cloud as a test system and furthermore showed that the amount of friction in the system can be tuned by tuning the inter-particle interaction strengths. We also presented calculations for a similar model with bosonic scatterers which was implemented in an experiment and accurately predicted the diffusion coefficient for a dark soliton in an elongated ^{87}Rb BEC.

Finally, in Chapter 5 we explored a quasi-1D spin-1 BEC in an optical lattice with spin-orbit coupling (SOC). This model can be mapped on to a 2D square lattice where the internal spin states form a discrete synthetic dimension. For a specific form of the SOC each lattice plaquette has a uniform flux set by the ratio of Raman beam momentum and lattice momentum; this is a classic model for the Quantum Hall Effect (QHE). In the non-interacting case this system shows some signatures of the QHE including edge transport. We numerically showed that in the presence of interactions, density and spin-density waves occur as the ground state and can suppress or enhance the edge current based on the sign of

spin-dependent interactions. This provides evidence for interesting ground states to emerge in a synthetic dimensions experiment with interactions.

Appendix A: Gauge Transformation of In-Plane Magnetization

Although there are many ways to describe skyrmion textures, one simple and useful ansatz for the magnetization vector $\hat{\mathbf{n}}(r,\varphi)$ is [17]

$$\hat{\mathbf{n}}(r,\varphi) = \frac{2R_{\mathrm{S}}r}{r^2+R_{\mathrm{S}}^2}(-\sin\varphi\hat{x}+\cos\varphi\hat{y}) + \frac{r^2-R_{\mathrm{S}}^2}{r^2+R_{\mathrm{S}}^2}\hat{z} \tag{A.1}$$

Where R_{S} is the radius of the skyrmion. The in-plane magnetization in this case is a vortex, and it is symmetric under rotations. This is more apparent when we rewrite the in plane magnetization in polar coordinates,

$$n_{\varphi}(r)\hat{\varphi} = \frac{2R_{\mathrm{S}}r}{r^2+R_{\mathrm{S}}^2}\hat{\varphi}.$$

Now, we can separate the in-plane and out-of-plane magnetization in the Hamiltonian, where $\boldsymbol{\sigma} = (\sigma^x, \sigma^y)$.

$$\mathcal{H} = v_{\mathrm{F}}\left[\mathbf{p}\times\boldsymbol{\sigma}\right]\cdot\hat{z} + \Delta_{\mathrm{S}}n_{\varphi}(r)\hat{\varphi}\cdot\boldsymbol{\sigma} + \Delta_{\mathrm{S}}n_z(r)\hat{z}\cdot\sigma^z \tag{A.2}$$

using $\hat{\varphi} = \hat{z}\times\hat{r}$ and vector identities we rewrite $\mathcal{H}$

$$\mathcal{H} = \left[(v_{\mathrm{F}}\mathbf{p} + \Delta_{\mathrm{S}}n_{\varphi}(r)\hat{r})\times\boldsymbol{\sigma}\right]\cdot\hat{z} + \Delta_{\mathrm{S}}n_z(r)\hat{z}\cdot\sigma^z \tag{A.3}$$

Where $\mathcal{H}\psi = \epsilon\psi$. Introducing a gauge transformation $\psi \to e^{if(r,\varphi)}\psi'$ with a scalar function $f(r,\varphi)$, we can rewrite the time-independent Schrödinger equation as

$\mathcal{H}'\psi' = \epsilon\psi'$, where

$$\mathcal{H}' = [(v_{\mathrm{F}}\mathbf{p} + v_{\mathrm{F}}\hbar\nabla f(r,\varphi) + \Delta_{\mathrm{S}} n_{\varphi}(r)\hat{r}) \times \boldsymbol{\sigma}] \cdot \hat{z} + \Delta_{\mathrm{S}} n_z(r)\hat{z} \cdot \sigma^z \tag{A.4}$$

We can then find a scalar function $f(r,\varphi)$ for the skyrmion texture given in Equation (A.1) such that $v_{\mathrm{F}}\hbar\nabla f(r,\varphi) + \Delta_{\mathrm{S}} n_{\varphi}(r)\hat{r} = 0$. If this equation has a solution for the skyrmion ansatz, we are able to"gauge away" the in-plane magnetic texture. In this way we see that the in plane texture will not change the energy spectrum of the bound Dirac fermions. Most importantly, the in-plane magnetization will not open up a gap in the spectrum. The scalar function $f(r,\varphi)$ should be independent of φ since the magnetic texture is rotationally invariant. In polar coordinates we have

$$\nabla f(r,\varphi) = \frac{\partial f(r,\varphi)}{\partial r}\hat{r} + \frac{1}{r}\frac{\partial f(r,\varphi)}{\partial \varphi}\hat{\varphi} = -\frac{\Delta_{\mathrm{S}}}{v_{\mathrm{F}}\hbar} n_{\varphi}(r)\hat{r}$$

$$f(r) = -\frac{\Delta_{\mathrm{S}} R_{\mathrm{S}}}{v_{\mathrm{F}}\hbar}\int_0^r dr \frac{2r}{r^2 + R_{\mathrm{S}}^2} = -\frac{\Delta_{\mathrm{S}} R_{\mathrm{S}}}{v_{\mathrm{F}}\hbar}\log\left(\frac{r^2 + R_{\mathrm{S}}^2}{R_{\mathrm{S}}^2}\right) \tag{A.5}$$

Appendix B: Low-T XY-Model Correlation Functions

B.1 Free Energy

For the low-temperature correlation functions we can use the continuum approximation of the free energy $F = \frac{1}{2}\int d\mathbf{r}\rho_s(\nabla\Theta(\mathbf{r}))^2$ where ρ_s is the spring constant or "spin stiffness" and $\Theta(\mathbf{r})$ is the phase of the magnetic moments $\mathbf{n}(\mathbf{r}) = (\cos\Theta(\mathbf{r}), \sin\Theta(\mathbf{r}))$. The Fourier transform of F is found using $\Theta(\mathbf{r}) = \sum_k \Theta_k e^{i\mathbf{k}\cdot\mathbf{r}}$.

$$F = \frac{\rho_s}{2}\int d\mathbf{r}\sum_{kk'} ikik'\Theta_k\Theta_{k'}e^{ikr+ik'r} = \frac{\rho_s}{2}\sum_k k^2\Theta_k\Theta_{-k} \tag{B.1}$$

Where the integral over $d\mathbf{r}$ gives the relation $k' = -k$. Furthermore, the field $\Theta(\mathbf{r})$ is real, giving $\Theta_{-k} = \Theta_k^*$. Since Θ_k is a complex quantity we need only sum over *positive* values of k to account for this redundancy. We denote the sum over k for $k > 0$ as $\sum_k'$. Using this, we have

$$F = \frac{\rho_s}{2}\sum_k k^2\Theta_k\Theta_{-k} = \frac{\rho_s}{2}\sum_k{}' 2k^2|\Theta_k|^2 = \sum_k{}' \varepsilon_k|\Theta_k|^2 \quad ; \quad \varepsilon_k = \rho_s k^2$$

Now we have a free energy that is diagonal in momentum space and quadratic in the field Θ_k.

B.2 Spin-Spin Correlation Functions

To calculate the correlation functions of the spin components we calculate quantities like $\left\langle e^{i\{\Theta(\mathbf{r}_1)+\Theta(\mathbf{r}_2)\}}\right\rangle$ and $\left\langle e^{i\{\Theta(\mathbf{r}_1)-\Theta(\mathbf{r}_2)\}}\right\rangle$. We define them in k-space as

$$e^{i\{\Theta(\mathbf{r}_1)+\Theta(\mathbf{r}_2)\}} = e^{i\sum_k \Theta_k(e^{ikr_1}+e^{ikr_2})} = e^{i\sum_k \Theta_k c_{1,k}}$$
$$e^{i\{\Theta(r_1)-\Theta(r_2)\}} = e^{i\sum_k \Theta_k(e^{ikr_1}-e^{ikr_2})} = e^{i\sum_k \Theta_k c_{2,k}}$$

Now we have

$$e^{i\sum_k \Theta_k c_k} = e^{i\sum_k' \Theta_k c_k + i\sum_k' \Theta_{-k} c_{-k}} = e^{i\sum_k' \Theta_k c_k + i\sum_k' \Theta_k^* c_k^*}$$

The gaussian integration over the Θ_k fields is the straightforward if we split Θ_k into real and imaginary parts. This gives:

$$i\sum_k{}' \Theta_k c_k + i\sum_k{}' \Theta_k^* c_k^* = i\sum{}' \Theta_k^R(c_k + c_k^*) + i\Theta_k^I(c_k - c_k^*) = 2i\sum_k{}' \Theta^R c_k^R - \Theta_k^I c_k^I$$

Now we can calculate the correlators:

$$\left\langle e^{i\{\Theta(r_1)\pm\Theta(r_2)\}}\right\rangle = \frac{\int \mathcal{D}\Theta_k^R \mathcal{D}\Theta_k^I e^{2i\sum_k' \Theta^R c_k^R - \Theta_k^I c_k^I} e^{-\beta\sum_k' \varepsilon_k(\Theta_k^R)^2 + (\Theta_k^I)^2}}{\int \mathcal{D}\Theta_k^R \mathcal{D}\Theta_k^I e^{-\beta\sum_k' \varepsilon_k(\Theta_k^R)^2 + (\Theta_k^I)^2}}$$

Both the real and imaginary integrals are now of the form $\int dx\, e^{-ax^2-2bx} = \sqrt{\frac{\pi}{a}}\, e^{\frac{b^2}{a}}$, so we have

$$\left\langle e^{i\{\Theta(r_1)\pm\Theta(r_2)\}}\right\rangle = \prod_k{}' e^{-\sum_k' \frac{\left(c_k^R\right)^2}{\beta\varepsilon_k}} e^{-\sum_k' \frac{\left(c_k^I\right)^2}{\beta\varepsilon_k}} = \prod_k{}' e^{-\sum_k' \frac{|c_k|^2}{\beta\varepsilon_k}} = e^{-I}$$

The functions c_k are now different depending on $\Theta(r_1) \pm \Theta(r_2)$ where $I_1 = (+)$ and $I_2 = (-)$.

$$|c_{1,k}|^2 = (e^{ikr_1} + e^{ikr_2})(e^{-ikr_1} + e^{-ikr_2}) = 2 + 2\cos[\mathbf{k}\cdot\mathbf{r}]$$
$$|c_{2,k}|^2 = (e^{ikr_1} - e^{ikr_2})(e^{-ikr_1} - e^{-ikr_2}) = 2 - 2\cos[\mathbf{k}\cdot\mathbf{r}]$$

Where $\mathbf{r} = \mathbf{r}_1 - \mathbf{r}_2$.

$$I_1 = \frac{2}{\beta\rho_s}\int \frac{d^2k}{(2\pi)^2}\frac{1+\cos(kr\cos\theta)}{k^2} \;\; ; \;\; I_2 = \frac{2}{\beta\rho_s}\int \frac{d^2k}{(2\pi)^2}\frac{1-\cos(kr\cos\theta)}{k^2}$$

To solve these we will need the formula $\cos(\alpha\cos\theta) = \sum_m e^{im\theta}J_m(\alpha)$, where $J_m(\alpha)$ is a Bessel function of the first kind.

$$I_1(\mathbf{r}) = \frac{1}{2\pi\beta\rho_s}\int_0^\infty \frac{dk}{k}\left[1 + J_0(kr)\right] \tag{B.2}$$
$$I_2(\mathbf{r}) = \frac{1}{2\pi\beta\rho_s}\int_0^\infty \frac{dk}{k}\left[1 - J_0(kr)\right] \tag{B.3}$$

Looking at $I_1(\mathbf{r})$, we see that the integral diverges as $k \to 0$ and $k \to \infty$. The infrared divergence as $k \to 0$ implies that the overall quantity $\left\langle e^{i(\Theta_1+\Theta_2)}\right\rangle$ is killed off by long range phase fluctuations. Therefore, we can safely say that $\left\langle e^{\pm i(\Theta_1+\Theta_2)}\right\rangle = 0$. $I_2(\mathbf{r})$ is well-behaved at the origin but diverges logarithmically as $k \to \infty$. This is because for small arguments $J_0(k\mathbf{r})$ approaches 1, so the infrared divergence at the origin is removed. To deal with the logarithmic divergence, we introduce a length scale a such that $k_{\max} \sim a^{-1}$. a is the smallest length scale that can be described by the continuum theory, analogous to a lattice constant. Therefore, we have

$$I_2(\mathbf{r}) = \frac{1}{2\pi\beta\rho_s}\int_0^{r/a}\frac{dx}{x}\left[1 - J_0(x)\right] \sim \frac{1}{2\pi\beta\rho_s}\ln\frac{r}{a} \;\; ; \;\; \frac{r}{a} \gg 1$$

Finally, we have

$$\left\langle e^{i\{\Theta(r_1)-\Theta(r_2)\}}\right\rangle = e^{-I_2(\mathbf{r})} = \left(\frac{r}{a}\right)^{-\frac{1}{2\pi\beta\rho_s}} \tag{B.4}$$

From this general expression we can calculate

$$\begin{aligned}\langle n_x n_x\rangle &= |n|^2 \langle \cos\Theta(r_1)\cos\Theta(r_2)\rangle \\ &= \frac{1}{4}\left[\left\langle e^{i\{\Theta(r_1)+\Theta(r_2)\}}\right\rangle + \left\langle e^{-i\{\Theta(r_1)+\Theta(r_2)\}}\right\rangle + \left\langle e^{i\{\Theta(r_1)-\Theta(r_2)\}}\right\rangle + \left\langle e^{-i\{\Theta(r_1)-\Theta(r_2)\}}\right\rangle\right] \\ &= \frac{1}{2}\left(\frac{r}{a}\right)^{-\frac{1}{2\pi\beta\rho_s}} = \frac{1}{2}\langle \mathbf{n}\cdot\mathbf{n}\rangle \end{aligned} \tag{B.5}$$

$$\begin{aligned}\langle n_y n_y\rangle &= |n|^2 \langle \sin\Theta(r_1)\sin\Theta(r_2)\rangle \\ &= \frac{1}{4(i^2)}\left[\left\langle e^{i\{\Theta(r_1)+\Theta(r_2)\}}\right\rangle + \left\langle e^{-i\{\Theta(r_1)+\Theta(r_2)\}}\right\rangle - \left\langle e^{i\{\Theta(r_1)-\Theta(r_2)\}}\right\rangle - \left\langle e^{-i\{\Theta(r_1)-\Theta(r_2)\}}\right\rangle\right] \\ &= \frac{1}{2}\left(\frac{r}{a}\right)^{-\frac{1}{2\pi\beta\rho_s}} = \frac{1}{2}\langle \mathbf{n}\cdot\mathbf{n}\rangle \end{aligned} \tag{B.6}$$

Therefore, we have quasi long range order in $\langle n_x n_x\rangle$ and $\langle n_y n_y\rangle$ because the correlations exhibit power law decay. Finally, we have

$$\begin{aligned}\langle n_x n_y\rangle &= |n|^2 \langle \cos\Theta(r_1)\sin\Theta(r_2)\rangle \\ &= \frac{1}{4}\left[\left\langle e^{i\{\Theta(r_1)+\Theta(r_2)\}}\right\rangle - \left\langle e^{-i\{\Theta(r_1)+\Theta(r_2)\}}\right\rangle - \left\langle e^{i\{\Theta(r_1)-\Theta(r_2)\}}\right\rangle + \left\langle e^{-i\{\Theta(r_1)-\Theta(r_2)\}}\right\rangle\right] \\ &= \frac{1}{4}\left[\left(\frac{r}{a}\right)^{-\frac{1}{2\pi\beta\rho_s}} - \left(\frac{r}{a}\right)^{-\frac{1}{2\pi\beta\rho_s}}\right] = 0 \end{aligned} \tag{B.7}$$

There are no correlations between n_x and n_y components.

Appendix C: Impurities Reflection Coefficient

We begin the analysis from Equation 4.11 in the main text for the impurity wave-function,

$$\frac{\partial^2\psi(z)}{\partial z^2} + \left[\frac{\lambda(\lambda-1)}{\cosh^2(z)} + k^2\right]\psi(z) = 0 \tag{C.1}$$

Where $z = \gamma_v z/\xi$ and

$$\lambda(\lambda-1) = \frac{2m_{\rm i}g'}{m_{\rm c}g}\ ;\ k^2 = \frac{4m_{\rm i}\xi^2}{\hbar^2\gamma_{\rm s}^2}\left(E + \frac{m_{\rm i}v_{\rm s}^2}{2} - g'n_{\rm c}\right). \tag{C.2}$$

The energy of $\psi(z)$ is shifted from the ususal Pöschl-Teller problem by $-g'n_c$ due to the transformation we made from $\tanh^2(z)$ to $\cosh^{-2}(z)$. It is also shifted by $mv^2/2$, which is just the additional kinetic energy imparted by being in the rest frame of a soliton moving at finite velocity v. In the following we work in the soliton rest frame where $v = 0$ ($\gamma_v = 1$). Equation (C.1) can be brought into hypergeometric form by defining the following transformations [111]

$$y = \frac{1+\tanh(z)}{2}\ \ ;\ \ \psi(y) = \left(\frac{1+y}{1-y}\right)^{ik/2} U(y) \tag{C.3}$$

The function $U(y)$ obeys the hypergeometric equation

$$y(1-y)\frac{\partial^2 U}{\partial y^2} + (ik - 2y + 1)\frac{\partial U}{\partial y} + \lambda(\lambda-1)U(y) = 0 \tag{C.4}$$

with two solutions ${}_2F_1(a,b,c;y)$ and $y^{1-c}\ {}_2F_1(a-c+1,b-c+1,2-c;y)$ [150]. Restoring the original variables, the most general solution for $\psi(z)$ is

$$\psi(z) = Ae^{ikz}\ {}_2F_1\left(\lambda, 1-\lambda, ik+1; \frac{1+\tanh(z)}{2}\right) + \\ + B\left(2+e^{-2z}+e^{2z}\right)^{ik/2}\ {}_2F_1\left(\lambda-ik, 1-\lambda-ik, 1-ik; \frac{1+\tanh(z)}{2}\right) \tag{C.5}$$

Where A and B are general coefficients. The asymptotic form of $\psi(z)$ as $z \to \pm\infty$ allows us to determine the form of the scattering matrix, and thus the reflection and transmission amplitudes. As $z \to \pm\infty$, $\tanh(z) \to \pm 1$ and the argument of the hypergeometric functions goes to 1 or 0. Given that ${}_2F_1(a,b,c;0) = 1$, we can first easily find the limit as $z \to -\infty$:

$$\psi^-(z) = \lim_{z\to-\infty} \psi(z) = Ae^{ikz} + Be^{-ikz} \tag{C.6}$$

In the limit $z \to \infty$, the argument of the hypergeometric function approaches 1, but care must be taken with this limit. We first use the following property of hypergeometric functions [150]

$${}_2F_1\left(a,b,c;u\right) = \frac{\Gamma(c)\Gamma(c-a-b)}{\Gamma(c-a)\Gamma(c-b)}\ {}_2F_1\left(a,b,a+b-c+1,1-u\right) \\ + (1-u)^{c-a-b}\frac{\Gamma(c)\Gamma(a+b-c)}{\Gamma(a)\Gamma(b)}\ {}_2F_1\left(c-a,c-b,c-a-b+1,1-u\right) \tag{C.7}$$

We start with

$$\psi^+(z) = \lim_{z\to+\infty} \psi(z) = Ae^{ikz}\ {}_2F_1\left(\lambda, 1-\lambda, ik+1; \frac{1+\tanh(z)}{2}\right) + \\ + Be^{ikz}\ {}_2F_1\left(\lambda-ik, 1-\lambda-ik, 1-ik; \frac{1+\tanh(z)}{2}\right) \tag{C.8}$$

In both A and B terms we have terms like

$$\lim_{z\to\infty} e^{ikz}\frac{e^{-ikz}}{(e^{-z}+e^{z})^{ik}} \approx e^{-ikz} \tag{C.9}$$

Finally, we end up with

$$\psi^{+}(z) = Ce^{ikz} + De^{-ikz} \tag{C.10}$$

with

$$C = \left[A\frac{\Gamma(ik+1)\Gamma(ik)}{\Gamma(ik+1-\lambda)\Gamma(ik+\lambda)} + B\frac{\Gamma(1-ik)\Gamma(ik)}{\Gamma(1-\lambda)\Gamma(\lambda)}\right]$$

$$D = \left[A\frac{\Gamma(1-ik)\Gamma(-ik)}{\Gamma(\lambda-ik)\Gamma(1-\lambda-ik)} + B\frac{\Gamma(1-ik)\Gamma(-ik)}{\Gamma(\lambda-ik)\Gamma(1-\lambda-ik)}\right]$$

The transfer matrix $\hat{T}$ is then defined by connecting the asymptotic wavefunctions at $\pm\infty$ as $\psi^{+}(z) = \hat{T}\psi^{-}(z)$.

$$\begin{pmatrix} C \\ D \end{pmatrix} = \hat{T}\begin{pmatrix} A \\ B \end{pmatrix} \tag{C.11}$$

Finally, we have the analytical form of the transfer matrix, simplified slightly to

$$\hat{T} = \begin{pmatrix} \frac{\Gamma(ik+1)\Gamma(ik)}{\Gamma(ik+1-\lambda)\Gamma(ik+\lambda)} & \frac{\Gamma(1-ik)\Gamma(ik)}{\Gamma(1-\lambda)\Gamma(\lambda)} \\ \\ \frac{\Gamma(ik+1)\Gamma(-ik)}{\Gamma(1-\lambda)\Gamma(\lambda)} & \frac{\Gamma(1-ik)\Gamma(-ik)}{\Gamma(\lambda-ik)\Gamma(1-\lambda-ik)} \end{pmatrix} \tag{C.12}$$

The scattering matrix $\hat{S}$ connects left and right moving states, and it is defined as

$$\begin{pmatrix} B \\ C \end{pmatrix} = \hat{S}\begin{pmatrix} A \\ D \end{pmatrix} \tag{C.13}$$

$\hat{S}$ can be found from the transfer matrix via the relation [151]

$$\hat{S} = \frac{1}{T_{22}} \begin{pmatrix} -T_{21} & 1 \\ T_{11}T_{22} - T_{21}T_{12} & T_{12} \end{pmatrix} \tag{C.14}$$

and finally, the transmission and reflection amplitudes are given by

$$r = S_{11} = \frac{\Gamma(\lambda - ik)\Gamma(1 - \lambda - ik)}{\Gamma(1 - \lambda)\Gamma(\lambda)} \tag{C.15}$$

$$t = S_{21} = \frac{\Gamma(\lambda - ik)\Gamma(1 - \lambda - ik)}{\Gamma(1 - ik)\Gamma(-ik)} \tag{C.16}$$

The reflection coefficient $R = |r|^2$ determines the transport coefficients of the soliton, because friction and diffusion comes from impurity states that are scattered from the soliton while those that are not scattered will not impart any momentum to the soliton. The reflection coefficient is

$$\begin{aligned} R(k, \lambda) &= \frac{\Gamma(\lambda - ik)\Gamma(\lambda + ik)\Gamma(1 - \lambda - ik)\Gamma(1 - \lambda + ik)}{\Gamma(1 - \lambda)^2\Gamma(\lambda)^2} \\ &= \frac{1 - \cos(2\pi\lambda)}{\cosh(2\pi k) - \cos(2\pi\lambda)} \end{aligned} \tag{C.17}$$

Appendix D: Chemical Potential of Fermions with Dark Soliton

The friction coefficient γ is highly sensitive to the reflection coefficient $R(k,\lambda)$ *and* the chemical potential of the fermionic atoms through the distribution function $n_{\rm F}(\epsilon_k)$ in equation (4.19). Although the number of fermions in the system is fixed, the chemical potential is sensitive to the bound states in the soliton well, the phase shift of the scattering states, and the density of states at the Fermi level. In this Appendix we present the full calculation of the chemical potential of 1D fermions in the presence of a dark soliton potential well. The same calculation was done for bosons for Section 4.7.

The total number of impurities is given by $N_{\rm i} = N_{\rm s}(\mu_{\rm i}) + N_{\rm b}(\mu_{\rm i}) + \delta N(\mu_{\rm i})$, where $N_{\rm s}$ indicates scattering (continuum) states, $N_{\rm b}$ indicates bound states, and δN is a correction due to the phase shift of scattering states. All three quantities are a function of the chemical potential $\mu_{\rm i}$. We can define the following equation for the 1D impurity density,

$$\frac{N_{\rm i}}{L} = -\sqrt{\frac{m_{\rm i}k_{\rm B}T}{2\pi\hbar^2}}\mathrm{Li}_{\frac{1}{2}}\left(-e^{\beta\mu_{\rm i}}\right) + \frac{2}{L}\sum_{j=0}^{\mathrm{floor}(\lambda-1)}\frac{1}{e^{\beta(\epsilon_j-\mu_{\rm i})}+1} + \frac{1}{L}\int\frac{dk}{2\pi}\frac{1}{e^{\beta(\epsilon_k-\mu_{\rm i})}+1}\frac{\partial\delta(k,\lambda)}{\partial k} \quad ; \quad \beta = \frac{1}{k_{\rm B}T} \tag{D.1}$$

The first term in equation (D.1) comes from integrating over k for the continuum states, where $\mathrm{Li}_{1/2}(x)$ is the polylogarithm function. The continuum dispersion is $\epsilon_k \propto \hbar^2k^2/2m_{\rm i}$. The second term accounts for the bound states, which have quantized energies $\epsilon_j = -\hbar^2/2m_{\rm i}\xi^2(\lambda-1-j)^2$ for integer $j < \lambda-1$. The factor of two accounts for Pauli degeneracy. Finally, the third term in equation (D.1) is a

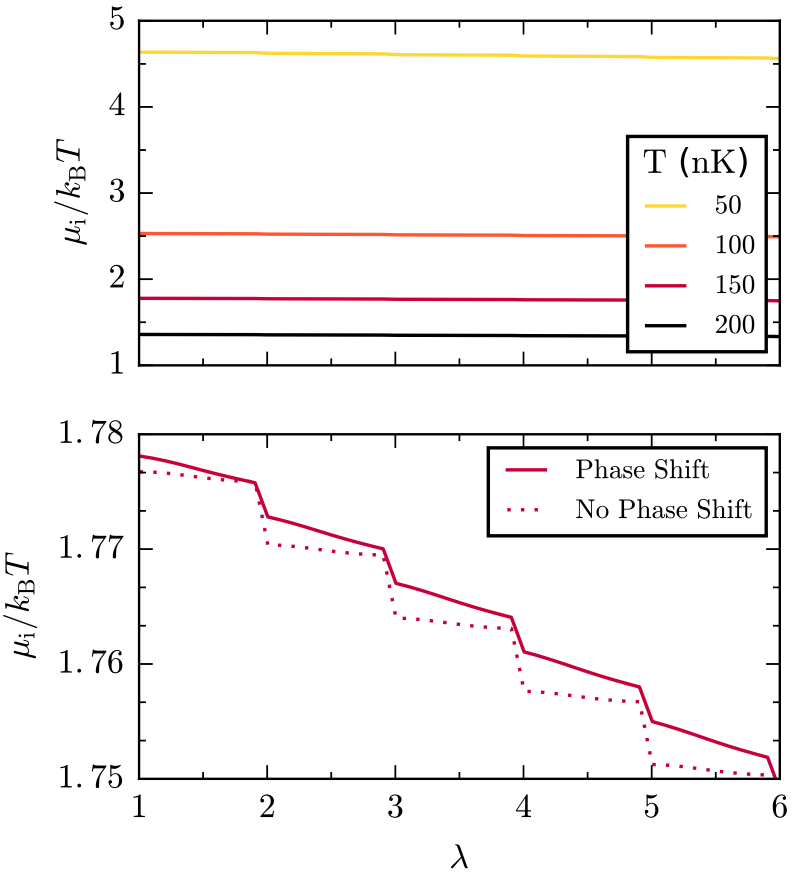

FIGURE D.1: Top: The chemical potential μ_i of fermionic impurities, from solving equation (D.1) numerically for $N_i = 1000$ ^{173}Yb atoms with $L = 250$ μm. μ_i decreases slightly as λ is increased and there are more bound states in the soliton well. Increasingly dark lines indicate higher temperatures. Bottom: Chemical potential for $T = 150$ nK. The steps at each integer indicate an additional bound state in the soliton well. The chemical potential including the phase shift (solid line) is increased slightly from the result without it (dotted line).

correction due to the phase shift of the scattering states. The phase shift is given by $\delta(k, \lambda) = \mathrm{Arg}\,[t(k, \lambda)]$ with the transmission amplitude from Equation (C.16)

$$t = \frac{\Gamma(\lambda - ik)\Gamma(1 - \lambda - ik)}{\Gamma(1 - ik)\Gamma(-ik)}. \tag{D.2}$$

The correction δN is proportional to $\partial_k \delta(k, \lambda)$, which takes the form

$$\frac{\partial \delta(k,\lambda)}{\partial k} = \mathrm{Re}\left[\psi^0(-ik) + \psi^0(1-ik) - \psi^0(\lambda - ik) - \psi^0(1-ik-\lambda)\right], \quad \text{(D.3)}$$

where $\psi^0(z) = \Gamma'(z)/\Gamma(z)$ is the digamma function. We solve for μ_i numerically for ^{173}Yb atoms with $N_\mathrm{i} = 1000$ and $L = 250$ μm for temperatures $T = \{50, 100, 150, 200\}$ nK.

The results of the calculation are shown in Figure D.1. The chemical potential of the fermion atoms decreases slightly as the interaction strengths are tuned and the soliton well becomes deeper, and we find $\mu_\mathrm{i} \approx k_\mathrm{B}T$ for all temperatures considered. In the bottom panel of Figure D.1 we show the result with and without accounting for the phase shift term. The phase shift of the scattering states slightly increases the chemical potential. These results are used in calculating γ in equation (4.19) and Fig. 4.2 of the main text.

Appendix E: Kinetic Theory Derivations

E.1 Collision Integral

The collision integral for a heavy object interacting with a gas of lighter objects can be derived in quite a general way, as has been done in many textbooks (e.g.[106, 152]). The essential assumption is that the momentum transferred in each collision is small. Treating the soliton as a heavy classical object, we assume that it has some probability distribution $f(t, x_{\rm s}, p)$ which depends on momentum p, time t, and position $x_{\rm s}$. Let $P(p,q)dq$ denote the probability per unit time of a change $p \to p-q$ in the momentum of the soliton in a collision with a fermionic impurity atom, where q is the momentum transferred. The transport equation for f is then given by

$$\frac{df}{dt} = \int dq\ P(p+q,q)f(t,p+q) - P(p,q)f(t,p) \tag{E.1}$$

which measures the difference between the soliton scattering into a state with momentum p and out of a state with momentum p. We assume that the transferred momentum in each collision is small, i.e. $q \ll p$ and that $P(p,q)$ is a smooth function. We then make the following expansion,

$$P(p+q,q)f(t,p+q) \approx P(p,q)f(t,p) + q\frac{\partial}{\partial p}\left(P(p,q)f(t,p)\right) + \frac{1}{2}q^2\frac{\partial^2}{\partial p \partial p}\left(P(p,q)f(t,p)\right) \tag{E.2}$$

This gives a transport equation for f with a collision integral in Fokker-Planck form

$$\frac{df}{dt} = \mathcal{I}[f] \quad ; \quad \mathcal{I}[f] = \frac{\partial}{\partial p}\left(A_p f + \frac{\partial}{\partial p}\left[B_p f\right]\right). \tag{E.3}$$

E.2 Transport Coefficients

The transport coefficients are given by

$$A_p = \sum_q qP(p,q) \;\; ; \;\; B_p = \frac{1}{2}\sum_q q^2 P(p,q), \tag{E.4}$$

where q is the momentum transferred between the heavy object and the light one in a single collision.

For the dark soliton we write the momentum $p = -Mv_\mathrm{s}$, giving the collision integral as a function of velocity

$$\mathcal{I}[f] = \frac{\partial}{\partial v_\mathrm{s}}\left(-\frac{A_p}{M}f + \frac{\partial}{\partial v_\mathrm{s}}\left[\frac{B_p}{M^2}f\right]\right) = \frac{\partial}{\partial v_\mathrm{s}}\left(-A_{v_\mathrm{s}}f + \frac{\partial}{\partial v_\mathrm{s}}\left[B_{v_\mathrm{s}}f\right]\right). \tag{E.5}$$

The transport coefficients presented in equation (4.17) and (4.18) of the main text are related to A_p and B_p as $A_{v_\mathrm{s}} = A_p/M$ and $B_{v_\mathrm{s}} = B_p/M^2$; we present the rest of the calculation in terms of v_s.

Coefficients A_{v_s} and B_{v_s} are not independent. When $f = \exp(-E(v_\mathrm{s})/k_\mathrm{B}T)$ is the Maxwell-Boltzmann distribution the collision integral $\mathcal{I}[f]$ must vanish. For the soliton, we have $f(E(v_\mathrm{s})) \approx \exp(Mv_\mathrm{s}^2/2k_\mathrm{B}T)$. Plugging this into $\mathcal{I}[f]$, we find the relation

$$\left(-A_{v_\mathrm{s}} + \frac{\partial B_{v_\mathrm{s}}}{\partial v_\mathrm{s}}\right)f + \frac{v_\mathrm{s}MB_{v_\mathrm{s}}}{k_\mathrm{B}T}f = 0. \tag{E.6}$$

To first order, $\partial_{v_\mathrm{s}} B_{v_\mathrm{s}} = 0$, giving

$$A_{v_\mathrm{s}} = \frac{Mv_\mathrm{s}B_{v_\mathrm{s}}}{k_\mathrm{B}T}. \tag{E.7}$$

We emphasize that this relation relies only on the condition that $f(E(v_\mathrm{s}))$ is Maxwell-Boltzmann and not on the microscopic properties of the scatterers, and

the microscopic expressions for A_{v_s} and B_{v_s} must satisfy this relation [106].

The probability per unit time that the heavy object will undergo a scattering event is $P(p,q) = R_q|v_q|\mathbf{s}(k,k_s)$, where R_q is the reflection coefficient, $|v_q|$ is the velocity and $\mathbf{s}(k,k_s)$ is a statistical factor which gives the occupation number of scatterers. In the case of bosonic impurities, $\mathbf{s}(k,k_s) = n_B(1+n_B)$, where n_B is the Bose-Einstein distribution. This term accounts for bosonic enhancement.

In the case of fermionic impurities, which we consider here, $\mathbf{s}(k,k_s) = n_F(1-n_F)$ where n_F is the Fermi-Dirac distribution. This term accounts for Pauli blocking, which means that a fermion with momentum k is unable to scatter into a state with momentum $-k$ if that state is already filled. An incoming particle with momentum $p_i = \hbar k$ is reflected with momentum $p_f = -\hbar k$, giving $q = p_f - p_i = -2\hbar k$. Now, we have the following expressions for A_{v_s} and B_{v_s}

$$A_{v_s} = -\frac{2\hbar}{M}\sum_k kR_{k,\lambda}\left|\frac{\partial\epsilon_k}{\hbar\partial k}\right| n_F(\epsilon_{k+k_s})\left[1-n_F(\epsilon_{-k+k_s})\right]. \tag{E.8}$$

$$B_{v_s} = \frac{2\hbar^2}{M^2}\sum_k k^2R_{k,\lambda}\left|\frac{\partial\epsilon_k}{\hbar\partial k}\right| n_F(\epsilon_{k+k_s})\left[1-n_F(\epsilon_{-k+k_s})\right]. \tag{E.9}$$

Given these relations, we can check that equation (E.7) is satisfied to first order in $k_s = m_i v_s/\hbar$. The Fermi-Dirac distribution can be expanded as

$$n_F(\epsilon_{\pm k+k_s}) \approx n_F(\epsilon_{\pm k}) \pm \hbar k v_s \frac{\partial n_F}{\partial \epsilon_{\pm k}}, \tag{E.10}$$

where we have used the relation $\epsilon_{\pm k+k_s} \approx \epsilon_{\pm k} \pm \hbar k v_s$. Plugging into equation (E.8), we find

$$A_{v_s} \approx -\frac{2\hbar^2 v_s}{M}\sum_k k^2 R_{k,\lambda}\left|\frac{\partial\epsilon_k}{\hbar\partial k}\right|\frac{\partial n_F}{\partial\epsilon_k} = \frac{Mv_sB_{v_s}}{k_BT} \tag{E.11}$$

We note that the zeroth-order term of A_{v_s} vanishes because $\sum_k k$ is an odd function of k. Similarly, for B_{v_s} the first order in k_s is $B \propto \sum_k k^3 = 0$. Equation (E.7) is

satisfied *only* if the Pauli-blocking term is included in the microscopic expressions for A_{v_s} and B_{v_s}.

Bibliography

[1] J. M. Kosterlitz. Nobel lecture: Topological defects and phase transitions. *Rev. Mod. Phys.*, 89:040501, Oct 2017.

[2] N David Mermin. The topological theory of defects in ordered media. *Rev. Mod. Phys.*, 51(3):591, 1979.

[3] R Rajaraman. *Solitons and Instantons*. North-Holland, Amsterdam, 1987.

[4] Joel E Moore. The birth of topological insulators. *Nature*, 464(7286):194, 2010.

[5] M Zahid Hasan and Charles L Kane. Colloquium: topological insulators. *Rev. Mod. Phys.*, 82(4):3045, 2010.

[6] Song-Bo Zhang, Hai-Zhou Lu, and Shun-Qing Shen. Edge states and integer quantum hall effect in topological insulator thin films. *Sci. Rep.*, 5:13277, 2015.

[7] Howard Georgi. *Lie algebras in particle physics: from isospin to unified theories*, volume 54. Westview press, 1999.

[8] R Shankar. Applications of topology to the study of ordered systems. *Journal de Physique*, 38(11):1405–1412, 1977.

[9] Heinz Hopf. Über die abbildungen der dreidimensionalen sphäre auf die kugelfläche. *Mathematische Annalen*, 104(1):637–665, 1931.

[10] Paul J Ackerman and Ivan I Smalyukh. Diversity of knot solitons in liquid crystals manifested by linking of preimages in torons and hopfions. *Phys. Rev. X*, 7(1):011006, 2017.

[11] Elie Cartan. *La topologie des groupes de Lie*, volume 358. Hermann & cie, 1936.

[12] Hans-Benjamin Braun. Topological effects in nanomagnetism: from superparamagnetism to chiral quantum solitons. *Advances in Physics*, 61(1):1–116, 2012.

[13] S. Mühlbauer, B. Binz, F. Jonietz, C. Pfleiderer, A. Rosch, A. Neubauer, R. Georgii, and P. Böni. Skyrmion lattice in a chiral magnet. *Science*, 323 (5916):915–919, February 2009.

[14] X. Z. Yu, Y. Onose, N. Kanazawa, J. H. Park, J. H. Han, Y. Matsui, N. Nagaosa, and Y. Tokura. Real-space observation of a two-dimensional skyrmion crystal. *Nature*, 465(7300):901–904, June 2010.

[15] AN Bogdanov and DA Yablonskii. Thermodynamically stable" vortices" in magnetically ordered crystals. the mixed state of magnets. *Zh. Eksp. Teor. Fiz*, 95:182, 1989.

[16] A Bogdanov and A Hubert. Thermodynamically stable magnetic vortex states in magnetic crystals. *J. of Magnetism and Magnetic Mat.*, 138(3): 255–269, 1994.

[17] Jung Hoon Han, Jiadong Zang, Zhihua Yang, Jin-Hong Park, and Naoto Nagaosa. Skyrmion lattice in a two-dimensional chiral magnet. *Phys. Rev. B*, 82(9):094429, 2010.

[18] I Dzyaloshinskii. A thermodynamic theory of weak ferromagnetism of antiferromagnetics. *J. Phys. Chem. Solids*, 4(4):241–255, 1958.

[19] UK Rößler, AN Bogdanov, and C Pfleiderer. Spontaneous skyrmion ground states in magnetic metals. *Nature*, 442(7104):797–801, 2006.

[20] F Jonietz, S Mühlbauer, C Pfleiderer, A Neubauer, W Münzer, A Bauer, T Adams, R Georgii, P Böni, RA Duine, et al. Spin transfer torques in mnsi at ultralow current densities. *Science*, 330(6011):1648–1651, 2010.

[21] Jiadong Zang, Maxim Mostovoy, Jung Hoon Han, and Naoto Nagaosa. Dynamics of skyrmion crystals in metallic thin films. *Phys. Rev. Lett.*, 107(13): 136804, 2011.

[22] Shinichiro Seki, XZ Yu, S Ishiwata, and Y Tokura. Observation of skyrmions in a multiferroic material. *Science*, 336(6078):198–201, 2012.

[23] Ye-Hua Liu, You-Quan Li, and Jung Hoon Han. Skyrmion dynamics in multiferroic insulators. *Phys. Rev. B*, 87(10):100402, 2013.

[24] Lingyao Kong and Jiadong Zang. Dynamics of an insulating skyrmion under a temperature gradient. *Phys. Rev. Lett.*, 111(6):067203, 2013.

[25] Haruki Watanabe and Ashvin Vishwanath. Electric field-induced skyrmion crystals via charged monopoles in insulating helimagets. *Journal of the Physical Society of Japan*, 85(6):064707, 2016.

[26] Naoto Nagaosa and Yoshinori Tokura. Topological properties and dynamics of magnetic skyrmions. *Nat. Nano.*, 8(12):899–911, 2013.

[27] N David Mermin and Ho Wagner. Absence of ferromagnetism or antiferromagnetism in one-or two-dimensional isotropic heisenberg models. *Phys. Rev. Lett.*, 17(22):1133, 1966.

[28] ND Mermin. Absence of ordering in certain classical systems. *J. Math Phys.*, 8(5):1061–1064, 1967.

[29] VL Berezinskii. Destruction of long-range order in one-dimensional and two-dimensional systems having a continuous symmetry group i. classical systems. *Sov. Phys. JETP*, 32(3):493–500, 1971.

[30] J. M. Kosterlitz and D. J. Thouless. Long range order and metastability in two dimensional solids and superfluids.(application of dislocation theory). *Journal of Physics C: Solid State Physics*, 5(11):L124, 1972.

[31] John Michael Kosterlitz and David James Thouless. Ordering, metastability and phase transitions in two-dimensional systems. *J. Phys. C: Solid State*, 6(7):1181, 1973.

[32] K Hirakawa. Kosterlitz-thouless transition in two-dimensional planar ferromagnet k_2cuf_4. *J. of Applied Physics*, 53(3):1893–1898, 1982.

[33] Kinshiro Hirakawa, Hideki Yoshizawa, and Koji Ubukoshi. Neutron scattering study of the phase transition in two-dimensional planar ferromagnet k_2cuf_4. *J. of the Phys. Soc. Japan*, 51(7):2151–2158, 1982.

[34] D Waibel, G Fischer, Th Wolf, H v Löhneysen, and B Pilawa. Determining the berezinskii-kosterlitz-thouless coherence length in $bani_2v_2o_8$ by v^{51} nmr. *Phys. Rev. B*, 91(21):214412, 2015.

[35] LP Regnault, J Rossat-Mignod, JY Henry, and LJ De Jongh. Magnetic properties of the quasi-2d easy plane antiferromagnet $bani_2(po_4)_2$. *Journal of Magnetism and Magnetic Materials*, 31:1205–1206, 1983.

[36] SO Demokritov, NM Kreines, VI Kudinov, and SV Petrov. Fmr and phase diagram of easy plane 2d ferromagnets. *Journal of Magnetism and Magnetic Materials*, 90:305–306, 1990.

[37] CA Cornelius, P Day, PJ Fyne, MT Hutchings, and PJ Walker. Temperature and field dependence of the magnetisation of rb_2crcl_4: a two-dimensional easy-plane ionic ferromagnet. *J. Phys. C: Solid State*, 19(6):909, 1986.

[38] B Sachs, TO Wehling, KS Novoselov, AI Lichtenstein, and MI Katsnelson. Ferromagnetic two-dimensional crystals: Single layers of k_2cuf_4. *Phys. Rev. B*, 88(20):201402, 2013.

[39] Zoran Hadzibabic, Peter Krüger, Marc Cheneau, Baptiste Battelier, and Jean Dalibard. Berezinskii–kosterlitz–thouless crossover in a trapped atomic gas. *Nature*, 441(7097):1118–1121, 2006.

[40] Xiao-Liang Qi and Shou-Cheng Zhang. Topological insulators and superconductors. *Rev. Mod. Phys.*, 83(4):1057, 2011.

[41] J. E. Moore and L. Balents. Topological invariants of time-reversal-invariant band structures. *Phys. Rev. B*, 75:121306, Mar 2007.

[42] Liang Fu, Charles L Kane, and Eugene J Mele. Topological insulators in three dimensions. *Phys. Rev. Lett.*, 98(10):106803, 2007.

[43] Liang Fu and Charles L Kane. Topological insulators with inversion symmetry. *Physical Review B*, 76(4):045302, 2007.

[44] Haijun Zhang, Chao-Xing Liu, Xiao-Liang Qi, Xi Dai, Zhong Fang, and Shou-Cheng Zhang. Topological insulators in bi2se3, bi2te3 and sb2te3 with a single dirac cone on the surface. *Nature Phys.*, 5(6):438, 2009.

[45] Chao-Xing Liu, Xiao-Liang Qi, HaiJun Zhang, Xi Dai, Zhong Fang, and Shou-Cheng Zhang. Model hamiltonian for topological insulators. *Phys. Rev. B*, 82:045122, Jul 2010.

[46] Markus König, Hartmut Buhmann, Laurens W. Molenkamp, Taylor Hughes, Chao-Xing Liu, Xiao-Liang Qi, and Shou-Cheng Zhang. The quantum spin hall effect: theory and experiment. *J. Phys. Soc. Jpn.*, 77(3):031007, 2008.

[47] Peng Wei, Ferhat Katmis, Badih A Assaf, Hadar Steinberg, Pablo Jarillo-Herrero, Donald Heiman, and Jagadeesh S Moodera. Exchange-coupling-induced symmetry breaking in topological insulators. *Phys. Rev. Lett.*, 110 (18):186807, 2013.

[48] Wang-Kong Tse and A H MacDonald. Giant Magneto-Optical Kerr Effect and Universal Faraday Effect in Thin-Film Topological Insulators. *Phys. Rev. Lett.*, 105(5):057401, 2010.

[49] DK Efimkin and Yu E Lozovik. Resonant manifestations of chiral excitons in faraday and kerr effects in a topological insulator film. *Phys. Rev. B*, 87 (24):245416, 2013.

[50] Justin H Wilson, Dmitry K Efimkin, and Victor M Galitski. Resonant faraday and kerr effects due to in-gap states on the surface of a topological insulator. *Phys. Rev. B*, 90(20):205432, 2014.

[51] M. H Anderson, J. R. Ensher, M. R. Matthews, C. E. Wieman, and E. A. Cornell. Observation of bose-einstein condensation in a dilute atomic vapor. *Science*, 269(5221):198–201, 1995.

[52] Lev Pitaevskii and Sandro Stringari. *Bose-Einstein condensation and superfluidity*, volume 164. Oxford University Press, 2016.

[53] Toshio Tsuzuki. Nonlinear waves in the pitaevskii-gross equation. *J. Low Temp. Phys.*, 4(4):441–457, 1971.

[54] A. Muryshev, G. V. Shlyapnikov, W. Ertmer, K. Sengstock, and M. Lewenstein. Dynamics of dark solitons in elongated Bose-Einstein condensates. *Phys. Rev. Lett.*, 89(11):110401, 2002.

[55] Joachim Brand and William P Reinhardt. Solitonic vortices and the fundamental modes of the snake instability: Possibility of observation in the gaseous bose-einstein condensate. *Phys. Rev. A*, 65(4):043612, 2002.

[56] S Komineas, NR Cooper, and N Papanicolaou. Single vortex states in a confined bose-einstein condensate. *Phys. Rev. A*, 72(5):053624, 2005.

[57] Simone Donadello, Simone Serafini, Marek Tylutki, Lev P Pitaevskii, Franco Dalfovo, Giacomo Lamporesi, and Gabriele Ferrari. Observation of solitonic vortices in bose-einstein condensates. *Phys. Rev. Lett.*, 113(6):065302, 2014.

[58] Panayotis G Kevrekidis, Dimitri J Frantzeskakis, and Ricardo Carretero-González. *Emergent nonlinear phenomena in Bose-Einstein condensates: theory and experiment*, volume 45. Springer Science & Business Media, 2007.

[59] Tin-Lun Ho. Spinor Bose condensates in optical traps. *Phys. Rev. Lett.*, 81 (4):742, 1998.

[60] Dan M Stamper-Kurn and Masahito Ueda. Spinor Bose gases: symmetries, magnetism, and quantum dynamics. *Rev. Mod. Phys.*, 85(3):1191, 2013.

[61] C. K. Law, H. Pu, and N. P. Bigelow. Quantum spins mixing in spinor bose-einstein condensates. *Phys. Rev. Lett.*, 81:5257–5261, Dec 1998.

[62] Tin-Lun Ho and Sung Kit Yip. Fragmented and single condensate ground states of spin-1 bose gas. *Phys. Rev. Lett.*, 84:4031–4034, May 2000.

[63] Lauren M. Aycock, Hilary M. Hurst, Dmitry K. Efimkin, Dina Genkina, Hsin-I Lu, Victor M. Galitski, and I. B. Spielman. Brownian motion of solitons in a Bose-Einstein condensate. *Proc. Natl. Acad. Sci. U.S.A.*, page 201615004, 2017.

[64] Alessio Celi, Pietro Massignan, Julius Ruseckas, Nathan Goldman, Ian B Spielman, G Juzeliūnas, and M Lewenstein. Synthetic gauge fields in synthetic dimensions. *Phys. Rev. Lett.*, 112(4):043001, 2014.

[65] B. K. Stuhl, H.-I. Lu, L. M. Aycock, D. Genkina, and I. B. Spielman. Visualizing edge states with an atomic Bose gas in the quantum Hall regime. *Science*, 349(6255):1514–1518, 2015. ISSN 0036-8075.

[66] AA Omrani, JS White, K Prša, I Živković, Helmuth Berger, Arnaud Magrez, Ye-Hua Liu, JH Han, and Henrik M Rønnow. Exploration of the helimagnetic and skyrmion lattice phase diagram in cu 2 oseo 3 using magnetoelectric susceptibility. *Phys. Rev. B*, 89(6):064406, 2014.

[67] JS White, K Prša, P Huang, AA Omrani, I Živković, M Bartkowiak, H Berger, A Magrez, JL Gavilano, G Nagy, et al. Electric-field-induced skyrmion distortion and giant lattice rotation in the magnetoelectric insulator cu 2 oseo 3. *Phys. Rev. Lett.*, 113(10):107203, 2014.

[68] Jonathan S White, Ivana Levatić, AA Omrani, N Egetenmeyer, Krunoslav Prša, Ivica Živković, JL Gavilano, J Kohlbrecher, M Bartkowiak, Helmuth Berger, et al. Electric field control of the skyrmion lattice in cu2oseo3. *J. Phys.: Cond. Matt.*, 24(43):432201, 2012.

[69] Splitting of bound states from continuous bands is accomplished by a redistribution of density of states within the bands, which is of importance here.

[70] Roman Jackiw and C Rebbi. Solitons with fermion number 1/2. *Phys. Rev. D*, 13(12):3398, 1976.

[71] Fred Cooper, Avinash Khare, and Uday Sukhatme. Supersymmetry and quantum mechanics. *Physics Reports*, 251(5-6):267–385, 1995.

[72] Kentaro Nomura and Naoto Nagaosa. Electric charging of magnetic textures on the surface of a topological insulator. *Phys. Rev. B*, 82(16):161401, 2010.

[73] John R Klauder. Path integrals and stationary-phase approximations. *Phys. Rev. D*, 19(8):2349, 1979.

[74] Michael Stone. Supersymmetry and the quantum mechanics of spin. *Nucl. Phys. B*, 314(3):557–586, 1989.

[75] Michael Stone. Magnus force on skyrmions in ferromagnets and quantum hall systems. *Phys. Rev. B*, 53(24):16573, 1996.

[76] Christina Psaroudaki, Silas Hoffman, Jelena Klinovaja, and Daniel Loss. Quantum dynamics of skyrmions in chiral magnets. *arXiv preprint arXiv:1612.01885*, 2016.

[77] T Schulz, R Ritz, A Bauer, M Halder, M Wagner, C Franz, C Pfleiderer, K Everschor, M Garst, and A Rosch. Emergent electrodynamics of skyrmions in a chiral magnet. *Nat. Phys.*, 8(4):301–304, 2012.

[78] Karin Everschor, Markus Garst, RA Duine, and Achim Rosch. Current-induced rotational torques in the skyrmion lattice phase of chiral magnets. *Phys. Rev. B*, 84(6):064401, 2011.

[79] Karin Everschor, Markus Garst, Benedikt Binz, Florian Jonietz, Sebastian Mühlbauer, Christian Pfleiderer, and Achim Rosch. Rotating skyrmion lattices by spin torques and field or temperature gradients. *Phys. Rev. B*, 86 (5):054432, 2012.

[80] S Seki, S Ishiwata, and Y Tokura. Magnetoelectric nature of skyrmions in a chiral magnetic insulator cu 2 oseo 3. *Phys. Rev. B*, 86(6):060403, 2012.

[81] Stefan Heinze, Kirsten von Bergmann, Matthias Menzel, Jens Brede, André Kubetzka, Roland Wiesendanger, Gustav Bihlmayer, and Stefan Blügel. Spontaneous atomic-scale magnetic skyrmion lattice in two dimensions. *Nat. Phys.*, 7(9):713–718, September 2011.

[82] Yuval Baum and Ady Stern. Density-waves instability and a skyrmion lattice on the surface of strong topological insulators. *Phys. Rev. B*, 86:195116, Nov 2012.

[83] Yoshinori Okada, Chetan Dhital, Wenwen Zhou, Erik D Huemiller, Hsin Lin, S Basak, A Bansil, Y-B Huang, H Ding, Z Wang, et al. Direct observation of broken time-reversal symmetry on the surface of a magnetically doped topological insulator. *Phys. Rev. Lett.*, 106(20):206805, 2011.

[84] Inhee Lee, Chung Koo Kim, Jinho Lee, Simon JL Billinge, Ruidan Zhong, John A Schneeloch, Tiansheng Liu, Tonica Valla, John M Tranquada, Genda Gu, et al. Imaging dirac-mass disorder from magnetic dopant atoms in the ferromagnetic topological insulator crx (bi0. 1sb0. 9) 2-xte3. *PNAS*, 112(5): 1316–1321, 2015.

[85] Ion Garate and M Franz. Magnetoelectric response of the time-reversal invariant helical metal. *Phys. Rev. B*, 81(17):172408, 2010.

[86] HK Pal, VI Yudson, and DL Maslov. Effect of electron-electron interaction on surface transport in the bi 2 te 3 family of three-dimensional topological insulators. *Phys. Rev. B*, 85(8):085439, 2012.

[87] Henrik Bruus and Karsten Flensberg. *Many-Body Quantum Theory in Condensed Matter Physics*. OUP Oxford, 2004.

[88] Dong-Xia Qu, YS Hor, Jun Xiong, RJ Cava, and NP Ong. Quantum oscillations and hall anomaly of surface states in the topological insulator bi_2te_3. *Science*, 329(5993):821–824, 2010.

[89] SE Harrison, LJ Collins-McIntyre, P Schönherr, A Vailionis, V Srot, PA van Aken, AJ Kellock, A Pushp, SSP Parkin, JS Harris, et al. Massive dirac fermion observed in lanthanide-doped topological insulator thin films. *Sci. Rep.*, 5, 2015.

[90] P. O. Fedichev, A. E. Muryshev, and G. V. Shlyapnikov. Dissipative dynamics of a kink state in a Bose-condensed gas. *Phys. Rev. A*, 60(4):3220, 1999.

[91] B. A. Ivanov and A. K. Kolezhuk. Soliton diffusion in one-dimensional systems close to integrable ones. *Phys. Lett. A*, 146(4):190–194, 1990.

[92] N. G. Parker, N. P. Proukakis, M. Leadbeater, and C. S. Adams. Soliton-sound interactions in quasi-one-dimensional Bose-Einstein condensates. *Phys. Rev. Lett.*, 90(22):220401, 2003.

[93] Parker, N. G. and Proukakis, N. P. and Adams, C. S. Dark soliton decay due to trap anharmonicity in atomic Bose-Einstein condensates. *Phys. Rev. A*, 81(3):033606, 2010.

[94] Th. Busch and J. R. Anglin. Dark-bright solitons in inhomogeneous Bose-Einstein condensates. *Phys. Rev. Lett.*, 87(1):010401, 2001.

[95] B. Jackson, N. P. Proukakis, and C. F. Barenghi. Dark-soliton dynamics in Bose-Einstein condensates at finite temperature. *Phys. Rev. A*, 75(5): 051601, 2007.

[96] D. K. Efimkin, J. Hofmann, and V. Galitski. Non-Markovian quantum friction of bright solitons in superfluids. *Phys. Rev. Lett.*, 116(22):225301, 2016.

[97] A. Einstein. On the movement of small particles suspended in stationary liquids required by the molecular-kinetic theory of heat. *Annalen der Physik*, 17:549–560, 1905.

[98] Maxim Olshanii. Atomic scattering in the presence of an external confinement and a gas of impenetrable bosons. *Phys. Rev. Lett.*, 81(5):938, 1998.

[99] A. Imambekov and E. Demler. Exactly solvable case of a one-dimensional Bose-Fermi mixture. *Phys. Rev. A*, 73(2):021602, 2006.

[100] C. K. Lai and C. N. Yang. Ground-state energy of a mixture of fermions and bosons in one dimension with a repulsive δ-function interaction. *Phys. Rev. A*, 3:393–399, Jan 1971.

[101] Andrew G. Truscott, Kevin E. Strecker, William I. McAlexander, Guthrie B. Partridge, and Randall G. Hulet. Observation of Fermi pressure in a gas of trapped atoms. *Science*, 291(5513):2570–2572, 2001.

[102] F. Schreck, L. Khaykovich, K. L. Corwin, G. Ferrari, T. Bourdel, J. Cubizolles, and C. Salomon. Quasipure Bose-Einstein condensate immersed in a Fermi sea. *Phys. Rev. Lett.*, 87:080403, Aug 2001.

[103] Z. Hadzibabic, C. A. Stan, K. Dieckmann, S. Gupta, M. W. Zwierlein, A. Görlitz, and W. Ketterle. Two-species mixture of quantum degenerate Bose and Fermi gases. *Phys. Rev. Lett.*, 88:160401, Apr 2002.

[104] J. Goldwin, S. Inouye, M. L. Olsen, B. Newman, B. D. DePaola, and D. S. Jin. Measurement of the interaction strength in a Bose-Fermi mixture with ^{87}Rb and ^{40}K. *Phys. Rev. A*, 70(2):021601, 2004.

[105] Richard Roy, Alaina Green, Ryan Bowler, and Subhadeep Gupta. Two-element mixture of Bose and Fermi superfluids. *Phys. Rev. Lett.*, 118:055301, Feb 2017.

[106] E. M. Lifschitz and L. P. Pitaevskii. *Course of Theoretical Physics Vol. 10: Physical Kinetics*. Oxford, 1983.

[107] G. Pöschl and E. Teller. Bemerkungen zur Quantenmechanik des anharmonischen Oszillators. *Zeitschrift für Physik*, 83(3-4):143–151, 1933.

[108] A. Frank and K. B. Wolf. Lie algebras for potential scattering. *Phys. Rev. Lett.*, 52(20):1737, 1984.

[109] J. Guerrero. A group-theoretical derivation of the S-matrix for the Pöschl-Teller potentials. In *J. Phys: Conference Series*, volume 237, page 012012. IOP Publishing, 2010.

[110] Y. Alhassid, F. Gürsey, and F. Iachello. Potential scattering, transfer matrix, and group theory. *Phys. Rev. Lett.*, 50(12):873, 1983.

[111] D. Çevik, M. Gadella, Ş. Kuru, and J. Negro. Resonances and antibound states for the Pöschl–Teller potential: Ladder operators and SUSY partners. *Phys. Lett. A*, 380(18):1600–1609, 2016.

[112] M. I. Shaukat, E. V. Castro, and H. Terças. Quantum dark solitons as qubits in bose-einstein condensates. *Phys. Rev. A*, 95:053618, May 2017.

[113] V. V. Konotop and L. Pitaevskii. Landau dynamics of a grey soliton in a trapped condensate. *Phys. Rev. Lett.*, 93(24):240403, 2004.

[114] Th. Busch and J. R. Anglin. Motion of dark solitons in trapped Bose-Einstein condensates. *Phys. Rev. Lett.*, 84(11):2298, 2000.

[115] A. Weller, J. P. Ronzheimer, C. Gross, J. Esteve, M. K. Oberthaler, D. J. Frantzeskakis, G. Theocharis, and P. G. Kevrekidis. Experimental observation of oscillating and interacting matter wave dark solitons. *Phys. Rev. Lett.*, 101(13):130401, 2008.

[116] Stefan Burger, K. Bongs, S. Dettmer, W. Ertmer, K. Sengstock, A. Sanpera, G. V. Shlyapnikov, and M. Lewenstein. Dark solitons in Bose-Einstein condensates. *Phys. Rev. Lett.*, 83(25):5198, 1999.

[117] J. Denschlag, J. E. Simsarian, D. L. Feder, Charles W. Clark, L. A. Collins, J. Cubizolles, L. Deng, E. W. Hagley, K. Helmerson, W. P. Reinhardt, S. L. Rolston, B. I. Schneider, and W. D. Phillips. Generating solitons by phase engineering of a Bose-Einstein condensate. *Science*, 287(5450):97–101, 2000.

[118] A Muñoz Mateo and Joachim Brand. Stability and dispersion relations of three-dimensional solitary waves in trapped Bose-Einstein condensates. *New J. Phys.*, 17(12):125013, 2015.

[119] Masaaki Kitagawa, Katsunari Enomoto, Kentaro Kasa, Yoshiro Takahashi, Roman Ciuryło, Pascal Naidon, and Paul S. Julienne. Two-color photoassociation spectroscopy of ytterbium atoms and the precise determinations of s-wave scattering lengths. *Phys. Rev. A*, 77(1):012719, 2008.

[120] Takeshi Fukuhara, Seiji Sugawa, Yosuke Takasu, and Yoshiro Takahashi. All-optical formation of quantum degenerate mixtures. *Phys. Rev. A*, 79(2): 021601, 2009.

[121] N. D. Lemke, A. D. Ludlow, Z. W. Barber, T. M. Fortier, S. A. Diddams, Y. Jiang, S. R. Jefferts, T. P. Heavner, T. E. Parker, and C. W. Oates. Spin-1/2 optical lattice clock. *Phys. Rev. Lett.*, 103(6):063001, 2009.

[122] Min-Seok Kim, Jeongwon Lee, Jae Hoon Lee, Y. Shin, and Jongchul Mun. Measurements of optical Feshbach resonances of ^{174}Yb atoms. *Phys. Rev. A*, 94:042703, Oct 2016.

[123] Xi-Wang Luo, Xingxiang Zhou, Chuan-Feng Li, Jin-Shi Xu, Guang-Can Guo, and Zheng-Wei Zhou. Quantum simulation of 2D topological physics in a 1D array of optical cavities. *Nat. Commun.*, 6, 2015.

[124] F Kolley, M Piraud, IP McCulloch, U Schollwöck, and F Heidrich-Meisner. Strongly interacting bosons on a three-leg ladder in the presence of a homogeneous flux. *New J. Phys.*, 17(9):092001, 2015.

[125] Marcos Atala, Monika Aidelsburger, Michael Lohse, Julio T Barreiro, Belén Paredes, and Immanuel Bloch. Observation of chiral currents with ultracold atoms in bosonic ladders. *Nature Phys.*, 10(8):588–593, 2014.

[126] Tian-Sheng Zeng, Ce Wang, and Hui Zhai. Charge pumping of interacting fermion atoms in the synthetic dimension. *Phys. Rev. Lett.*, 115:095302, Aug 2015.

[127] M. Mancini, G. Pagano, G. Cappellini, L. Livi, M. Rider, J. Catani, C. Sias, P. Zoller, M. Inguscio, M. Dalmonte, and L. Fallani. Observation of chiral

edge states with neutral fermions in synthetic Hall ribbons. *Science*, 349 (6255):1510–1513, 2015. ISSN 0036-8075.

[128] Victor Galitski and Ian B Spielman. Spin-orbit coupling in quantum gases. *Nature*, 494(7435):49–54, 2013.

[129] MC Beeler, RA Williams, Karina Jimenez-Garcia, LJ LeBlanc, AR Perry, and IB Spielman. The spin Hall effect in a quantum gas. *Nature*, 498(7453): 201–204, 2013.

[130] Jean Dalibard, Fabrice Gerbier, Gediminas Juzeliūnas, and Patrik Öhberg. Colloquium: Artificial gauge potentials for neutral atoms. *Rev. Mod. Phys.*, 83(4):1523, 2011.

[131] Chunji Wang, Chao Gao, Chao-Ming Jian, and Hui Zhai. Spin-orbit coupled spinor Bose-Einstein condensates. *Phys. Rev. Lett.*, 105(16):160403, 2010.

[132] Tin-Lun Ho and Shizhong Zhang. Bose-Einstein condensates with spin-orbit interaction. *Phys. Rev. Lett.*, 107(15):150403, 2011.

[133] Zhihao Lan and Patrik Öhberg. Raman-dressed spin-1 spin-orbit-coupled quantum gas. *Phys. Rev. A*, 89(2):023630, 2014.

[134] Wu Cong-Jun, Ian Mondragon-Shem, and Zhou Xiang-Fa. Unconventional Bose-Einstein condensations from spin-orbit coupling. *Chin. Phys. Lett.*, 28 (9):097102, 2011.

[135] Yun Li, Lev P Pitaevskii, and Sandro Stringari. Quantum tricriticality and phase transitions in spin-orbit coupled Bose-Einstein condensates. *Phys. Rev. Lett.*, 108(22):225301, 2012.

[136] ZF Xu, Y Kawaguchi, L You, and M Ueda. Symmetry classification of spin-orbit-coupled spinor Bose-Einstein condensates. *Phys. Rev. A*, 86(3):033628, 2012.

[137] Zeng-Qiang Yu. Ground-state phase diagram and critical temperature of two-component Bose gases with Rashba spin-orbit coupling. *Phys. Rev. A*, 87(5):051606, 2013.

[138] Stefan S Natu, Xiaopeng Li, and William S Cole. Striped ferronematic ground states in a spin-orbit-coupled $S = 1$ Bose gas. *Phys. Rev. A*, 91(2): 023608, 2015.

[139] Kuei Sun, Chunlei Qu, Yong Xu, Yongping Zhang, and Chuanwei Zhang. Interacting spin-orbit-coupled spin-1 Bose-Einstein condensates. *Phys. Rev. A*, 93(2):023615, 2016.

[140] Giovanni I Martone, Francesco V Pepe, Paolo Facchi, Saverio Pascazio, and Sandro Stringari. Tricriticalities and quantum phases in spin-orbit-coupled spin-1 bose gases. *Phys. Rev. Lett.*, 117(12):125301, 2016.

[141] Hannah M Price, Oded Zilberberg, Tomoki Ozawa, Iacopo Carusotto, and Nathan Goldman. Four-dimensional quantum Hall effect with ultracold atoms. *Phys. Rev. Lett.*, 115(19):195303, 2015.

[142] Zeng-Qiang Yu. Phase transitions and elementary excitations in spin-1 Bose gases with Raman-induced spin-orbit coupling. *Phys. Rev. A*, 93:033648, Mar 2016.

[143] Li Chen, Han Pu, and Yunbo Zhang. Spin-orbit angular momentum coupling in a spin-1 Bose-Einstein condensate. *Phys. Rev. A*, 93:013629, Jan 2016.

[144] J. H. Pixley, Stefan S. Natu, I. B. Spielman, and S. Das Sarma. Interaction-driven exotic quantum phases in spin-orbit-coupled spin-1 bosons. *Phys. Rev. B*, 93:081101(R), Feb 2016.

[145] Zhu Chen and Zhaoxin Liang. Ground-state phase diagram of a spin-orbit-coupled bosonic superfluid in an optical lattice. *Phys. Rev. A*, 93(1):013601, 2016.

[146] Giovanni I Martone, Tomoki Ozawa, Chunlei Qu, and Sandro Stringari. Optical-lattice-assisted magnetic phase transition in a spin-orbit-coupled Bose-Einstein condensate. *Phys. Rev. A*, 94(4):043629, 2016.

[147] ML Chiofalo, S Succi, and MP Tosi. Ground state of trapped interacting Bose-Einstein condensates by an explicit imaginary-time algorithm. *Phys. Rev. E*, 62(5):7438, 2000.

[148] Xavier Antoine and Romain Duboscq. GPELab, a Matlab toolbox to solve Gross–Pitaevskii equations I: Computation of stationary solutions. *Comput. Phys. Commun.*, 185(11):2969–2991, 2014.

[149] Tetsuo Ohmi and Kazushige Machida. Bose-Einstein condensation with internal degrees of freedom in alkali atom gases. *J Phys. Soc. Jpn.*, 67(6): 1822–1825, 1998.

[150] Izrail Solomonovich Gradshteyn and Iosif Moiseevich Ryzhik. *Table of integrals, series, and products*. Academic press, 2014.

[151] Jun John Sakurai and Eugene D Commins. *Modern Quantum Mechanics*. AAPT, 1995.

[152] H. Risken. *The Fokker-Planck equation*. Springer, 1984.